EUROPEAN ORGANIZATION FOR PARTICLE PHYSICS

CERN-EP/99-136
28 Sep 1999

Precision Luminosity for Z^0 Lineshape Measurements with a Silicon-Tungsten Calorimeter

The OPAL Collaboration

Abstract

The measurement of small–angle Bhabha scattering is used to determine the luminosity at the OPAL interaction point for the LEP I data recorded between 1993 and 1995. The measurement is based on the OPAL Silicon-Tungsten Luminometer which is composed of two calorimeters encircling the LEP beam pipe, on opposite sides of the interaction point. The luminometer detects electrons from small–angle Bhabha scattering at angles between 25 and 58 mrad. At LEP center-of-mass energies around the Z^0, about half of all Bhabha electrons entering the detector fall within a 79 nb fiducial acceptance region. The electromagnetic showers generated in the stack of 1 radiation length tungsten absorber plates are sampled by 608 silicon detectors with $38,912$ radial pads of 2.5 mm width. The fine segmentation of the detector, combined with the precise knowledge of its physical dimensions, allows the trajectories of incoming 45 GeV electrons or photons to be determined with a total systematic error of less than 7 microns. We have quantified all significant sources of systematic experimental error in the luminosity determination by direct physical measurement. All measured properites of the luminosity event sample are found to be in agreement with current theoretical expectations. The total systematic measurement uncertainty is 3.4×10^{-4}, significantly below the theoretical error of 5.4×10^{-4} currently assigned to the QED calculation of the Bhabha acceptance, and contributes negligibly to the total uncertainty in the OPAL measurement of $\Gamma_{\mathrm{inv}}/\Gamma_{\ell^+\ell^-}$, a quantity of basic physical interest which depends crucially on the luminosity measurement.

To be submitted to Eur. Phys. J. C

The OPAL Collaboration

G. Abbiendi[2], K. Ackerstaff[8], G. Alexander[23], J. Allison[16], K.J. Anderson[9], S. Anderson[12], S. Arcelli[17], S. Asai[24], S.F. Ashby[1], D. Axen[29], G. Azuelos[18,a], A.H. Ball[8], E. Barberio[8], R.J. Barlow[16], J.R. Batley[5], S. Baumann[3], J. Bechtluft[14], T. Behnke[27], K.W. Bell[20], G. Bella[23], A. Bellerive[9], S. Bentvelsen[8], S. Bethke[14], S. Betts[15], O. Biebel[14], A. Biguzzi[5], I.J. Bloodworth[1], P. Bock[11], J. Böhme[14], O. Boeriu[10], D. Bonacorsi[2], M. Boutemeur[33], S. Braibant[8], P. Bright-Thomas[1], L. Brigliadori[2], R.M. Brown[20], H.J. Burckhart[8], P. Capiluppi[2], R.K. Carnegie[6], A.A. Carter[13], J.R. Carter[5], C.Y. Chang[17], D.G. Charlton[1,b], D. Chrisman[4], C. Ciocca[2], P.E.L. Clarke[15], E. Clay[15], I. Cohen[23], J.E. Conboy[15], O.C. Cooke[8], J. Couchman[15], C. Couyoumtzelis[13], R.L. Coxe[9], M. Cuffiani[2], S. Dado[22], G.M. Dallavalle[2], S. Dallison[16], C. Darling[34], R. Davis[30], S. De Jong[12], A. de Roeck[8], P. Dervan[15], K. Desch[27], B. Dienes[32,h], M.S. Dixit[7], M. Donkers[6], J. Dubbert[33], E. Duchovni[26], G. Duckeck[33], I.P. Duerdoth[16], P.G. Estabrooks[6], E. Etzion[23], H. Evans[9,i], F. Fabbri[2], A. Fanfani[2], M. Fanti[2], A.A. Faust[30], L. Feld[10], P. Ferrari[12], F. Fiedler[27], M. Fierro[2], I. Fleck[10], M. Foucher[17], A. Frey[8], A. Fürtjes[8], D.I. Futyan[16], P. Gagnon[7], J.W. Gary[4], S. Gascon-Shotkin[17], G. Gaycken[27], C. Geich-Gimbel[3], G. Giacomelli[2], P. Giacomelli[2], R. Giacomelli[2], W.R. Gibson[13], D.M. Gingrich[30,a], D. Glenzinski[9], J. Goldberg[22], W. Gorn[4], C. Grandi[2], K. Graham[28], E. Gross[26], J. Grunhaus[23], M. Gruwé[27], C. Hajdu[31] G.G. Hanson[12], M. Hansroul[8], M. Hapke[13], K. Harder[27], A. Harel[22], C.K. Hargrove[7], M. Harin-Dirac[4], P. Hart[9,k], M. Hauschild[8], C.M. Hawkes[1], R. Hawkings[27], R.J. Hemingway[6], G. Herten[10], R.D. Heuer[27], M.D. Hildreth[8], J.C. Hill[5], S. Hillier[1], P.R. Hobson[25], A. Hocker[9], K. Hoffman[8], R.J. Homer[1], A.K. Honma[28,a], D. Horváth[31,c], K.R. Hossain[30], R. Howard[29], P. Hüntemeyer[27], P. Igo-Kemenes[11], D.C. Imrie[25], K. Ishii[24], F.R. Jacob[20], A. Jawahery[17], H. Jeremie[18], M. Jimack[1], C.R. Jones[5], P. Jovanovic[1], T.R. Junk[6], N. Kanaya[24], J. Kanzaki[24], D. Karlen[6], V. Kartvelishvili[16], K. Kawagoe[24], T. Kawamoto[24], P.I. Kayal[30], R.K. Keeler[28], R.G. Kellogg[17], B.W. Kennedy[20], D.H. Kim[19], J. Kirk[8], A. Klier[26], T. Kobayashi[24], M. Kobel[3,d], T.P. Kokott[3], M. Kolrep[10], S. Komamiya[24], R.V. Kowalewski[28], T. Kress[4], P. Krieger[6], J. von Krogh[11], T. Kuhl[3], P. Kyberd[13], W.P. Lai[19,o], G.D. Lafferty[16], R. Lahmann[17,m], H. Landsman[22], D. Lanske[14], J. Lauber[15], I. Lawson[28], J.G. Layter[4], A.M. Lee[34], D. Lellouch[26], J. Letts[12], L. Levinson[26], R. Liebisch[11], J. Lillich[10], B. List[8], C. Littlewood[5], A.W. Lloyd[1], S.L. Lloyd[13], F.K. Loebinger[16], G.D. Long[28], M.J. Losty[7], J. Lu[29], J. Ludwig[10], D. Liu[12], A. Macchiolo[18], A. Macpherson[30], W. Mader[3], M. Mannelli[8], S. Marcellini[2], T.E. Marchant[16], A.J. Martin[13], J.P. Martin[18], G. Martinez[17], T. Mashimo[24], P. Mättig[26], W.J. McDonald[30], J. McKenna[29], E.A. Mckigney[15], T.J. McMahon[1], R.A. McPherson[28], F. Meijers[8], P. Mendez-Lorenzo[33], S. Menke[3], F.S. Merritt[9], H. Mes[7], I. Meyer[5], A. Michelini[2], S. Mihara[24], G. Mikenberg[26], D.J. Miller[15], W. Mohr[10], A. Montanari[2], T. Mori[24], U. Müller[3], K. Nagai[8], I. Nakamura[24], H.A. Neal[12,g], R. Nisius[8], S.W. O'Neale[1], F.G. Oakham[7], F. Odorici[2], H.O. Ogren[12], A. Okpara[11], M.J. Oreglia[9], S. Orito[24], F. Palmonari[2], G. Pásztor[31], J.R. Pater[16], G.N. Patrick[20], J. Patt[10], R. Perez-Ochoa[8], S. Petzold[27], P. Pfeifenschneider[14], J.E. Pilcher[9], J. Pinfold[30], D.E. Plane[8], P. Poffenberger[28], B. Poli[2], J. Polok[8], M. Przybycień[8,e], A. Quadt[8], B. Raith[3], C. Rembser[8], H. Rick[8], S. Robertson[28], S.A. Robins[22], N. Rodning[30], J.M. Roney[28], S. Rosati[3], K. Roscoe[16], A.M. Rossi[2], Y. Rozen[22], K. Runge[10], O. Runolfsson[8], D.R. Rust[12], K. Sachs[10], T. Saeki[24], O. Sahr[33], W.M. Sang[25], E.K.G. Sarkisyan[23], C. Sbarra[29], A.D. Schaile[33], O. Schaile[33], P. Scharff-Hansen[8], J. Schieck[11], B. Schmitt[3], S. Schmitt[11], A. Schöning[8], M. Schröder[8], M. Schumacher[3], C. Schwick[8], W.G. Scott[20], R. Seuster[14], T.G. Shears[8], B.C. Shen[4], C.H. Shepherd-Themistocleous[5], P. Sherwood[15], G.P. Siroli[2], A. Skuja[17], A.M. Smith[8], G.A. Snow[17], R. Sobie[28], S. Söldner-Rembold[10,f], S. Spagnolo[20], W. Springer[17,n], M. Sproston[20], A. Stahl[3], K. Stephens[16], K. Stoll[10], D. Strom[19], R. Ströhmer[33], B. Surrow[8], S.D. Talbot[1], P. Taras[18], S. Tarem[22], M. Tecchio[9,l], R. Teuscher[9], M. Thiergen[10], J. Thomas[15], M.A. Thomson[8], E. Torrence[8], S. Towers[6], T. Trefzger[33], I. Trigger[18], Z. Trócsányi[32,h], E. Tsur[23], M.F. Turner-Watson[1], I. Ueda[24], R. Van Kooten[12], P. Vannerem[10], M. Verzocchi[8], H. Voss[3], F. Wäckerle[10], A. Wagner[27], D. Wagner[9,j], D. Waller[6], C.P. Ward[5], D.R. Ward[5], P.M. Watkins[1],

A.T. Watson[1], N.K. Watson[1], P.S. Wells[8], N. Wermes[3], D. Wetterling[11] J.S. White[6], G.W. Wilson[16],
J.A. Wilson[1], T.R. Wyatt[16], S. Yamashita[24], V. Zacek[18], D. Zer-Zion[8]

[1]School of Physics and Astronomy, University of Birmingham, Birmingham B15 2TT, UK
[2]Dipartimento di Fisica dell' Università di Bologna and INFN, I-40126 Bologna, Italy
[3]Physikalisches Institut, Universität Bonn, D-53115 Bonn, Germany
[4]Department of Physics, University of California, Riverside CA 92521, USA
[5]Cavendish Laboratory, Cambridge CB3 0HE, UK
[6]Ottawa-Carleton Institute for Physics, Department of Physics, Carleton University, Ottawa, Ontario K1S 5B6, Canada
[7]Centre for Research in Particle Physics, Carleton University, Ottawa, Ontario K1S 5B6, Canada
[8]CERN, European Organisation for Particle Physics, CH-1211 Geneva 23, Switzerland
[9]Enrico Fermi Institute and Department of Physics, University of Chicago, Chicago IL 60637, USA
[10]Fakultät für Physik, Albert Ludwigs Universität, D-79104 Freiburg, Germany
[11]Physikalisches Institut, Universität Heidelberg, D-69120 Heidelberg, Germany
[12]Indiana University, Department of Physics, Swain Hall West 117, Bloomington IN 47405, USA
[13]Queen Mary and Westfield College, University of London, London E1 4NS, UK
[14]Technische Hochschule Aachen, III Physikalisches Institut, Sommerfeldstrasse 26-28, D-52056 Aachen, Germany
[15]University College London, London WC1E 6BT, UK
[16]Department of Physics, Schuster Laboratory, The University, Manchester M13 9PL, UK
[17]Department of Physics, University of Maryland, College Park, MD 20742, USA
[18]Laboratoire de Physique Nucléaire, Université de Montréal, Montréal, Quebec H3C 3J7, Canada
[19]University of Oregon, Department of Physics, Eugene OR 97403, USA
[20]CLRC Rutherford Appleton Laboratory, Chilton, Didcot, Oxfordshire OX11 0QX, UK
[22]Department of Physics, Technion-Israel Institute of Technology, Haifa 32000, Israel
[23]Department of Physics and Astronomy, Tel Aviv University, Tel Aviv 69978, Israel
[24]International Centre for Elementary Particle Physics and Department of Physics, University of Tokyo, Tokyo 113-0033, and Kobe University, Kobe 657-8501, Japan
[25]Institute of Physical and Environmental Sciences, Brunel University, Uxbridge, Middlesex UB8 3PH, UK
[26]Particle Physics Department, Weizmann Institute of Science, Rehovot 76100, Israel
[27]Universität Hamburg/DESY, II Institut für Experimental Physik, Notkestrasse 85, D-22607 Hamburg, Germany
[28]University of Victoria, Department of Physics, P O Box 3055, Victoria BC V8W 3P6, Canada
[29]University of British Columbia, Department of Physics, Vancouver BC V6T 1Z1, Canada
[30]University of Alberta, Department of Physics, Edmonton AB T6G 2J1, Canada
[31]Research Institute for Particle and Nuclear Physics, H-1525 Budapest, P O Box 49, Hungary
[32]Institute of Nuclear Research, H-4001 Debrecen, P O Box 51, Hungary
[33]Ludwigs-Maximilians-Universität München, Sektion Physik, Am Coulombwall 1, D-85748 Garching, Germany
[34]Duke University, Department of Physics, Durham NC 27708-0305, USA

[a] and at TRIUMF, Vancouver, Canada V6T 2A3
[b] and Royal Society University Research Fellow
[c] and Institute of Nuclear Research, Debrecen, Hungary
[d] on leave of absence from the University of Freiburg
[e] and University of Mining and Metallurgy, Cracow
[f] and Heisenberg Fellow

[g] now at Yale University, Dept of Physics, New Haven, CT, USA
[h] and Department of Experimental Physics, Lajos Kossuth University, Debrecen, Hungary.
[i] now at Columbia University, Dept of Physics, New York, NY, USA
[j] now at University of Colorado, Dept of Physics, Boulder, CO, USA
[k] now at University of California, Santa Barbara, Dept of Physics, Santa Barbara, CA, USA
[l] now at University of Michigan, Dept of Physics, Ann Arbor, MI, USA
[m] now at DESY, Hamburg
[n] now at University of Utah, Dept of Physics, Salt Lake City, UT 84112, USA
[o] now at Academia Sinica, Taiwan

1 Introduction

Precision measurements of the leptonic and hadronic production cross sections in electron-positron annihilations near the Z^0 resonance are a vital part of the LEP physics program [?, ?, ?, ?]. The precision with which such cross-section measurements can be made has often been limited by the experimental systematic error on the luminosity of the colliding beams. For example, at PEP and PETRA where both wide-angle and small-angle Bhabha scattering were used to determine the luminosity, the experimental systematic errors were 2–5% and much larger than the statistical error inherent in the number of multihadron events produced [?].

In LEP collider runs near the Z^0 resonance, data samples of order 5×10^6 Z^0 decays have been delivered to each of the four experiments. If these data are to be used efficiently, a very precise determination of the luminosity must be made. In the initial running at the Z^0 resonance, OPAL was able to determine the luminosity to significantly better than 1% but it was clear that the experimental systematic error could not be expected to keep pace with the foreseen improvements in Z^0 statistics. In 1991 the decision was taken to build a second-generation luminosity monitor. The new detector, referred to as SiW, employs calorimeters with tungsten absorber and silicon sampling and was first operated in the 1993 LEP run. In this document we describe the determination of the OPAL luminosity for the 1993, 1994 and 1995 LEP runs at the Z^0. The measurement has an experimental systematic error of 3.4×10^{-4}, an improvement of nearly two orders of magnitude on the PEP/PETRA measurements, and is substantially more precise than other luminosity measurements at the Z^0 [?].

1.1 Physics motivation

The measurement of the Z^0 resonance parameters requires precise cross section measurements at several different energies. From the shape of the resonance, the Z^0 mass, m_Z, and total width, Γ_Z, are determined. The overall normalization of the resonance is given by the peak cross sections to all accessible charged fermions, $\sigma^\mathrm{pole}_\mathrm{had}$, $\sigma^\mathrm{pole}_\mathrm{ee}$, $\sigma^\mathrm{pole}_{\mu\mu}$ and $\sigma^\mathrm{pole}_{\tau\tau}$. The measurement of these cross sections requires an absolute determination of the luminosity. In principle, measurement of m_Z and Γ_Z requires only a relative luminosity measurement. In practice the situation is more complicated. The "off-peak" data were collected in energy scans in 1993 and 1995 with the bulk of the "on-peak" data taken in 1994. To make the best use of the data for determining Γ_Z, the luminosity measurement must be stable between years, requiring an analysis which is similar to the determination of the absolute luminosity.

The importance of m_Z as a fundamental input to the Standard Model and the sensitivity of Γ_Z to radiative corrections involving the top mass, m_t, and the Higgs mass, m_h, are well known [?]. The physics interpretation of the the total cross sections is somewhat more involved. At tree level the cross sections for fermion-pair production at the Z^0 can be expressed as

$$\sigma^\mathrm{pole}_{\mathrm{f\bar{f}}} = \frac{12\pi}{m_\mathrm{Z}^2} \frac{\Gamma_{\mathrm{e^+e^-}} \Gamma_{\mathrm{f\bar{f}}}}{\Gamma_\mathrm{Z}^2}, \qquad (1)$$

where $\Gamma_{\mathrm{e^+e^-}}$ is the partial decay width of the Z^0 to electrons, $\Gamma_{\mathrm{f\bar{f}}}$ the partial decay width to a given fermion pair, and Γ_Z is the total decay width of the Z^0. The physics of the absolute cross section can be seen most clearly if equation 1 is expressed in terms of branching ratios:

$$\sigma^\mathrm{pole}_{\mathrm{f\bar{f}}} = \frac{12\pi}{m_\mathrm{Z}^2} Br(\mathrm{Z}^0 \to \mathrm{e^+e^-}) Br(\mathrm{Z}^0 \to \mathrm{f\bar{f}}). \qquad (2)$$

Thus the measurement of the pole cross section of the Z^0 to fermion pairs, $\sigma^\mathrm{pole}_{\mathrm{f\bar{f}}}$, allows us to make measurements of absolute branching ratios.

In particular, $Br(\mathrm{Z}^0 \to \mathrm{inv})$, the branching ratio of the Z^0 to particles such as neutrinos which are not visible in our detector,[1] is measureable only by determining the absolute production cross sections

---

[1] More precisely, the measured invisible width contains any contribution to the Z^0 decay width which is not accounted for by either the multihadron or charged lepton pair analyses.

of visible final states. An especially interesting quantity involving $Br(\mathrm{Z}^0 \rightarrow \mathrm{inv})$ is

$$R_{\mathrm{inv}} \equiv \frac{Br(\mathrm{Z}^0 \rightarrow \mathrm{inv})}{Br(\mathrm{Z}^0 \rightarrow \ell^+\ell^-)} \tag{3}$$

where $Br(\mathrm{Z}^0 \rightarrow \ell^+\ell^-)$ is the leptonic width of a single generation. Assuming charged lepton universality, the invisible branching ratio is

$$Br(\mathrm{Z}^0 \rightarrow \mathrm{inv}) = 1 - Br(\mathrm{Z}^0 \rightarrow \mathrm{had}) - 3\ Br(\mathrm{Z}^0 \rightarrow \ell^+\ell^-) \tag{4}$$

where $Br(\mathrm{Z}^0 \rightarrow \mathrm{had})$ is the total branching ratio to the 5 quarks kinematically accessible at the Z^0. Using equation 2, equation 3 can be rewritten as

$$R_{\mathrm{inv}} \ = \ \left(\frac{12\pi}{\sigma^{\mathrm{pole}}_{\ell^+\ell^-} m^2_{\mathrm{Z}}} \right)^{\frac{1}{2}} \ - \ R_{\mathrm{had}} \ - \ 3 \tag{5}$$

where R_{had} is the ratio of hadronic to leptonic Z^0 decays given by $R_{\mathrm{had}} = \frac{Br(\mathrm{Z}^0 \rightarrow \mathrm{had})}{Br(\mathrm{Z}^0 \rightarrow \ell^+\ell^-)}$. Measurement of the quantities in equation 5 allows the Standard Model prediction for the coupling of the Z^0 to neutrinos to be tested. The Standard Model prediction for R_{inv},

$$R^{\mathrm{SM}}_{\mathrm{inv}} \equiv 3 \frac{Br(\mathrm{Z}^0 \rightarrow \nu\bar{\nu})}{Br(\mathrm{Z}^0 \rightarrow \ell^+\ell^-)} \tag{6}$$

depends only weakly on m_{t} and m_{h} since the dependence of $Br(\mathrm{Z}^0 \rightarrow \nu\bar{\nu})$ and $Br(\mathrm{Z}^0 \rightarrow \ell^+\ell^-)$ on these quantities nearly cancels in the ratio. For example, using $m_{\mathrm{t}} = 175 \pm 5.5$ GeV, $m_{\mathrm{h}} = 300^{+700}_{-240}$ GeV and $\alpha_s = 0.119 \pm 0.003$ gives the Standard Model prediction of

$$R^{\mathrm{SM}}_{\mathrm{inv}} = 5.973 \pm 0.003.$$

The errors on the prediction of $R^{\mathrm{SM}}_{\mathrm{inv}}$ from uncertainties on m_{t} and m_{h} are far smaller than the precision with which R_{inv} can be measured. The contribution of the various experimental statistical and systematic errors to the absolute uncertainty in R_{inv} can be expressed as:

$$\Delta R_{\mathrm{inv}} \ \approx \ 6\ \frac{\Delta N_l}{N_l} \ \oplus \ 21\ \frac{\Delta N_{had}}{N_{had}} \ \oplus \ 15\ \frac{\Delta L}{L} \tag{7}$$

where N_l and N_{had} are the numbers of leptonic and hadronic decays observed, corrected for full acceptance, L is the integrated luminosity, and $\oplus$ indicates summation in quadrature. The large coefficients of the hadronic and luminosity terms indicate their relative importance in the measurement. It was equation 7 which originally motivated our interest in improving the OPAL luminosity measurement to be commensurate with the achievable precision in measuring hadronic events. The relative uncertainties ultimately achieved are summarized in table 1. The theoretical uncertainty on the photonic radiative corrections to $\sigma^{\mathrm{pole}}_{\ell^+\ell^-}$ affect the determination of R_{inv} in the same way as the error on the luminosity. Recent theoretical work [?] has significantly reduced this uncertainty to the point where it no longer makes a significant contribution. For the final OPAL LEP I data sample, the errors on the measurements of the luminosity, the number of lepton pair events and the number of multihadron events contribute approximately equally to the uncertainty on R_{inv}, making a 0.4% measurement possible. Because of the small theoretical error on the prediction for R_{inv}, a measurement of R_{inv} which differs from the Standard Model would be a definite indication of new physics.

If the Standard Model couplings for neutrinos and charged leptons are assumed, a measurement of R_{inv} allows the parameter space of other models to be explored. For example, particles which are candidates for cold dark matter and which can be produced in Z^0 decays would contribute to $Br(\mathrm{Z}^0 \rightarrow \mathrm{inv})$. These models are significantly constrained by measurements of R_{inv} [?].

The values of $\sigma^{\mathrm{pole}}_{\mathrm{had}}$ and $\sigma^{\mathrm{pole}}_{\ell^+\ell^-}$ are also insensitive to the values of m_{t} and m_{h}. This can be most clearly seen by noting that the effects of m_{t} and m_{h} on the partial widths are largely independent

Quantity	Relative statistical error ($\times 10^{-4}$)	Relative Systematic error ($\times 10^{-4}$)	Relative (stat. + syst.) error on R_{inv} ($\times 10^{-4}$)
Acceptance corrected hadrons	6	7	34
Acceptance corrected leptons	17	13	21
Luminosity (theoretical)	0	5.4	14
Luminosity (experimental)	3	3.4	9
Photonic correction to $\sigma^{\mathrm{pole}}_{\ell^+\ell^-}$	0	2	6
Total			44

Table 1: Approximate contribution to the relative error on R_{inv} from the various quantities measured by OPAL. Before the introduction of the SiW detector, the experimental luminosity systematic error contributed 103×10^{-4} to the relative error on R_{inv}, and represented the dominant source of error in its measurement.

of the fermion type[2] and therefore affect the numerator and denominator of equation 1 in the same way. In contrast, the final state QCD correction affects only the quarks, giving the hadronic width a unique correction which increases Γ_{had} by a factor of approximately $1 + \frac{\alpha_s}{\pi}$. This correction gives $\sigma^{\mathrm{pole}}_{\ell^+\ell^-}$ sensitivity to the value of α_s through the dominant contribution of Γ_{had} to the total width, Γ_{Z}. Somewhat counter intuitively, $\sigma^{\mathrm{pole}}_{\mathrm{had}}$ exhibits less sensitivity to α_s due to the partial cancellation of the variation induced through Γ_{had} and Γ_{Z}. In table 2 the statistical precision of measurements of α_s using $\sigma^{\mathrm{pole}}_{\mathrm{had}}$, $\sigma^{\mathrm{pole}}_{\ell^+\ell^-}$, and R_{had} are compared. In the absence of systematic errors, $\sigma^{\mathrm{pole}}_{\ell^+\ell^-}$ provides the most precise measurement of α_s. Measurements of α_s based on the quantity R_{had} do not depend on the luminosity measurements, but are less precise than those from $\sigma^{\mathrm{pole}}_{\ell^+\ell^-}$.

In contrast to almost all other quantities used to measure α_s, uncertainties in higher order QCD radiative corrections to Γ_{had} give rise to relatively small theoretical errors on α_s [**?**]. Given the large statistics of the LEP I data sample, the measurement of α_s from $\sigma^{\mathrm{pole}}_{\ell^+\ell^-}$ is one of the most precise.

Alternatively, if α_s is determined from external measurements, the measurement of $\sigma^{\mathrm{pole}}_{\ell^+\ell^-}$ can also be used to constrain anomalous Z^0 decays which would be classified as multihadrons or as an "invisible" decay.

Quantity	Approximate fractional dependence on α_s	Ideal statistical precision of α_s
$\sigma^{\mathrm{pole}}_{\ell^+\ell^-}$	$1 - 1.4\frac{\alpha_s}{\pi}$	$\pi\sqrt{3.6/N_{\mathrm{had}}}$
$\sigma^{\mathrm{pole}}_{\mathrm{had}}$	$1 - 0.4\frac{\alpha_s}{\pi}$	$\pi\sqrt{7.0/N_{\mathrm{had}}}$
R_{had}	$1 + 1.0\frac{\alpha_s}{\pi}$	$\pi\sqrt{6.3/N_{\mathrm{had}}}$

Table 2: The ideal statistical precision of α_s extracted from various quantities expressed as a function of the total number of *hadronic* events recorded, N_{had}. In practice these precisions are degraded by systematic errors and inefficiencies.

1.2 Analysis strategy

The SiW luminometer and the associated luminosity selection were optimized to exploit the characteristics of Bhabha scattering. The small–angle Bhabha cross section is dominated by the t-channel exchange of a photon, which is represented by the first term in the following expression for the Born–level differential scattering cross section:

---

[2] Except for triangle vertex corrections to Γ_{b} which have an explicit m_{t} dependence. The resulting uncertainty is, however, negligable, given the known constraints on m_{t}.

$$\frac{d\sigma}{d\Omega} = \frac{\alpha^2}{2s}\left[\frac{1+\cos^4\frac{\theta}{2}}{\sin^4\frac{\theta}{2}} - 2\frac{\cos^4\frac{\theta}{2}}{\sin^2\frac{\theta}{2}} + \frac{1+\cos^2\theta}{2}\right]. \tag{8}$$

This yields a $1/\theta^3$ angular spectrum, where θ is the angle of the out-going electron and positron with respect to the beam. By instrumenting a region at sufficiently small angles, in our case approximately 25 to 58 mrad, the counting rate from small–angle Bhabha events can be made larger than the rate of Z^0 production, minimizing the contribution of the luminosity measurement to the statistical error of the measured cross sections.

As far as experimental systematic errors are concerned, the forward-peaked $1/\theta^3$ Bhabha spectrum requires that the detector and luminosity analysis define the angle marking the inner edge of the acceptance with particularly high precision. For example, to achieve a precision of 1/1000, the inner edge of the acceptance must be known to 10 μrad (see section 4.1), corresponding to $\sim$ 25 μm in the radial coordinate of the showers generated in the calorimeters located approximately 2.5 m on either side of the interaction region. Similarly, the $\sim$5 m distance between the two luminometers, which is not easily accessible to direct measurement under operating conditions, must be known to better than 2.5 mm.

The theoretical difficulty in ascribing meaning to the trajectory of a bare Bhabha-scattered electron encouraged our fundamental decision to make a calorimetric position measurement, which naturally includes the effects of close-lying radiated photons. But practical limits on the spatial resolution which can be achieved by a calorimeter are about 200μm. Similarly, the physical width of the LEP luminous region itself exceeds 100μm, and the angular divergence of the beams is about 100μrad. Furthermore, the movements of the beam spot with respect to the detector over the course of data taking are on the millimeter scale. These effects are all much larger than the basic precision with which the Bhabha scattering acceptance angle must be defined. Only by ensuring that they influence the detector acceptance in second-order is a luminosity measurement surpassing a precision of 1/1000 possible. This is achieved by constructing the detector to be as symmetrical and homogeneous as possible (section 2). The azimuthal symmetry of the detector, coupled with the event selection described below in section 1.3, minimizes the effects of beam offset on the luminosity (section 7). Careful reconstruction of the radial coordinate (section 4.1) gives a resolution function which is nearly symmetric around the inner and outer radial cuts. The goal here is not to attain the highest possible resolution, but rather to minimize any possible bias. In the end our chief success is to demonstrate that the net bias in our angular acceptance boundary is less than 4% of our resolution.

Apart from the determination of the radial acceptance of the detector, the most important measurement is that of energy (section 4.3). As discussed in sections 1.3 and 5, the background from off-momentum beam particles requires that rather tight energy cuts be applied. Even in the absence of this background, energy cuts would be required to reduce the sensitivity of the selection to radiative Bhabha events with small values of t-channel momentum transfer. The systematic error arising from the imprecision with which we understand the low energy tails of the detector energy response is reduced by imposing a cut on the acollinearity of the scattered electrons, which causes our acceptance for radiative events to be determined by geometry rather than energy.

Another consideration is the treatment of events with multiple showers in one (or both) of the calorimeters. Here we exploit the fine granularity of our detector to reject spurious electromagnetic showers from off-momentum beam particles, while retaining showers from final state radiation. Using this approach (section 3), the dependence of the luminosity measurement on the theoretical description of final state radiation and on the off-momentum background is minimized.

The SiW detector and luminosity analysis were designed to provide sufficient redundancy and internal consistency checks to allow the performance of the detector to be closely monitored. Here we cite a few examples. The fine radial and longitudinal granularity of the detector are exploited to produce precise and continuous radial coordinates. This allows the acceptance of the luminosity selection to be probed by varying the inner and outer radial cuts (section 4.1.4). The continuous radial coordinate also allows us to exploit radiative and non-radiative Bhabha events to measure the energy response and linearity of the detector during OPAL operation, as illustrated in section 4.3. Finally, extensive monitoring of trigger signals allows us to measure the background from random coincidences of off–momentum beam particles (section 5) as well as to measure the efficiency of the trigger signals (section 6).

The luminometer acceptance calculation for Bhabha scattering was designed to be as direct as possible. The simulation of electromagnetic showers in this calculation is based on a parametrization of the detector response obtained from the data, rather than the usual approach of utilizing a detailed Monte-Carlo simulation of shower development. This approach gives a much more reliable description of the tails of the detector response functions, which are primarily due to extreme fluctuations in shower development, than we could obtain using any existing program which attempts to simulate the basic interactions of photons and electrons in matter. The measured LEP beam size and divergence, as well as the measured offset and tilt of the beam with respect to the calorimeters are also incorporated into this simulation. This approach, described in section 8, allows us to propagate the uncertainties in the measurements through to the final luminosity error in a transparent manner. As discussed in section 4.1.4, the radial coordinate bias is determined directly from data and explicitly accounted for. The Monte Carlo, therefore, is only used to further correct the acceptance for the effects of the detector energy response, LEP beam parameters and coordinate resolution.

The largest acceptance correction generated by the differences between the raw four-vectors and the reconstructed detector response is of order -5×10^{-4} and due mostly to the finite resolution of the energy measurements in the two calorimeters. A detailed parameterization of the energy response of each calorimeter is required in order to obtain a reliable calculation of this correction. This is discussed in section 4.3. The residual effect of the LEP beam parameters on the acceptance is of similar magnitude, but opposite sign. In section 7 we demonstrate that the effect of beam parameters on the acceptance has been understood and accounted for.

The overall acceptance correction is of order $\sim 2 \times 10^{-4}$ and is largely independent of the details of theoretical input. This will allow future improvements in the theoretical understanding of Bhabha scattering to be incorporated into our results. The interplay between the theoretical and experimental components of our acceptance calculation is discussed in section 9.1.

In the remainder of this paper, the detector and luminosity analysis are systematically described. We begin in section 2 with the detector design and construction. Also included in this section are the axial and radial metrology of the detector. In sections 3 and 4 event reconstruction and the measurement of shower coordinates and energy are described. In sections 5, 6 and 7, the sensitivity of the measurement to background, trigger efficiency and the LEP beam parameters is discussed. This is followed by a discussion of the detector simulation in section 8. In section 9 we discuss the calculation of the acceptance and summarize the experimental and theoretical systematic errors. Finally, in section 10 we discuss the properties of the selected sample of Bhabha scattered events.

One exception is made to this systematic description of the analysis. We pause here to describe the final event selection. This would logically follow the section on event measurement, but by introducing the event selection now we simplify and motivate much of the following discussion.

1.3 Bhabha event selection

The event selection criteria can be classified into *isolation* cuts which isolate a sample of pure Bhabha scattering events from the off-momentum background, and acceptance defining, or *definition* cuts. The isolation cuts are used to define a fiducial set of events which lie within the good acceptance of both calorimeters and are essentially background free. The definition cuts then select subsets of events from within the fiducial sample. As the nomenclature suggests, the characteristics of the definition cuts largely determine the quality of the measurement. Showers generated by incident electrons and photons are recognized as clusters in the calorimeters (section 3) and their energies and coordinates determined (section 4). The fine segmentation of the detectors allows incident particles with separations greater than 1 cm to be individually reconstructed with good efficiency.

The coordinate system used throughout this paper is cylindrical, with the z-axis pointing along the direction of the electron beam, passing through the centers of the two calorimeter bores. The origin of the azimuthal coordinate, ϕ, is in the horizontal plane, towards the inside of the LEP ring. All radial coordinate measurements are projected to reference planes at a distance of ±246.0225 cm from the nominal intersection point. These reference planes correspond to the nominal position of the silicon layers 7 X_0 deep in the two calorimeters.

The *isolation* cuts consist of the following requirements, imposed on (R_{R},ϕ_{R}) and (R_{L},ϕ_{L}), the radial and azimuthal coordinates of the highest energy cluster associated with the Bhabha event, in each of the right and left calorimeters, and on E_{R} and E_{L}, the total fiducial energy deposited by the Bhabha event in each of the two calorimeters, explicitly including the energy of radiated photons:

- Loose radial cut, right (left) $6.7\ \mathrm{cm} < R_{\mathrm{R}} < 13.7\ \mathrm{cm}$
  $(6.7\ \mathrm{cm} < R_{\mathrm{L}} < 13.7\ \mathrm{cm})$
- Acoplanarity cut $||\phi_{\mathrm{R}} - \phi_{\mathrm{L}}| - \pi| < 200\ \mathrm{mrad}$
- Acollinearity cut $|R_{\mathrm{R}} - R_{\mathrm{L}}| < 2.5\ \mathrm{cm}$
- Minimum energy cut, right (left) $E_{\mathrm{R}} > 0.5 \cdot E_{\mathrm{beam}}$
  $(E_{\mathrm{L}} > 0.5 \cdot E_{\mathrm{beam}})$
- Average energy cut $(E_{\mathrm{R}} + E_{\mathrm{L}})/2 > 0.75 \cdot E_{\mathrm{beam}}$

Note that by defining the energy cuts relative to the beam energy, E_{beam}, the selection efficiency is largely independent of $\sqrt{s}$.

The acollinearity cut (which corresponds to approximately 10.4 mrad) is introduced in order to ensure that the acceptance for single radiative events is effectively determined geometrically and not by the explicit energy cuts.

The *definition* cuts, based solely on the reconstructed radial positions $(R_{\mathrm{R}}, R_{\mathrm{L}})$ of the two highest energy clusters, then distinguish two classes of events which we count to determine the luminosity.

- SwitR $7.7\ \mathrm{cm} < R_{\mathrm{R}} < 12.7\ \mathrm{cm}$
- SwitL $7.7\ \mathrm{cm} < R_{\mathrm{L}} < 12.7\ \mathrm{cm}$

The SwitR and SwitL[3] *definition* cuts have been chosen so as to correspond closely (within $\approx 20\mu$m) to radial pad boundaries (see section 2) in the silicon layers at the reference planes 7 X_0 deep in the calorimeters. Expressed in terms of polar angles, these cuts correspond to 31.288 and 51.576 mrad.

The luminosity is measured from the average of the SwitL and SwitR counters, i.e.,

$$L_{\mathrm{RL}} \equiv \frac{1}{2A_{\mathrm{RL}}} \left(N_{\mathrm{SwitR}} + N_{\mathrm{SwitL}}\right) \tag{9}$$

where N_{SwitR} and N_{SwitL} are the numbers of events which satisfy each of the selections and the *acceptance*, A_{RL}, is the average of the theoretically calculated Bhabha cross sections accepted by the SwitR and SwitL selections, corrected for all effects of detector response and LEP beam parameters. Because a detailed study of the bias in the SwitR and SwitL definition cuts is possible, L_{RL} is used for the primary luminosity measurement.

A secondary luminosity measurement is defined in terms of the average of the radial positions of the clusters at the reference planes of the right and left calorimeters, (R_{A}). The counter, called SwitA has a definition cut given by:

$$7.7\ \mathrm{cm} < R_{\mathrm{A}} \equiv \frac{(R_{\mathrm{R}} + R_{\mathrm{L}})}{2} < 12.7\ \mathrm{cm}$$

---

[3] The “it” in the “SwitX” acronyms stands for in-time coincidences, to distinguish these from the corresponding selections used for the analysis of off momentum particle backgrounds. See section 5.

The corresponding luminosity measurement is defined as

$$L_{\mathrm{A}} \equiv \frac{N_{\mathrm{SwitA}}}{A_{\mathrm{A}}} \tag{10}$$

where the acceptance, A_{A}, is the calculated Bhabha cross section of the SwitA selection, corrected for all effects of detector response and LEP beam parameters. The SwitA selection has the advantage that the radial cut is effectively made in the beam-centered frame and therefore A_{A} is largely free of beam spot corrections. A second advantage of the SwitA selection is that it defines a unique sample of left/right symmetric events, and is frequently used in the evaluation of systematic errors such as those related to energy reconstruction. Since the L_{A} and L_{RL} selections have largely complementary sources of systematic error with respect to the acceptance–defining cuts, the comparison of the two selections can be used as a check on our understanding of coordinate bias and the effects of the LEP beam parameters on the luminosity measurement.

1.4 Data samples

In this paper we consider data taken during the 1993, 1994 and 1995 runs of the LEP collider. In 1993 and 1995, energy scans were performed and substantial amounts of data were taken at two energy points approximately 1.8 GeV above and below the Z^0 peak. In the following, we divide the data into nine different samples which have slightly different characteristics.

In the 1993 and 1995 scans, each energy point has been analyzed separately. This allows us to account for any differences in the selections at the different energies, including those induced by changes in the LEP beam parameters (section 7).

The 1994 data were all taken near the Z^0 peak. These data have been divided into three different samples. The first two samples are necessary because of a large change which occurred in the average vertical offset of the LEP beam at the OPAL intersection point (see section 7). The third sample corresponds to approximately the last month of running in 1994. In this period LEP changed from 8 bunch running to 4 bunch running in preparation for operating with bunch-trains in 1995. In addition, the OPAL Silicon-Microvertex Detector was removed for repairs, significantly reducing the amount of material in front of the left calorimeter.

A precise determination of the OPAL luminosity has not been undertaken for data recorded before stable LEP operation was achieved preceeding the 1993 and 1995 energy scans. The 1993 "prescan" period was used to achieve stable operation with the newly installed SiW luminosity monitor and the 1995 prescan period was used to commission the readout necessary for understanding operation of the luminosity monitor with bunch trains.

The number of luminosity and multihadron events recorded in each of the samples is given in table 3.

2 Detector

2.1 Physical construction

The SiW Luminometer consists of two cylindrical small–angle calorimeters encircling the beam pipe at approximately ±2.5 m from the interaction point. Each calorimeter is a stack of 19 layers of silicon sampling wafers interleaved with 18 tungsten plates, and mounted as two interlocking C-shaped modules around the LEP beam pipe. The first sampling layer lies in front of the first layer of tungsten to provide improved presampling of the energy lost in upstream material. One such calorimeter is shown in figure 1. Electromagnetic showers, initiated by small–angle Bhabha scattered electrons, are almost totally contained within the 140 mm sensitive depth of the detector, which represents 22 radiation lengths (X_0). The first 14 tungsten plates are each 1 X_0 thick, while the last 4 are each 2 X_0 thick. The sensitive area of the calorimeter fully covers radii between 62 and 142 mm from the beam axis.

Sample	Energy (GeV)	Multihadrons	SwitR	SwitL	SwitA
93 −2	89.45	84710	697370	699041	702729
93 pk	91.21	262735	689570	690487	694568
93 +2	93.04	123895	682445	683642	687282
94 a	91.24	267413	698423	701928	704489
94 b	91.22	1238184	3238878	3252718	3267218
94 c	91.43	11135	29066	29211	29293
94 c'	91.22	68324	177864	178154	179199
95 −2	89.44	83254	691317	690522	695735
95 pk	91.28	139328	362725	362853	365130
95 +2	92.97	126305	677469	675479	680982
Total		2405283	7945127	7964035	8006625

Table 3: The mean center-of-mass energy and numbers of multihadron and luminosity events recorded in the 1993, 1994 and 1995 data samples. For the purposes of the luminosity analysis the c and c$'$ data samples have been analyzed together. They are split in two when fitting the lineshape because of the large change in beam energy which occured in the middle of this sample.

Mechanically each half calorimeter, or "C", consists of 19 half-layer assemblies. Each half-layer consists of a precisely machined tungsten half-disk glued to the inner radius of a 2 mm thick aluminum support plate. The edges of the tungsten half disks that mate when the two C's close are bevelled so that projective cracks in the absorber are eliminated. The plate carries eight overlapping detector wedges and a semicircular printed circuit board. The detector wedges physically overlap, so that the active areas of all adjacent wedges are contiguous. The four C's contain a total of 608 detector wedges. Each is a large, thick-film, ceramic hybrid carrying a 64-pad silicon wafer diode, four AMPLEX readout chips and about 130 other electronic components. The pad layout of the silicon diodes is shown in figure 2. The pads have a radial pitch of 2.5 mm, and are arranged in an $r - \phi$ geometry. The diodes were fabricated by the Hammamatsu Corporation, and have proved to be extremely reliable. The average leakage current at 22°C and 80 V bias was 0.7 nA/pad (1 nA/cm^2) when the detector was installed. In the entire sample of 785 delivered diodes (50,240 pads) the largest leakage current for a single pad was 12 nA. Radiation damage from catastrophic losses of the stored beam into the calorimeters during seven years of operation at LEP has increased the total leakage current by about a factor of ten, but only three pads now exceed the AMPLEX bias current limit of $\sim 200\,\text{nA/pad}$.

Every second layer is rotated by 11.25 degrees, (half the silicon wafer angle) to reduce any systematic effects which might be introduced by the physical overlapping of adjacent wafers in each layer. As each wafer contains two azimuthal segments, the azimuthal and radial structure of the pads in each layer is identical. The projective structure of the azimuthal segmentation of the detector facilitates the cluster and coordinate reconstruction described in sections 3 and 4. The radial segmentation of the detector is cylindrical, but the approximate projective geometry with respect to the interaction point can still be exploited by the clustering algorithm. The lack of radial projectivity is in fact crucial to our ability to reconstruct a continuous radial coordinate with minimal systematic uncertainty (see section 4.1.2).

Two 15 mm precision dowels penetrate the entire stack, including the aluminum front and rear plates, to hold the half-layers in alignment (see figure 1). Distortion of each half-layer out of a plane is limited by spacers at the inner and outer radii. Spring loaded clamps on each of the sixteen 3.0 mm cooling pipes which penetrate the detector constrain the position of each layer along the detector axis. These clamps also ensure adequate thermal conductivity to the cooling water.

The two C's slide together on two massive brass dowels which ensure that the silicon wafers, which overlap as the detector is closed, do not violate their 300 μm clearances during assembly around the beam pipe. The relative alignment of the C's in the direction of closure is crucial in determining the radial geometry, and is determined by clamping the C's together against massive and precisely machined lips on the upper and lower support blocks. This method of alignment is an order of magnitude more precise than the $\sim 10\ \mu$m commonly achieved by conventional techniques of doweling transversely to the closing direction.

Sixteen 3 mm diameter water cooling pipes penetrate each calorimeter C at a radius of 220 mm to remove the 170 Watts generated by the front end electronics as close as possible to the source. During operation 3 ℓ/min of cooling water per C flows through the detector. The nominal temperature of the cooling water is 16 °C. Maximum temperature differences within the detector are measured to be less than 2.0 °C. During operation of the detector at LEP, the temperature of each half ring is monitored with thermistors located either near the coolest or the warmest part of the half ring, allowing the temperature gradients within the detector to also be monitored. Due to the slow accumulation of debris in the filter of the heat exchanger used to cool the 16 °C water, the average temperature of the half-planes slowly increased from 22.5 °C, at the start of 1993 scan, to 24.5 °C at the end of 1995 scan, when the reason for the temperature increase was understood and corrected.

The effect of temperature on the radial metrology is discussed below in section 2.3.

2.2 Beam pipe and upstream material

An important consideration in the design of the SiW calorimeters, over which we had little control, was the location of material associated with the existing parts of the OPAL detector. A flared beam pipe which would have allowed particles to exit the beam pipe at normal incidence was ruled out by the installation logistics of the OPAL microvertex detector. Instead, the material traversed by particles originating at the interaction point was reduced by extending the beryllium portion of the cylindrical OPAL beam pipe and modifying its supports. The distribution of material upstream of the calorimeters is shown in figure 3. Note that in the crucial region of the inner acceptance cut the upstream material totals approximately 0.25 radiation lengths. It was not possible to further reduce the shadow cast in the middle of the detector's radial acceptance by the microvertex detector cables and by the flanges and support structures of the OPAL pressure pipe [?]. Fortunately, the reconstruction of the shower position remains largely unaffected by this additional material (see section 4.1). Furthermore, this region is not crucial for the LEP I luminosity measurement. The effects of the degraded energy resolution are important, but measurements of the longitudinal development of the showers can be used to correct for energy which is deposited in this dead material (see section 4.3).

2.3 Radial metrology

One of the most demanding aspects of the SiW luminosity measurement is to establish the absolute radial dimensions of the detector. The details of our techniques and measurements can be found in reference [?]. Here we give a simplified description of the two essential steps of the metrology: determining the geometry of the detector under ideal conditions in the laboratory, and monitoring the changes which occur when the detector is brought into operation at LEP.

2.3.1 Laboratory measurements

The geometry of the Si wafers themselves can be defined very precisely. The semi-conductor industry routinely fabricates diode structures across the full width of a 10 cm Si wafer with sub-micron geometrical precision, and electrostatic calculations confirm that the sensitive boundaries of the detector pads correspond within a fraction of a micron with the midline of the 50μm inter-pad gap. Sharply defined visible boundaries in the detector aluminization are created above the diode implants in a subsequent photo-lithographic step, and provide convenient visible references which are directly related to the diode boundaries.

We used several microscopes mounted at fixed radii on stable rotating arms to align and measure each of the 608 silicon wafers in the luminometer using these visible references. All wafers were

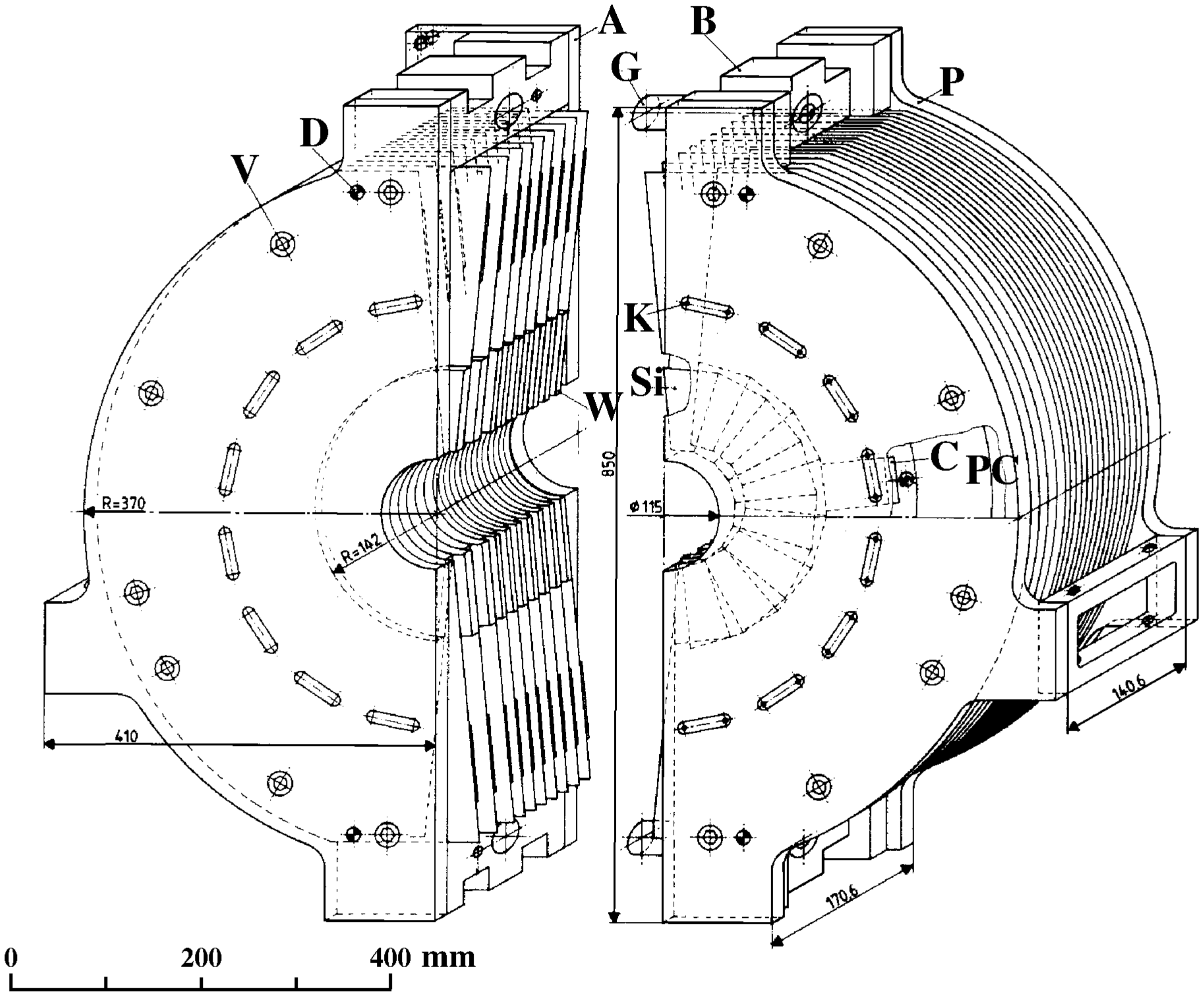

Figure 1: An isometric view of one of the SiW calorimeters, separated into two C's, **A** and **B**. The 15 mm precision dowels which radially align the individual half layers are labeled as **D**. The holes for the cooling pipes are labelled as **K**. The clamps which fix the axial position of the half layers on the cooling pipes are not visible. The axial position of the half layers is also constrained by bolts and spacers at locations **V**, as well as by spacers at the inner bore. One of the brass dowels which align the two C's is labelled as **G**. On the left C, the beveled edges of the tungsten layers are visible and labeled as **W**. The silicon diode wedge structure in two successive layers is shown on the right C and labelled **Si**. Also shown on the right C is a PC motherboard (**PC**) and the ceramic hybrid (**C**). The dimensions shown on the figure are mm.

individually measured during construction in 1993. A sizable fraction were remeasured twice in 1994, and all of the wafers used in coordinate determination were remeasured twice in 1995. A smaller set was remeasured in 1996.

The absolute radii of the microscopes were calibrated and monitored against a calibration plate, whose dimensions were determined with an interferometer, and checked against the principal metrology instrument of the central CERN Metrology lab. The absolute radius swept out by the primary microscope graticule is

$$R_{\rm micro} = 142.0305(19)\text{mm at } T = 21.5\,^{\circ}\mathrm{C}$$

where the quoted error includes the effects of the absolute uncertainty in the radius of the calibration plate (0.7μm), the allowance for possible calibration plate distortions (1μm), and the uncertainty in the long term stability of the microscope (1.45μm).

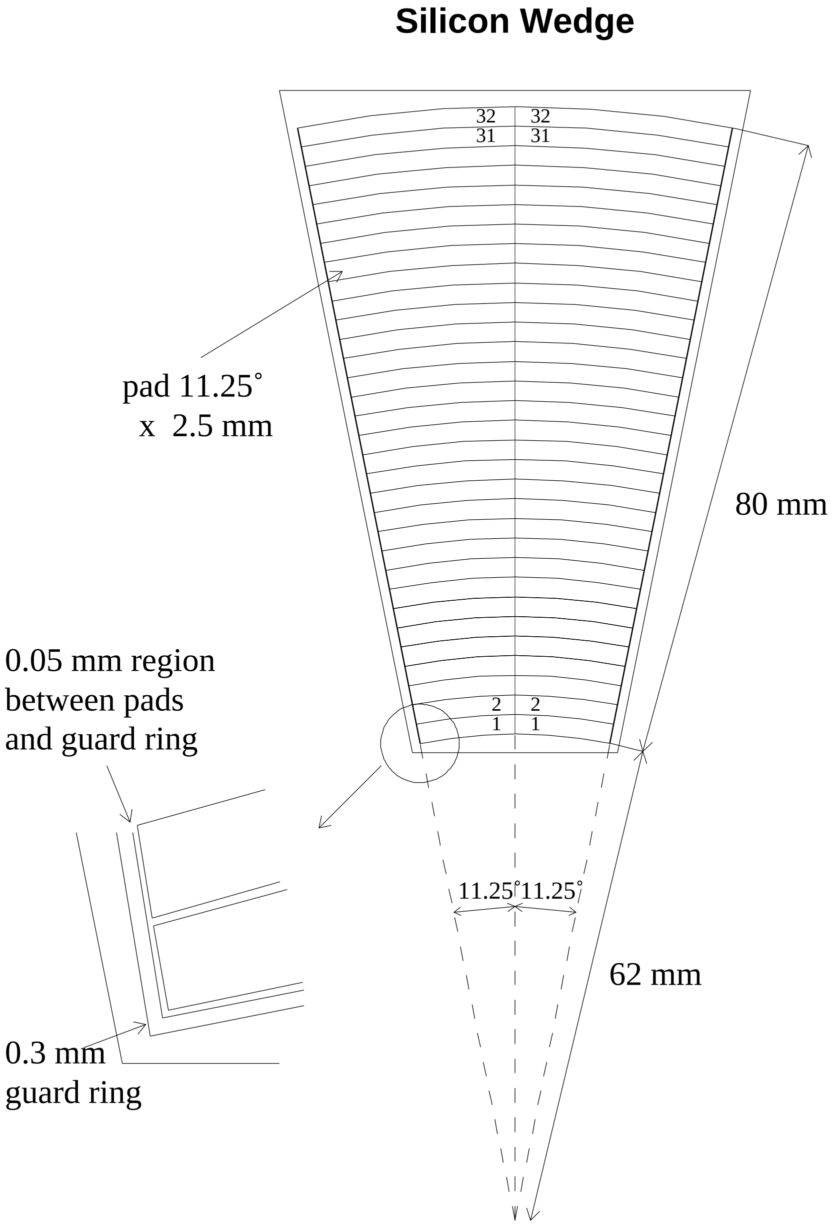

Figure 2: A schematic illustration of the silicon diode pad geometry. The silicon detectors are divided into 2 rows of 32 pads, each covering 11.25° in azimuth. The radial pad segmentation is 2.5 mm. Silicon detectors within each layer of the calorimeter are physically overlapped, so that the azimuthal boundaries of their active regions coincide and there are no dead or "double counted" regions.

The calorimeters each consist of two stacks of half rings, on which the silicon detectors are mounted. Within each stack, individual silicon detectors were verified to lie on the best–fit semicircle with an RMS scatter of about 1.3μm, as shown in figure 4. When the two calorimeter halves are brought

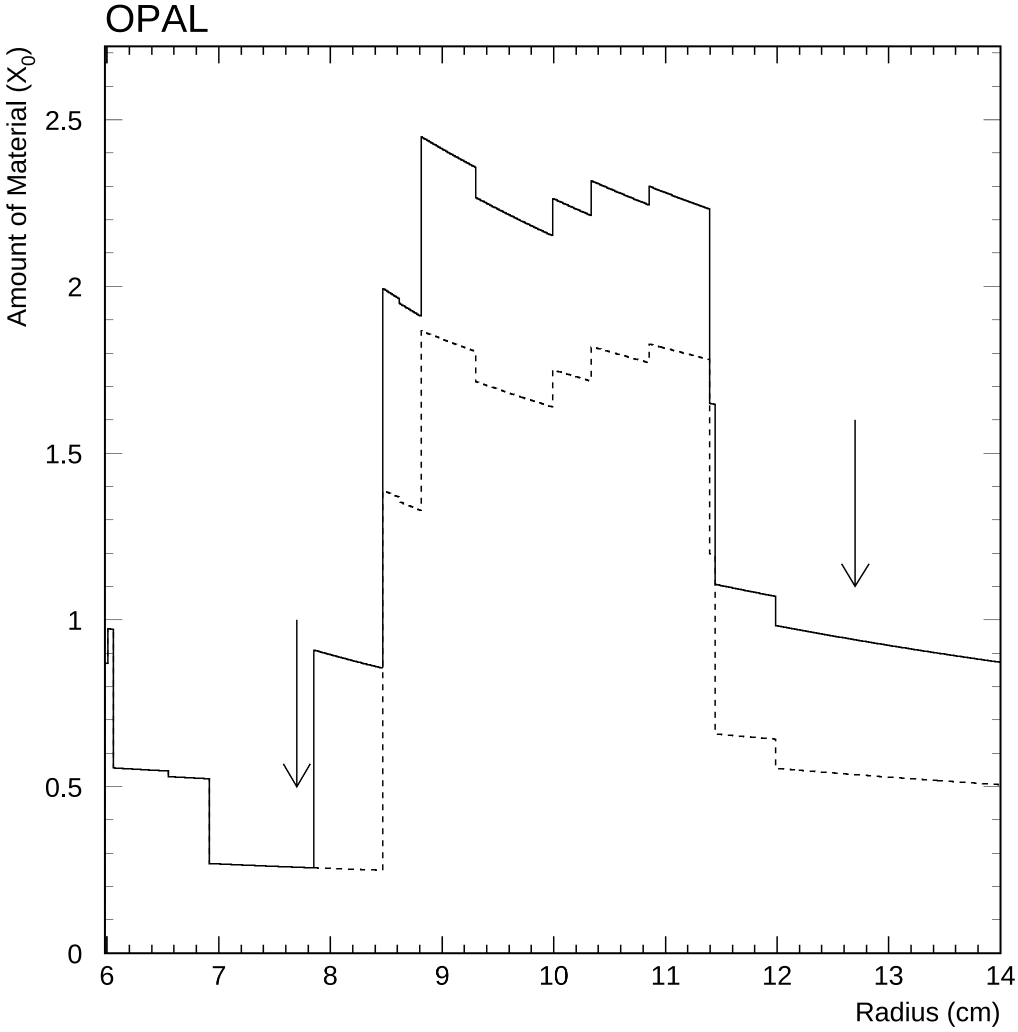

Figure 3: The calculated material traversed by particles originating at the interaction point as a function of calorimeter radius, measured at the reference plane (246 cm) for the 1993–1994 detector configuration. The solid curve corresponds to the left, the dotted curve to the right side. The larger amount of material on the left is due to the passage of cables from the OPAL microvertex detector. The arrows show the location of the acceptance definition cuts on shower radius.

together, there is some residual misalignment of the two halves with respect to each other. These misalignments are on the order of $10-20\mu$m, and are quite reproducible over time. When integrated in azimuth, the higher order corrections to the detector acceptance introduced by the relative separation and shear between half-rings (Δx_c ,Δy_c) are less than 10^{-6} so that only the average radial position of each layer of silicon detectors needs to be taken into account.

Variations in the individual half-ring separations in each layer as observed each time the layer is stacked or unstacked produce an RMS variation in layer radius of 1.9μm. The uniformity with which the separation between the two completed C's of each calorimeter can be preserved when the detector is liberated from the stacking fixture produces a further RMS variation in radius of 1.5μm.

Figure 5 shows the distribution of the average radius measured for each of the 38 layers. The RMS of 2.4μm is due mostly to actual differences in the layer radii, since the error on each entry is typically less than 1μm.

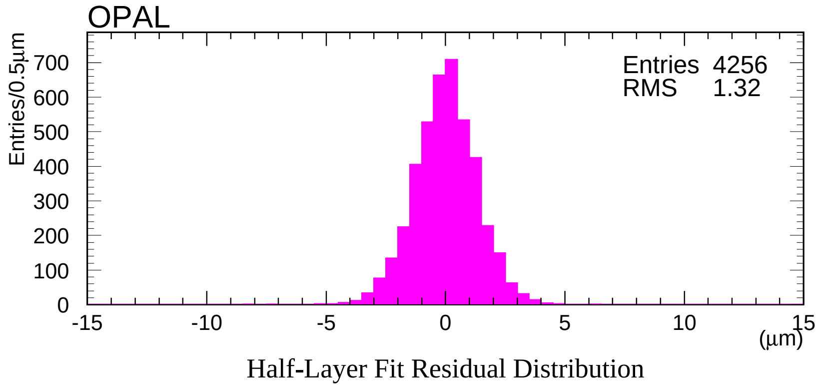

Figure 4: The residuals of the individual detector radii from the fit half-circles for all the standard metrology measurements. The RMS of 1.32μm includes the relative precision achieved in placing the the individual detectors on each half-ring, as well as the resolution of the subsequent measurements of their positions.

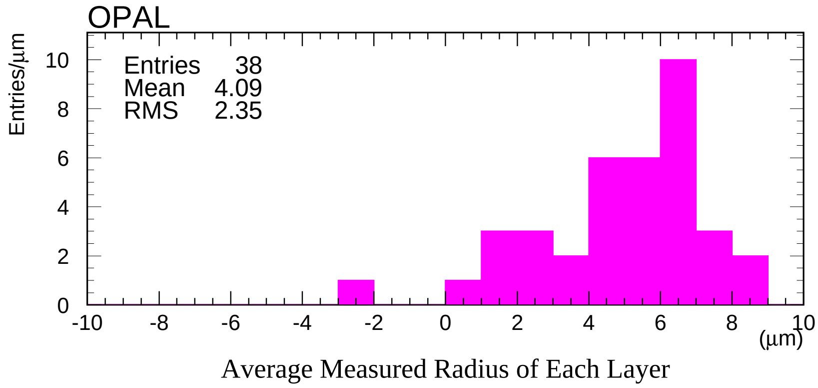

Figure 5: The distribution of the average measured radii for each layer with respect to R_{micro}. The RMS of 2.4μm is due mostly to actual differences in the layer radii, since the error on each entry is typically less than 1μm. The abscissa is in units of μm relative to the microscope graticule.

A list of the most interesting parameters for layer 7 in the two calorimeters is shown in table 4. The entries are from the average of all the measurements made on these layers. The layer 7 radii, alone, determine the actual luminometer acceptance boundary (see section 4.1). The difference of each layer's radius with respect to layer 7 propagates to the study of coordinate systematics (the coordinate "anchoring" described in section 4.1.4). Since the luminometer acceptance is determined by the *average* of the right and left radii of the layer 7 pad boundaries, nominally at 77 mm, we take

$$R_{\mathrm{std}} = 77.000\mathrm{mm} + \frac{1}{2}(5.0 + 4.7) \times 10^{-3}\mathrm{mm} = 77.0048(32)\mathrm{mm}$$

as the effective acceptance radius of the luminometer in standard metrology conditions. The quoted error takes into account the effects of the absolute uncertainty in items *a*-*f* of table 6. The actual acceptance radius will differ from R_{std} due to dimensional changes associated with bringing the detector from standard metrology conditions into operation at LEP.

The small annual changes in the detector radius measured under standard metrology conditions are well within the systematic errors we assign to the stability of our absolute radial scale. We found no evidence that the detector suffered any change in its standard metrology radius as a function of time.

2.3.2 Measurements in LEP operating conditions

The largest single source of uncertainty in the detector radius arises from the difficulty of measuring the dimensional changes which occur when the calorimeters are removed from the laboratory and brought into actual operation at LEP. We have nevertheless made such measurements, and do not rely simply on assumptions.

The first change required in bringing the detector into operation is to rotate the calorimeter from horizontal to vertical, which radically changes the mechanical loading placed on the main alignment dowels. After rotating each calorimeter, the standard metrology measurements were carried out on the first layer. The relative motion of survey marks glued to the inner bore on deeper layers were also observed.

With each calorimeter in the vertical position, the flow of cooling water was established, the front-end electronics were powered and the detector allowed to come to thermal equilibrium. The mean temperature of the inner and outer thermistors increased by 0.5°C and a thermal gradient of ~ 2.0°C was established. The first layer metrology and the bore measurements were then repeated.

Some of the measured effects may be artifacts resulting from the non-ideal metrology fixtures arranged for these tests. The non-redundant nature of these measurements also precludes extracting reliable estimates of systematic measurement errors from the observed scale of fluctuations, and we have quoted errors representative of measurement uncertainties achieved with the same equipment, but in better conditions. We then take a conservative approach by taking the scale of the uncertainties from the differences observed in the behavior of the two calorimeters, rather than from the estimated measurement errors. Table 5 summarizes the observed changes. Averaging over the two calorimeters, we estimate a radial change of $-9 \pm 3\,\mu$m in bringing the luminometer from metrology conditions into actual operation, where the error is half the observed difference between the two calorimeters.

Calorimeter no.	Layer 7 radius(μm)	1/2 Ring A radius(μm)	1/2 Ring B radius(μm)	$\Delta x_c = x_c(A) - x_c(B)$ (μm)	$\Delta y_c = y_c(A) - y_c(B)$ (μm)
Right	5.0 ± 0.9	1.2 ± 0.9	0.1 ± 0.7	13.0 ± 3.3	8.7 ± 2.1
Left	4.7 ± 0.9	2.4 ± 0.5	1.1 ± 0.6	7.7 ± 3.4	18.7 ± 1.2

Table 4: Average results for fits to the metrology data taken for layer 7 of the two half rings. The two half-rings of each calorimeter are designated "A" and "B". The coordinates (x_c,y_c) give the centers of the half-circles fitted to the detectors of each half-ring. The x-axis is parallel to the direction of closure. The errors are the RMS errors in the mean, evaluated from the spread observed in the fit results. The errors *do not* include the uncertainty in the absolute radial scale. All the radii are to be read as microns above 77 mm. They are valid in standard metrology conditions, detector closed, at $T = 21.5\,^\circ$C.

The inner acceptance radius of the luminometer in normal operating conditions is then

$$R_{\rm in} = 76.9958(44)\ \text{mm at T} = 22.0^\circ\text{C}.$$

where the quoted error takes into account the effects of items *a-g* in table 6.

The temperature of the luminometer was continuously monitored during operation, and the precision solid-state resistive temperature probes were carefully cross-calibrated to the thermometer used when the absolute radius of the calibration plate was determined. The changes in the acceptance radii (77 and 127 mm) as a function of operating temperature were measured to be

$$\Delta R_{\rm in} = 3.9[\mu\text{m}/\,^\circ\text{C}] \times (T_{avg} - 22.0\,^\circ\text{C})$$

	ΔR_1 (μm)	ΔR_2 (μm)
Stack rotation (horizontal to vertical)	-1 ± 1	-7 ± 1
Thermal loading	-5 ± 1	-5 ± 1
Total measured radial change	-6 ± 1	-12 ± 2

Table 5: Summary of the different contributions to the radial change observed for the top layer radius of calorimeter 1 and 2 (right and left) in going from standard metrology to operating conditions. Stack rotation refers to moving the detector from the horizontal (standard metrology) to the vertical (operational) position.

$$\Delta R_{\rm out} = 4.1[\mu{\rm m}/\,^\circ{\rm C}] \times (T_{avg} - 22.0\,^\circ{\rm C})$$

with respect to normal operating conditions. The mean temperature of each data sample was determined and the acceptance corrections (less than 3×10^{-4}, as shown in table 23) are calculated on the basis of the relations given in section 4.1. The systematic errors listed in table 24 reflect a 0.1 °C uncertainty in the average operating temperature and a 10% uncertainty in the measured thermal expansion coefficient. The smallest error (for 1993 pk) is taken as a component correlated among all data samples.

The SiW luminosity acceptance calculation assumes that the inner and outer acceptance radii are exactly 77.000 and 127.000 mm. Apart from the operating temperature correction just discussed, it is therefore necessary to apply a base metrology correction which reflects the 4.2μm difference between the actual and nominal dimensions, as well as a small correction which accounts for the difference between an ideal circular pad geometry and the actual polygonal pads implemented in the detector fabrication masks, with chord lengths of $\sim 1^\circ$. This base radial metrology acceptance correction, $\Delta A/A$, at $T_{avg} = 22.0\,^\circ$C is

$$\frac{\Delta A}{A} = (+1.55 \pm 1.40) \times 10^{-4}$$

which is to be applied to all data taken between 1993 and 1995 (in addition to the operating temperature corrections which are time dependent).

Diligent attention to the mechanical and thermal stability of the detector has allowed us to reduce the uncertainty in the geometry of the luminometers more than a factor of 5 beyond the level which would have compromised our goal of a 0.1% luminosity measurement. The inner radius of the luminometer acceptance region is determined with a precision of 4.4 μm taking into account mechanical deformations, temperature effects, and the precision of the optical apparatus used for the survey. This uncertainty in the acceptance radius contributes a systematic error of 1.4×10^{-4} to the OPAL luminosity measurement during 1993-1995. Table 6 gives the components of the total uncertainty in the detector radius.

2.4 Axial metrology

The metrology which determines the separation of the detectors in z, along the beam axis, is described in detail in reference [?]. Briefly, the measurement is based on interferometric and Johansson bar measurements of the distance between flanges on the OPAL beam and pressure pipes [?]. These pipes are then used as rulers to measure the distance between the calorimeters during operation. The pressure pipe, which forms the primary length reference, has a length of 473.9858(62) cm at 22.3°C. Optical grating position monitors with 0.5 μm resolution are used to measure the position of the calorimeters with respect to these pipes during detector operation. These monitors must track the relative motion of the calorimeters as the expansion of the central detector pressure vessel during its

Item	Systematic sources	ΔR
a	Calibration plate radius	$0.7\,\mu$m
b	Calibration plate distortions	$1.0\,\mu$m
c	Microscope stability	$1.45\,\mu$m
d	Half-ring separation stability	$1.9\,\mu$m
e	Cover plate reproducibility	$1.5\,\mu$m
f	Layer 7 measurement error	$0.6\,\mu$m
g	Changes between metrology & operation	$3.0\,\mu$m
h	Operating temperature expansion	$0.4 - 0.8\,\mu$m
i	Low detector polygon correction	$0.25\,\mu$m
	Total radial metrology systematic error	$4.4\,\mu$m
	Corresponding error in acceptance	1.4×10^{-4}

Table 6: Summary of the systematic errors for the radius measurements in standard operating conditions.

Systematic sources	1993–4	1995
Position of layer 7 relative to calorimeter reference face	$34\,\mu$m	$60\,\mu$m
Length of the pressure and beam pipes	$31\,\mu$m	$31\,\mu$m
Position monitor stability	$5\,\mu$m	$2\,\mu$m
Reference pipe temperature during calibration	$10\,\mu$m	$0\,\mu$m
Reference pipe temperature during operation	$15\,\mu$m	$4\,\mu$m
Total axial metrology systematic error	$50\,\mu$m	$68\,\mu$m
Corresponding error in acceptance	0.41×10^{-4}	0.55×10^{-4}

Table 7: Summary of errors in correcting the nominal 246.0225 cm half-distance between the layer 7 reference planes of the two calorimeters

pressurization to 4 bar carries them away from each other by about 10 mm. The length of the pipe is corrected for thermal expansion based on measurements from probes located on the pipe.

Corrections to the nominal detector half-separation of 246.0225 cm are made with a precision of approximately 60 μm on the basis of these measurements, corresponding to an uncertainty of about 5×10^{-5} in the luminosity. The contributions to the systematic error from the axial metrology are listed in table 7.

2.5 Front end electronics

The detector is read out using front-end electronics [?] based on the AMPLEX [?] chip. Each AMPLEX contains 16 channels which comprise a charge amplifier, a shaping amplifier and a track and hold. Four AMPLEX chips are mounted on each ceramic allowing signals from the 64 pads on each silicon detector to be multiplexed to the common output. The gain of the amplifier has been matched to signals expected from 45 GeV electromagnetic showers [?]. At shower maximum, a single layer of the calorimeter typically records a signal equivalent to 300 to 400 minimum ionizing particles (mips) or $\sim$ 1.0 to 1.3 pC for an incident electron of 45 GeV, and this is spread over a few pads (see section 3). The signal seen by an individual pad was well below the full scale limit of the AMPLEX and the ADC used to digitize the signal, which corresponds to more than 1000 mips.

Despite the large dynamic range of the signals, the equivalent noise for each channel remained at a level of 1500 to 2000 electrons for a typical detector capacitance of 20 pF, giving better than 10:1 signal to noise for mips. While the detection of single mips was not crucial in OPAL operation, the good response of the detectors to muons was essential for the precision alignment of the detectors in the test beam studies described in section 4.1.4.

The response of the AMPLEX to injected charge has been characterized with both external and internal calibration signals, as well as with signals from test beams and laboratory sources. The AMPLEX chips were individually tested with a custom–built semi–automatic probe station, and sorted according to gain. The chips used on each ceramic were selected to have equal gain, and a trimming resistor was used to equalize the gains of the ceramics giving an overall channel-to-channel uniformity of approximately 1%. This degree of uniformity not only ensures optimum resolution for the trigger threshold, but eliminates the need for a database of calibration constants for off–line energy reconstruction.

The gain variations among the 16 channels of each AMPLEX, which can degrade the uniformity of the radial position measurements, were appreciably smaller. Using the internal calibration system, the mean RMS gain variations within each AMPLEX were measured to be 0.25%. Real gain variations were likely to be smaller, since the observed width could have been significantly broadened by variations in the calibration system rather than in the AMPLEX gains themselves.

The AMPLEX gain and the cross talk among channels were found to depend on the input capacitance of each channel and of the hold signal timing. Trimming capacitors, integrated into the ceramic hybrid structure, were used to equalize the total input capacitance which otherwise would have varied by a factor of two from the inner to outer edge of the detector. We have optimized the hold timing to provide a uniform response to injected charge and to minimize cross talk. An empirical correction was made to the data to account for the residual -2% cross talk of each channel to each of the other 15 channels on the same AMPLEX. This correction allowed us to accurately reconstruct showers and to recognize close-lying secondary showers which would have otherwise been masked by the cross talk from the primary shower. The effect of this cross talk on the energy measurement is discussed in section 4.3. The sensitivity of the cross talk to the hold timing of the AMPLEX chip is further discussed below in section 2.7.

To minimize the effects of residual gain and cross talk variations that may be systematic functions of the AMPLEX channel number, the AMPLEX channel ordering was inverted between the two radial pad columns of each ceramic.

The reliability of the entire readout system has been excellent: of the 608 installed detectors, only three are not currently functional. For all of the LEP I running, the number of non-functional detectors varied between one and three, none of them within three radiation lengths of the shower maximum at layer $7X_0$. The signals from such detectors are ignored in event reconstruction, and the missing energy interpolated from the depositions observed in adjacent layers. At the achieved level of reliability, such non-functional detectors cause no measurable degradation in performance.

2.6 Trigger electronics

The AMPLEX chip also includes a trigger output. When used in trigger mode, the average of all 16 channels appears as a single output. In the OPAL implementation, the signals from the four AMPLEX chips which service each wafer are further summed to provide a single analog trigger signal for each silicon wafer. Details of the OPAL design are given in reference [?].

In trigger mode, the summed signals are further combined by the trigger hardware, to provide whole calorimeter and wafer-tower sums. The tower signals allow the implementation of triggers which require back-to-back showers in azimuth. Additional details for the trigger algorithm are given in section 6.

On each LEP beam crossing, even if not triggered for event readout, all of the signals used by the trigger are digitized and stored. This trigger information is used for detailed monitoring of the trigger (see section 6). In addition, the trigger information is used to determine independently the energy and azimuth of showers in the detector. This capability is exploited in background measurements (section 5) and to check for failures in the event readout and reconstruction (section 3).

2.7 Bunchlet triggering

In normal operation LEP collides single bunches of electrons and positrons at uniform intervals no shorter than $11\,\mu$s, but in 1995 LEP operated in bunch-train mode, in which each normal bunch was replaced by a train of up to four bunchlets separated by only a few hundred nanoseconds [**?**]. For the entire 1995 scan, LEP operated with 3 bunchlets per train with an inter-bunchlet spacing of 247 ns.

Bunch-trains presented difficulties for the SiW detector, since the shaping time of the AMPLEX is comparable to the 1995 inter-bunchlet spacing. The AMPLEX operates in "continuous time filtering mode", which means that the ionization charge injected by charged particles passing through the silicon produces a shaped signal which peaks in about 270 ns, then decays away somewhat more slowly. Readout of the detector requires that the hold signal be asserted at a known time near the peak of the shaped signal, so that the instantaneous analog signals are captured on storage capacitors. In single-bunchlet LEP running the hold can be issued at the proper time on each bunch crossing, but with bunch-trains, it can only be issued at the proper time with respect to a single bunchlet in each train.

If we were to issue the hold synchronous with the last bunchlet, we would measure only about half the energy of showers originating in the previous bunchlet, and only about 15% of the energy of showers originating in the bunchlet preceding that. Furthermore, the inter-channel cross talk of the AMPLEX depends on the hold timing. Even if we had been able to ensure adequate triggering on the degraded signals from the earlier bunchlets, it was not evident that our sophisticated clustering and coordinate reconstruction algorithms could have been modified to measure such stale showers precisely.

Another possible strategy might have been to issue our hold in time with one of the bunchlets chosen at random on each bunch crossing. Apart from the undesirable loss in statistics this would have entailed, it was not evident that the large number of stale signals from previous bunchlet events could have been distinguished from the low-energy tail of in-time radiative Bhabhas with sufficient precision.

We therefore decided to upgrade the luminometer with a "wagon tagger" to issue hold in response to bunchlets actually depositing energy in the calorimeters. The wagon tagger is based on fast analog sums of the signals induced by electromagnetic showers on the back-plane of the silicon wafers. These sums are locally discriminated and processed to provide a bunchlet synchronization signal. The design of the wagon tagger was aided by the analysis of test-beam data. These data allowed us to ensure adequate sensitivity for both early and late developing showers, with a minimum number of instrumented layers. We included 6 layers (at 3, 7, 11 and 4, 8, 12 X_0) in the wagon tagger sums.

To achieve a low rate of false (or premature) tags, due to off-momentum electrons in bunchlets prior to the event of interest, while retaining sufficiently low thresholds to ensure full tagging efficiency, the wagon tagger was operated in "AND" mode, which required coincident tags in the left and right calorimeters, in all but four runs during the 1995 scan. In the absence of tags on earlier bunchlets the synchronization signal was always issued for the last bunchlet in the train. This allowed the efficiency of the wagon tagger to be precisely measured on the last bunchlet, as discussed in section 6.

3 Event reconstruction

The detailed information available from the 38,912 individual pads of the luminometers allows events to be reconstructed in a way which is well matched to the strengths and weaknesses in the theoretical treatment of the Bhabha scattering process. The theoretical summation over increasing orders in perturbation theory naturally delivers a more precise description of the higher-energy partons, and becomes more approximate as their energy decreases. The description of the angular distribution of radiated photons about the primary axes of the event also becomes less precise as the event topology becomes more complicated. Both these features are mirrored in the natural characteristics of the SiW luminometer.

The lateral profile of electromagnetic showers in the dense medium of the SiW calorimeters is characterized by a sharp central peak and broad tails, as shown in figure 6. The sharpness of the shower cores and the fine granularity of the detector allow us to reconstruct individual positions for incident electrons and photons which are separated by about 1 cm, while the inclusive nature of the calorimetric measurement of the energy in the shower tails forms a natural summation over accompanying low-energy photons, in a manner largely independent of their angular distributions. We exploit the fine granularity of the detector and conservation of transverse momentum to exclude background clusters generated by accidental off-momentum electrons from the energy sum.

The final luminosity measurement is not very sensitive to the parameters used to distinguish individual shower cores and to those used to determine which shower clusters belong to the Bhabha event.

In this section we describe some details of the cluster formation and describe how kinematic information is used to select the clusters which belong to an event. The first step of cluster finding is the peak-finding algorithm which is used to find shower cores. Near the longitudinal shower maximum, these shower cores are typically sharply peaked transversely with a FWHM of less than a single radial pad width (0.25 cm). However, the tail of the energy distribution extends laterally to almost 10 pad widths (2.5 cm) as can be seen in figure 6. This diffuse energy is associated with shower cores to form “clusters”. The detector simulation described in section 8 has been tuned using actual data to reproduce the measured properties of this clustering algorithm.

After all resolvable clusters have been assigned radial and azimuthal coordinates, and their measured energies have been corrected for showering losses in the dead material in front of the detector, as described in section 4, the clusters belonging to a candidate Bhabha are selected by a kinematic selection algorithm, described in section 3.2. This algorithm differentiates between showers from radiative Bhabha processes and those due to background from the LEP machine by exploiting the transverse momentum balance intrinsic in the set of clusters belonging to a true Bhabha event. When the candidate Bhabha clusters are identified, the most energetic cluster found on each side of the detector is used to define the event coordinates, while the energy sum of all selected clusters on each side is used in making the cuts on the minimum and average energies required for fiducial Bhabha selection. By cutting on the total energy, rather than the energy of the most energetic cluster, the sensitivity of the luminosity measurement to treatment of final state radiation in the BHLUMI Monte Carlo and in the detector simulation is greatly reduced.

3.1 Peak finding and cluster building

Although the full three-dimensional information (r, ϕ, z) of each pad in the event is available, for the purpose of identifying cores of electromagnetic showers, a generalized search in three dimensions is not needed. Instead, the nearly projective geometry of the detector is exploited to reduce the three-dimensional pattern recognition problem to a two-dimensional one.

The peak finding algorithm first finds the energy deposited in pads in the three even and three odd layers nearest the estimated mean longitudinal depth of each individual shower. The energies in these two sets of pads are then projected separately onto the $r-\phi$ plane. The peak finder then searches for coincident peaks in the $r-\phi$ projection of the two sets of pads. Peaks are identified by a threshold on the second spatial derivative of pad charge, so that a sufficiently pronounced shoulder can be identified as a secondary peak close to the primary. The multiplicity spectrum of such identified peaks falls exponentially with a factor of about 0.015 per additional peak. Up to three peaks in a given calorimeter are selected and pads in a geometric region around each peak are associated to form clusters. The collection of pads associated with each cluster are then used to determine the radial and azimuthal coordinates, as described in section 4.

In order to retain strangely shaped showers, a second cluster algorithm is used to find any remaining energy deposition. This “blob” finder projects all of the unused energy in the detector to the $r-\phi$ plane and looks for any simply connected two-dimensional region of energy deposition. Such blobs with more than 1 GeV of measured energy are subsequently treated in all respects as normal “peak”

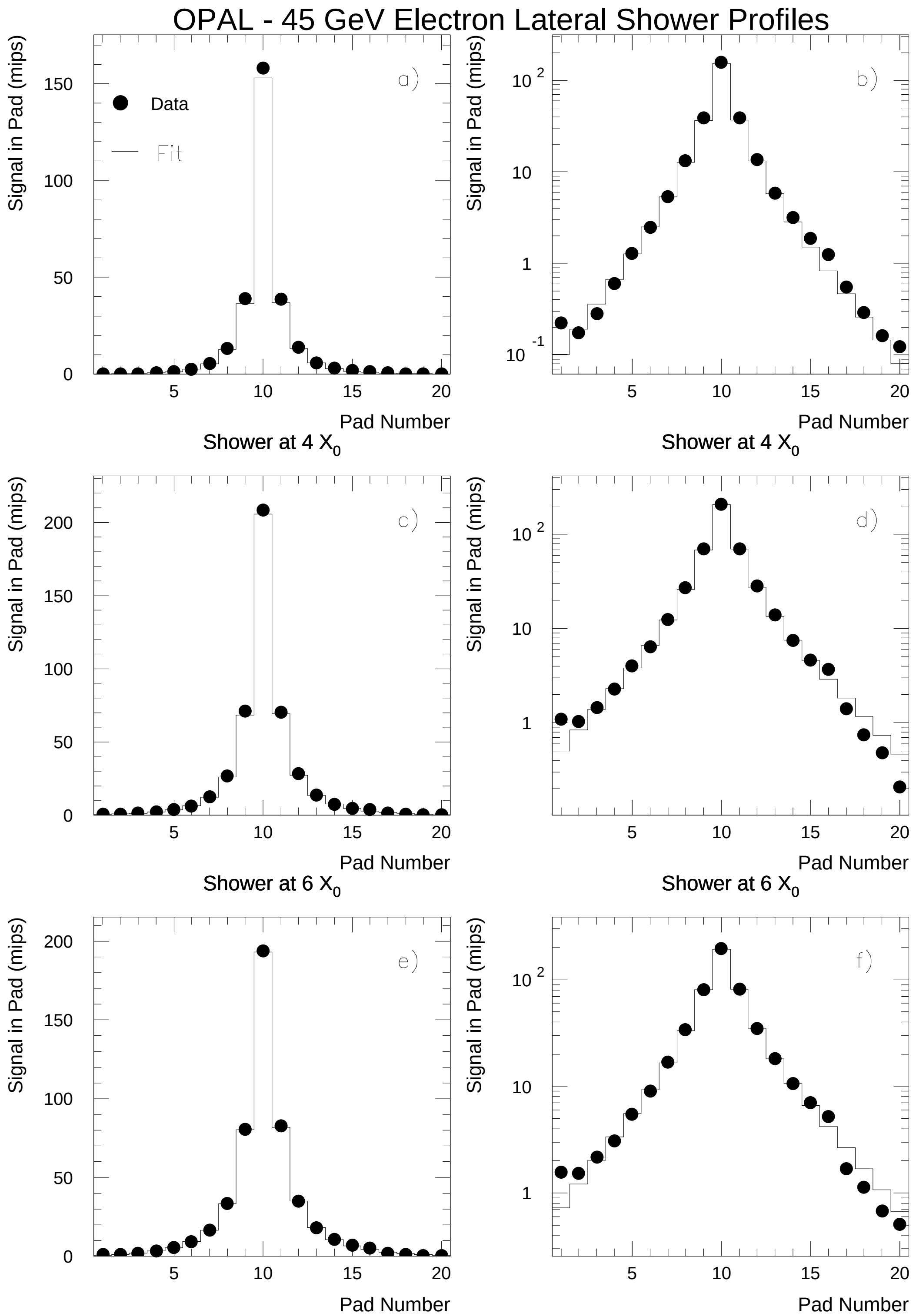

Figure 6: Average radial shower profiles at 4 X_0 a) and b), 6 X_0 c) and d), and 8 X_0 (e) and (f). The fit shows the parameterization of the electromagnetic showers given in reference [?]. The left plots show the data on a linear scale, the right plots on a logarithmic scale.

clusters. The azimuthal and radial coordinates of blobs are determined from the location of the energy maximum in the $r - \phi$ plane.

The probability that a true shower is classified as a blob is small. By looking for events (with somewhat looser selection requirements than those given in section 1.3) which have a normal cluster on one side and only a blob on the other, the rate of blobs is estimated to be less than 1 in 10^4 [?]. This small number shows that the main cluster finding succeeds in correctly identifying almost all showers from Bhabha events.

We have also used the trigger system to check the cluster finding efficiency. This is accomplished by requiring that one side has a cluster with $E > 0.85 \cdot E_{\mathrm{beam}}$ and a radial coordinate which satisfies the definition cuts of section 1.3. In addition, a back-to-back trigger (SWSEG, see section 6) is required and the digitized trigger energy on each side is required to exceed $0.5 \cdot E_{\mathrm{beam}}$. We would expect that in all such events reconstructed clusters would be found on both sides of the detector. In the 1993 and 1994 data, only one event without reconstructed clusters on both sides is observed. In the 1995 data, 11 such events are observed in a sample of 1.7×10^6 events. On the basis of these 11 events, a systematic error of 0.1×10^{-4} is assigned to the cluster finding process.

The ability of the cluster finder to resolve two electromagnetic showers has been studied by using events with a secondary cluster from final state radiation. The two cluster separation efficiency is measured by overlaying the pad energies from the raw data of the radiative cluster at a variable position near the most energetic cluster. This is accomplished by using events with a widely separated radiative cluster and then rotating the pad signals of one of the clusters in azimuth so that they overlap with the pad signals of the other cluster. As the radial distance between the two clusters varies, the efficiency for the cluster finder to find both clusters is measured. It is found that for clusters above 5 GeV, the cluster finding efficiency is 50% at a separation of approximately 1.0 cm, corresponding to 4 pad widths, as shown in figure 7. The measured values of the two cluster separation efficiency have been incorporated into the detector simulation described in section 8.

Figure 8 illustrates how the reconstructed coordinate of the primary cluster is disturbed by about 100 μm when the secondary cluster is resolved, and up to 1.5 mm when the cluster is fused. There is no evidence of a net radial bias.

Although we have expended considerable effort to optimize the cluster separation capabilities of the detector, the acceptance of the Bhabha selection is in fact insensitive to the details of cluster formation. For example, changing the cluster finding parameters so that a large fraction ($\sim 20\%$) of true showers are split into two clusters reduces the acceptance by only 10^{-4}.

3.2 Kinematic cluster selection

The kinematic cluster selection algorithm discriminates between radiative clusters belonging to the Bhabha event and off-momentum machine background by exploiting the conservation of transverse momentum in complete Bhabha events. The algorithm first calculates the momentum vectors associated with the clusters assuming they originate from the measured beam spot. The algorithm then evaluates each pairing of all possible cluster combinations in each calorimeter to find the pair of combinations which minimizes the total normalized transverse momentum imbalance. By minimizing transverse momentum normalized to the energy of the combination, a possible bias towards selecting low energy combinations is eliminated. The probability that the kinematic selection algorithm finds a secondary cluster belonging to a Bhabha event is about 1.3% per calorimeter. About 76% of these secondary clusters exceed 10% of the beam energy and satisfy generous requirements for clear separation by lying either more than 400 mrad in azimuth or more than 2 cm in radius from the primary cluster. The energy spectrum of such secondary clusters is shown in figure 33 in section 10. As explained above, when such radiative clusters are found, their energy contributes to the fiducial energy of the event, but they are ignored for the measurement of the radial and azimuthal coordinates.

The kinematic cluster selection algorithm has been compared with other, simpler, algorithms and no significant differences in acceptance have been observed. The acceptance of the Bhabha selection is also quite insensitive to the level of background clusters in the events, as discussed in section 5.

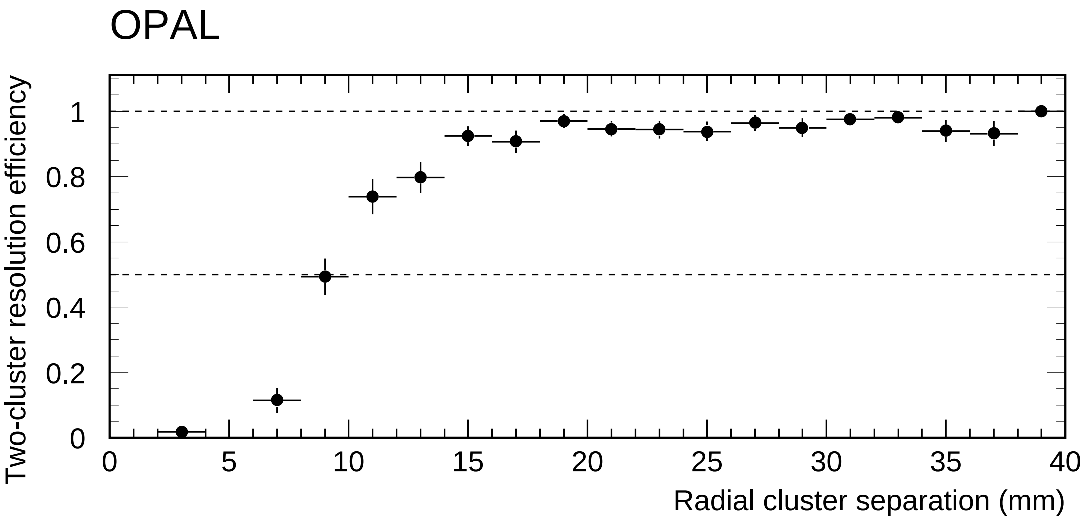

Figure 7: The measured probability of reconstructing the second cluster in a radiative Bhabha event, where the second cluster energy lies between 5 and 10 GeV and it shares the same azimuth as the primary cluster, plotted as a function of the radial separation between the two clusters.

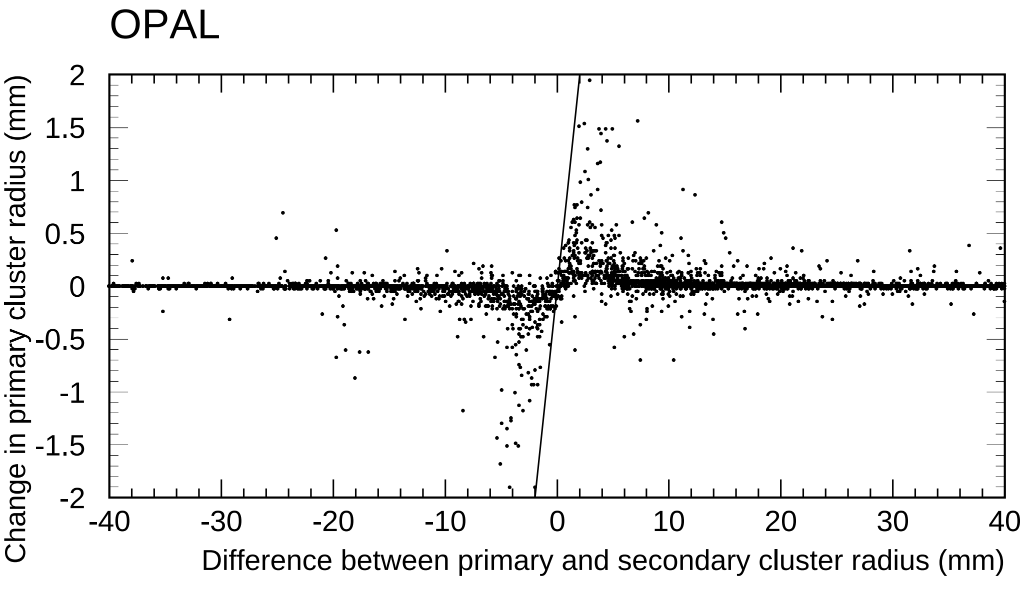

Figure 8: The displacement of the radial coordinate of the highest energy reconstructed cluster in the "overlayed" radiative event sample, as a function of the radial separation between the primary and secondary clusters. Here the secondary cluster is selected to have an energy above 2 GeV. The diagonal line shows the expected displacement if the secondary cluster were simply mistaken for the primary.

4 Measurement of shower position and energy

4.1 Radial reconstruction

The $1/\theta^3$ spectrum of the Bhabha scattering process causes the luminosity measurement to be particularly sensitive to bias in the cuts defining the angular acceptance. Not only must the absolute physical dimensions of the detector itself be carefully determined (as described in sections 2.3 and 2.4), but also the relationship between the reconstructed shower positions and the physical detector elements must be established. Since this represents perhaps the most critical aspect of the luminosity measurement, we describe, in some detail, how we reconstruct the position of showers from the pad signals, and especially how we determine the relation of these reconstructed coordinates to the actual trajectories of incident electrons in real space. First, however, we describe quantitatively the sensitivity of the angular cuts.

The acceptance of the luminosity measurement will be affected by any change, ΔR, in the inner and outer edges of the acceptance as follows:

$$\frac{\Delta A}{A} \approx -\frac{\Delta R_{\mathrm{in}}}{25\ \mu\mathrm{m}} \times 10^{-3} \tag{11}$$

and

$$\frac{\Delta A}{A} \approx +\frac{\Delta R_{\mathrm{out}}}{110\ \mu\mathrm{m}} \times 10^{-3}. \tag{12}$$

Similarly, the acceptance will be affected by any change, ΔZ, in the half-distance between the effective planes of the radial measurements in the two calorimeters:

$$\frac{\Delta A}{A} \approx +\frac{\Delta Z}{1.23\ \mathrm{mm}} \times 10^{-3}. \tag{13}$$

The coefficients in the expressions given above can be reproduced by simple analytic calculations, using only the $1/\theta^3$ Bhabha spectrum, the nominal half distance between the reference planes of the two detectors (2460.225 mm), and the inner and outer acceptance radii (77 and 127 mm).

Second order effects due to finite resolution also occur whenever a cut is imposed on a quantity with a steeply falling distribution. An acceptance change is introduced due to the fact that more events actually on the uphill side of the cut will be measured to fall on the downhill side than vice–versa. This *resolution flow* can be expressed as

$$\frac{\Delta A}{A} = \frac{\mathrm{d}f}{\mathrm{d}x}\frac{\sigma_x^2}{2} \tag{14}$$

where $f(x)$ is the intensity of events normalized to unity over the entire acceptance, and σ_x is the resolution in the variable x upon which the cut is imposed. Evaluating this expression for the R^{-3} Bhabha distribution within our acceptance, we find

$$\frac{\Delta A}{A} \approx +\left(\frac{\sigma_{\mathrm{Rin}}}{1.12\ \mathrm{mm}}\right)^2 \times 10^{-3} \tag{15}$$

and

$$\frac{\Delta A}{A} \approx -\left(\frac{\sigma_{\mathrm{Rout}}}{3.04\ \mathrm{mm}}\right)^2 \times 10^{-3} \tag{16}$$

for radial resolutions of σ_{Rin} and σ_{Rout} at the inner and outer acceptance boundaries.

Similarly, a cut is imposed on ΔR, the difference of R_{R} and R_{L}, in the tails of the acollinearity distribution (see figure 32, section 10) where the density of events is low, but is falling steeply. This results in a resolution flow of

$$\frac{\Delta A}{A} \approx -\left(\frac{\sigma_{\Delta R}}{3.54\ \mathrm{mm}}\right)^2 \times 10^{-3}. \tag{17}$$

Any net bias, ΔR_{bias}, in the measured acollinearity also causes a first–order change in the acceptance of

$$\frac{\Delta A}{A} \approx \frac{\Delta R_{\mathrm{bias}}}{416\,\mu\mathrm{m}} \times 10^{-3} \tag{18}$$

due to the density of events near the acollinearity cut (see again figure 32, section 10). These acceptance changes, on the order of a few times 10^{-5} are discussed in section 8.

The finite angular divergence of the LEP beams is in many respects equivalent to a further smearing of the detector resolution, and also creates a very small change in acceptance. This is discussed in section 7.

One of the advantages of our highly-segmented calorimetric measurement over a tracking measurement is the fact that valid coordinates can be assigned to all clusters observed within the fiducial volume of the detector with an inefficiency less than 10^{-5}. A typical 45 GeV electron shower deposits energy in $\sim$ 500 pads in the calorimeter. From this large amount of information, it is possible to reconstruct the radial position of the shower with a resolution of 130 to 170 μm and a systematic bias everywhere less than 15 μm. At a large number of pad boundaries, distributed throughout the volume of the detector, we can do even better, and demonstrate that our total bias near these boundaries, including metrology errors, is less than 6.5 μm.

The shower-by-shower radial reconstruction begins with finding a radial coordinate in each layer of the calorimeter (section 4.1.1). The better layer measurements are then selected, projected onto the reference layer at 7 X_0, and averaged (section 4.1.2). The average raw coordinate is finally smoothed to compensate for non-uniformities in the resolution across the pad structure of the detector (section 4.1.3). This smoothed coordinate is then used in making the primary cut defining the luminometer acceptance. We then proceed to quantify the residual bias in the smoothed coordinate and calculate a corresponding correction to our acceptance. This procedure relies on a concept which we term the *pad boundary image*, which can be defined as the coordinate at which an incident electron deposits, on average, equal energies on two adjacent pads. The bias of the coordinate with respect to a large number of such individual pad boundary images can be evaluated by a process we term “anchoring”. The absolute offset of the pad boundary images themselves with respect to the physical geometry of the detector is determined on the basis of test beam measurements in which a fully instrumented SiW segment was exposed to a beam of electrons and muons. Since the SiW pads are sensitive to muons, the muon tracks were used to determine the geometry of the calorimeter pads with respect to a beam telescope. Measurements of the showering electrons were then used to determine the small asymmetry in the energy deposited in a pair of adjacent pads (which differ slightly in area due to the $R-\phi$ geometry of the detector) when the electron trajectory lies exactly on the boundary between the pads. The evaluation of this bias is discussed in section 4.1.4. We now address the question of determining a radial shower coordinate from the pad signals in the individual layers of the detector.

4.1.1 Radial coordinate in each layer

The radial coordinate reconstruction in SiW is based on the good approximation that pad boundaries and pad centers are symmetry points of the detector. In each layer, using the triplet of pads centered around the pad with the maximum energy deposition, we construct the function:

$$D \equiv \frac{E_1 - E_3}{2 \cdot E_2 - E_1 - E_3} \tag{19}$$

where E_2 is the energy in the central pad of the triplet and E_1 and E_3 are the energies in the adjacent pads. To within the approximation given above, the function D so defined takes on the value of 0 for a shower hitting the center of the triplet of pads (in which case $E_1 = E_3$), and ± 1 for showers hitting the outer or inner boundaries of the central pad (in which case $E_1 = E_2$ or $E_3 = E_2$).

These symmetry properties of the function D would be perfect in a detector with Cartesian pad geometry. The extent to which this symmetry is altered by the $r-\phi$ configuration of the pads depends on the scale of the lateral shower spread in the calorimeter compared to the radius of curvature of the pads, as well as the pad size. The resulting bias is smaller at pad boundaries than it is at the pad center. In section 4.1.4, we discuss how we quantify the pad boundary bias using test beam measurements. This bias is, however, ignored in the process of shower coordinate reconstruction, which preserves these symmetries explicitly.

In the region between pad boundaries and pad centers, the variable D is not a linear function of the true position of the incoming electron, deviating from linearity by up to 20% of the pad width, or 500μm. This nonlinearity can be conveniently parameterized using the easily invertible functional form

$$|R_{\rm p}| = \frac{w_p}{2}\left[D_1 - \left(\frac{A}{|D| + D_0}\right)^{\frac{1}{\beta}}\right] \tag{20}$$

where $R_{\rm p} \in [-\frac{w_p}{2}, +\frac{w_p}{2}]$ is the linearized coordinate relative to the pad center, $w_p = 0.25$ cm is the pad width, the quantity β controls the nonlinearity of the transformation, and $D_1 = 1.1$ is a constant. The values of D_0 and A are set by transferring the symmetry conditions of D to $R_{\rm p}$ during the optimization of β. In particular, although not formally obvious, $R_{\rm p}$ is constrained to be a function with odd symmetry about the pad center. At a depth of $6{\rm X}_0$, the parameters take on the values: $\beta = 0.544, D_0 = 0.372, A = 0.392$.

Figure 9 shows $R_{\rm p}$ as a function of D as parametrized according to equation 20 for shower widths characteristic of calorimeter layers near the depth of maximum longitudinal shower development, which are more critical in measuring the radial coordinate. The extent of the evident nonlinearity depends sensitively ($\pm100\mu$m) on the scale of the lateral shower spread in the calorimeter compared to the size of the pads. We have optimized β as a function of the locally observed individual shower width while explictly preserving the desired symmetries of the reconstruction function about the pad edges and centers, using data taken both during normal running at LEP and in the test beam. The result is a unique expression for $R_{\rm p}$ in terms of the charges observed in the pad triplet. Due to its explicit dependence on the apparent shower width, the same functional form is valid, independent of layer.

The resolution of the radial coordinate in a single layer varies strongly across the pad. Near longitudinal shower maximum, it is about 300 μm at the pad boundary, and 750 μm at the pad center. This rapid variation in resolution makes a precise definition of the residual bias in $R_{\rm p}$ rather subtle, since events falling in regions of poor resolution are more likely to be measured as falling in regions of good resolution than vice versa. We refer to $R_{\rm p}$ as being "linearized", in that it has a much more linear relation to the true coordinate than the pad triplet quantity, D. Precisely speaking, it is linearized in that the parameters of equation 20 have been chosen to minimize what might best be termed the integral bias throughout the pad

$$\text{Bias}_{\text{int}}(R_{\rm p}) = w_p\frac{N(R_{\rm p})}{N_{\text{tot}}} - (R_{\rm p} + \frac{w_p}{2}) \tag{21}$$

where $N(R_{\rm p})$ is the number of events falling within the pad, but below $R_{\rm p}$, in a clean sample of Bhahba events, and N_{tot} is the total number of events within the pad. Note that we ignore in this optimization the expected $1/R^3$ fall-off in the Bhabha intensity and attempt to approach a flat distribution of events over the pad. The odd symmetry of the linearization function 20 about the pad center, obvious from figure 9, ensures that no events cross from one half of the pad to the other, and prevents this simplification from introducing a significant bias in the optimization.

Systematic errors in the layer coordinates derived from individual pad triplets can be induced by channel-to-channel variation in the AMPLEX front-end chip gains. All crucial coordinate measurements come from pad triplets which do not span AMPLEX boundaries. For such triplets the gain variations have been measured to be $\leq 0.25\%$, with a precision limited by the uniformity of the calibration system (see section 2.5). The corresponding systematic fluctuations in $R_{\rm p}$ can be calculated from the slope of figure 9, which varies strongly across the pad. At the pad boundary a 0.25% gain fluctuation corresponds to

$$\Delta R_{\rm p} = 2.5\,\mu\text{m}. \tag{22}$$

While at the pad center the same gain variation corresponds to $\sim 25\,\mu$m.

The effect of such systematics will be reduced by the fact that many independent sets of pad triplets contribute to the measurement, as will be seen in the following sections.

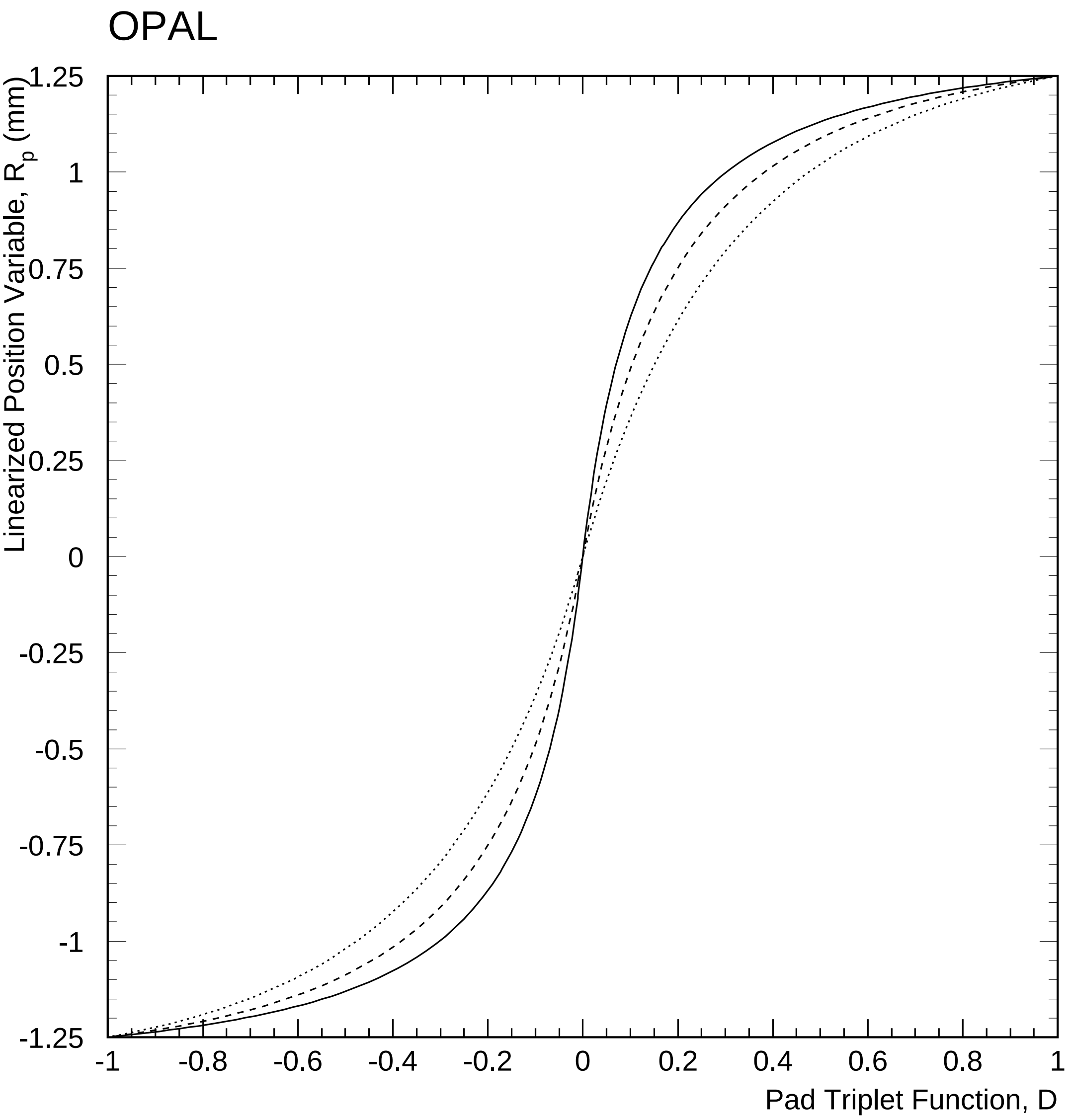

Figure 9: The linearized position variable, R_p, in millimeters as a function of D, in units of half pad widths. This is shown for characteristic shower depths of 4 (solid line), 6 (dashed line) and 8 X_0 (dotted line). The center of the pad is at 0, and the boundaries at ±1.25 mm.

4.1.2 Average radial coordinate

As the next step in reconstructing a radial coordinate, we project the positions measured in each layer using the variable R_p onto the reference plane at 7 X_0 assuming the nominal beam spot position. The average, R_a, is then determined from the projected coordinates. The layers used in the average are selected from the 9 layers at depths[4] between 2 and 10 X_0. Only layers with "good coordinates", are used but are not otherwise weighted in the average. "Good coordinates" are defined as coming from pad triplets with

- sensible observed shower width (characteristic of shower depths from 1 to 13X_0)
- an energy sum exceeding a minimal threshold ($E_\mathrm{triplet} > 200$ MeV)

---

[4] The range of 9 layers used is shifted by up to ± 2 layers in the case of exceptionally early or late shower development.

- a useful estimated resolution ($\sigma_\mathrm{r} < 2.5$ mm)

The mean number of layers used in the average is 6.2 with an RMS of 1.5 for a 45 GeV shower within the fiducial acceptance of the detector. The mean layer used in the average is 6.4 with an RMS of 0.7 on the right, and 6.1 with an RMS of 0.7 on the left. The fact that the center of measurement is close to the reference plane limits the error introduced by any difference between the actual beam spot and the ideal beam geometry assumed in the projection. Even for maximal beam spot offsets and highly abnormal longitudinal shower developments, the projection error is everywhere less than 10 μm, and cancels to a fraction of a micron in the average over either azimuth or shower development depth.

The process of averaging the layer coordinates also has the advantage of reducing the possible systematic error due to pad gain variations. Most significantly, any channel-to-channel gain variations which are common to all AMPLEXes will be largely cancelled by the fact that the radial direction of the AMPLEX channel ordering has been inverted between the right and left pad columns of each detector hybrid. This fact, in combination with the azimuthal staggering of each detector layer means that the AMPLEX channel ordering alternates from radially inwards to radially outwards for the pad triplets in each layer along the trajectory of every measured shower.

Also, in averaging over the 6.2 layers which typically contribute to the average coordinate for each shower, the effect of random channel-to-channel gain variations will be sampled over most of a pad width and be statistically damped, yielding a maximum systematic error in each tower of

$$\Delta R^{\mathrm{a}}_{\mathrm{gains}} = \frac{1}{2}(25\,\mu\mathrm{m} + 2.5\,\mu\mathrm{m})/\sqrt{6.2} = 5.5\,\mu\mathrm{m} \tag{23}$$

These random systematic errors will also be different in each of the 32 azimuthal towers in each calorimeter, yielding an expected error of only $5.5\,\mu\mathrm{m}/\sqrt{32} = 1.0\,\mu\mathrm{m}$ when averaged over ϕ.

A typical R_a distribution is shown in figure 10. For this plot, the normal isolation cuts are imposed, except for those involving the radial coordinate in either calorimeter. This radial coordinate is no longer integral bias free, as evidenced by the structure visible in the plot, which corresponds to a residual nonlinear bias of up to 50μm with a periodicity of 2.5 mm, given by the radial pad pitch. In averaging R_p over many layers, we have improved its resolution, but destroyed the original balance of resolution flow[5] and inherent bias enjoyed by R_p in each layer.

The symmetry of the coordinate about the pad boundary has also been influenced to some extent by the averaging over layers, but we can expect it to be best preserved at layer 7, the reference layer, and center of measurement. The fact that the pads possess a cylindrical, rather than projective geometry, not only dilutes systematic effects, but even allows the remaining systematic effects to be measured. Near the inner edge of the acceptance, the projected coordinate lies on the pad boundary of one layer or another with a periodicity of about 200 μm in R. This fact will be exploited extensively in section 4.1.4. We now turn our attention to the problem of re-establishing a condition of minimum integral bias in the layer-averaged coordinate.

4.1.3 Smoothing the radial coordinate

If the bias, B, in the raw average coordinate, R_a, were known, then it could be removed by direct subtraction, that is,

$$R_{\mathrm{true}} = R_a - B(R_a). \tag{24}$$

Although test beam measurements are able to give us some direct knowledge of B, the interplay between the coordinates from each layer depends strongly enough on the beam geometry and the material in front of the detector that it was not optimal to directly apply the bias measured in the test beam.

We were able to arrive at a better estimate of B under LEP conditions empirically, by studying the structure in the observed R_a distribution, and extracting a smoothing offset, $S \approx -B$, such that

---

[5] Finite resolution, coupled with a sloping spectrum, causes events to flow across a boundary. See equation 14.

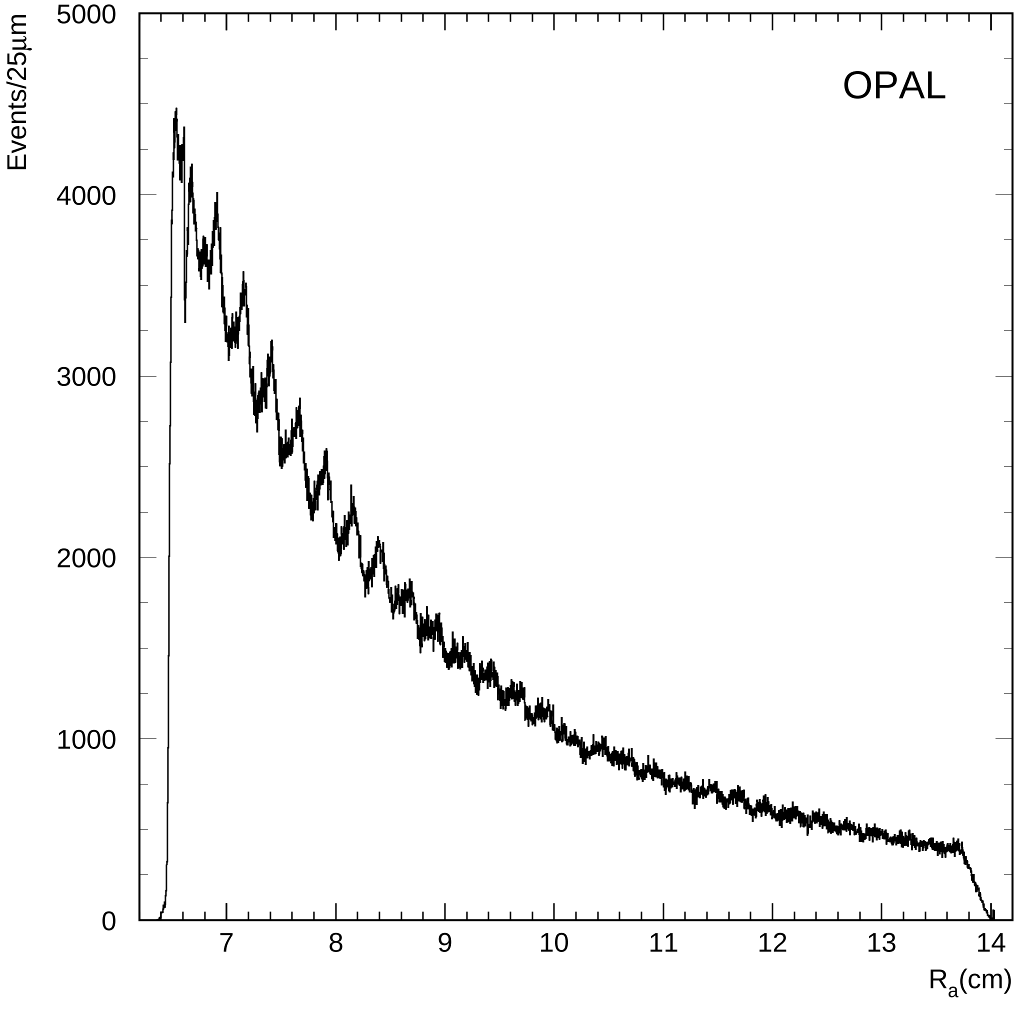

Figure 10: The distribution (upper plot) of R_{a}, the raw radial coordinate, averaged over layers, for the largest of the 9 luminosity analysis data sets (94b). Also shown (lower plot) is the bin-by-bin smoothing offsets, $S(R_a)$, determined by the smoothing condition. The quasiperiodic structure at the 2.5 mm period determined by the pad width has a maximum amplitude of $\approx 50\mu$m. The Bhabha isolation cuts have been applied, except for those involving the radial coordinate in either calorimeter.

$$R_{\text{smooth}} = R_a + S(R_a). \tag{25}$$

The distribution of R_{smooth} is required to have minimal structure at the 2.5 mm pad periodicity of the detector. The lack of structure in R_{smooth} is a requirement for the luminometer acceptance to be independent of the position of the radial acceptance cuts with respect to the pad boundaries. This condition, although highly desirable for the SWITR and SWITL selections, is truly essential for the SWITA selection, since the offset of the beam spot with respect to the symmetry axis of the calorimeters means that right and left shower coordinates individually lying well away from the fiducial pad boundaries in each calorimeter will comprise the acceptance boundary defined in terms of $R_A = \frac{1}{2}(R_R + R_L)$.

Apart from requiring that the distribution of R_{smooth} be smooth, we also, and more importantly, require the strict condition that the smoothing offsets cause no event to cross any pad boundary in the reference layer at $7X_0$. This condition is assured when $S(R_a) = 0$ at the pad boundaries.

We begin by parameterizing the R_{smooth} distribution as follows:

$$\frac{dN}{dR_{\text{smooth}}} = a_i R_{\text{smooth}}^{-3} - \frac{s_i}{w_{\text{bin}}} \cos(\alpha/2) - \frac{d_i}{w_{\text{bin}}} \cos(\alpha) \tag{26}$$

$$\alpha = 2\pi \frac{R_{\text{pad}}}{w_{\text{pad}}} + \pi \tag{27}$$

where $R_{\text{pad}} = R_a - R_i$, having the range $[-1.25, +1.25]$mm, is the radial coordinate with respect to R_i, the center of the pad (i) in which R_a lies, $w_{\text{pad}} = 2.5$mm is the pad width, and $w_{\text{bin}} = 25\mu$m is the radial histogram bin width. The power-law constants a_i, d_i, and s_i are determined as follows, where $i = [1, 32]$ runs over all the radial pad rows.

The constants a_i are fixed by the constraint that the smoothing should not alter the number of events in any pad, giving

$$a_i = \frac{2N_i}{(R_i - w_{\text{pad}}/2)^{-2} - (R_i + w_{\text{pad}}/2)^{-2}} \tag{28}$$

where N_i is the number of events in the sample to be smoothed which fall within pad i according to the raw radial coordinate, R_a.

Only if the radial distribution of events follows an R^{-3} dependence perfectly will the a_i terms determined above be continuous at the pad boundaries. The sinusoidal terms in equation 26 allow continuity to be restored while imposing minimal structure on the shape of the smoothed radial distribution. The discontinuities of the a_i terms at the pad boundaries are

$$b_i = a_i \cdot w_{\text{bin}} \cdot (R_i - w_{\text{pad}}/2)^{-3} - a_{i-1} \cdot w_{\text{bin}} \cdot (R_{i-1} + w_{\text{pad}}/2)^{-3}. \tag{29}$$

The sinusoidal terms in equation 26 have zero integral over each pad by construction, and therefore do not cause events to cross pad boundaries. Their coefficients d_i and s_i are determined by the condition that the right-hand side of equation 26 pass through the mid-points of the discontinuities, b_i, at each bin boundary.

The coefficients of the half-cycle sinusoids, s_i, can be called "slope modifier" terms, since they tend to move events in a single direction across the width of a pad. They compensate for any long-range deviation from the assumed R^{-3} dependence in the radial event distribution. Such a deviation would cause the b_i's to remain of like sign from pad to pad.

The coefficients of the full-cycle sinusoids, d_i, can be called "dust under the carpet" terms, since they tend to move events from both edges of the pad toward the center, or vice versa. They compensate for pads having locally either more or fewer events than could be extrapolated from their two nearest neighbors, leading to b_i's which change sign from pad to pad.

The d_i and s_i coefficients are determined very simply from the b_i's as follows:

$$d_i = +\frac{1}{4}\left(b_{i+1} - b_i\right) \tag{30}$$

$$s_i = -\frac{1}{4}\left(b_{i+1} + b_i\right) \tag{31}$$

Figure 11 shows the observed distribution of the raw radial coordinate, R_a, and the target function for dN/dR_{smooth} as determined by equation 26 in the region near the inner acceptance boundary. The departure of the R_a distribution from R^{-3} can be seen in the steps between the virtually straight power-law segments given by the a_i. In the inset, the final target function can be seen to pass smoothly through the mid-points of these discontinuities at the bin boundaries.

Having determined the desired shape of the radial event distribution in a way which ensures that no event will be allowed to cross a pad boundary at the reference layer in the detector, and which minimizes the structure in the radial distribution within the pad while guaranteeing continuity at the pad boundaries, we proceed to generate the smoothing offset of equation 25, which when added to R_a will produce the desired shape of the smoothed radial distribution.
The offset function $S(R_a)$ is determined by the condition

$$\int^{R} \frac{dN}{dR_a}\left(R_a + S(R_a)\right) dR_a = \int^{R} \frac{dN}{dR_{\text{smooth}}} dR_{\text{smooth}} \tag{32}$$

where dN/dR_{smooth} is given by the right-hand side of equation 26. The smoothing offsets as found bin-by-bin from the R_a distribution are shown in figure 10. The offsets exhibit a quasiperiodic variation following the pad pitch, with a maximum amplitude of 50μm and an rms of $\sim 20\mu$m. We then parameterize $S(R_a)$ with a Fourier decomposition which represents the lower portion of figure 10 everywhere within 1μm, giving

$$S_i(R_{\text{pad}}) = \sum_{j=1}^{7} c_{ij} \cdot \sin(j \cdot \alpha). \tag{33}$$

The restriction to sine terms only in the Fourier series guarantees that $S(R_a)$ is identically zero at the pad boundaries, and hence that the smoothing will not change the pad of any event. An independent smoothing transformation is made for each of the 9 separate luminosity analysis data samples in order to track any subtle influence of beam spot motion on the reconstructed radial coordinate. Noticeable differences between the data samples are observed, but none of great significance.

Figure 12 shows the distribution of the smoothed radial coordinates near the inner cut boundary for the same data sample as the raw radial distributions in figures 10 and 11. No structure is apparent beyond statistical fluctuations, and the measured luminosity is independent of the radius chosen to define the inner edge of the acceptance, as demonstrated in section 4.1.4. Since the smoothing is constrained to make no change in the measured coordinates at the pad boundaries, the primary luminosity acceptances, SwitR and SwitL, which are defined by radial cuts corresponding to the pad boundaries between pad rows 6 and 7, are insensitive to radical alterations, let alone any residual imperfections, in the smoothing.

It should be noted that the lack of integral bias provided by the smoothed radial coordinates on each side of the luminometer does not guarantee the lack of integral bias in the *average* radial coordinate, R_A, taken between the right and left calorimeters. The resolution of the average radius is improved by a factor of $\sqrt{2}$, and the balance between resolution flow and inherent bias is again disturbed. Test beam measurements provide a direct measurement of the variation of resolution of R_a (and hence R_{smooth}) across the pads. The resolution varies from 130μm near the pad boundary to 170μm near the pad center. We calculate that this level of variation induces $\sim 15\mu$m of inherent, but compensated, bias in the smoothed coordinate, so that the uncompensated integral bias in the smoothed coordinates averaged between the right and left sides, R_A, should be $\sim 10\mu$m.

Since the typical beam offset causes the radius of back-to-back showers to differ by up to a full pad width, no structure is visible, or would be visible, even if it were present, in the distribution of the

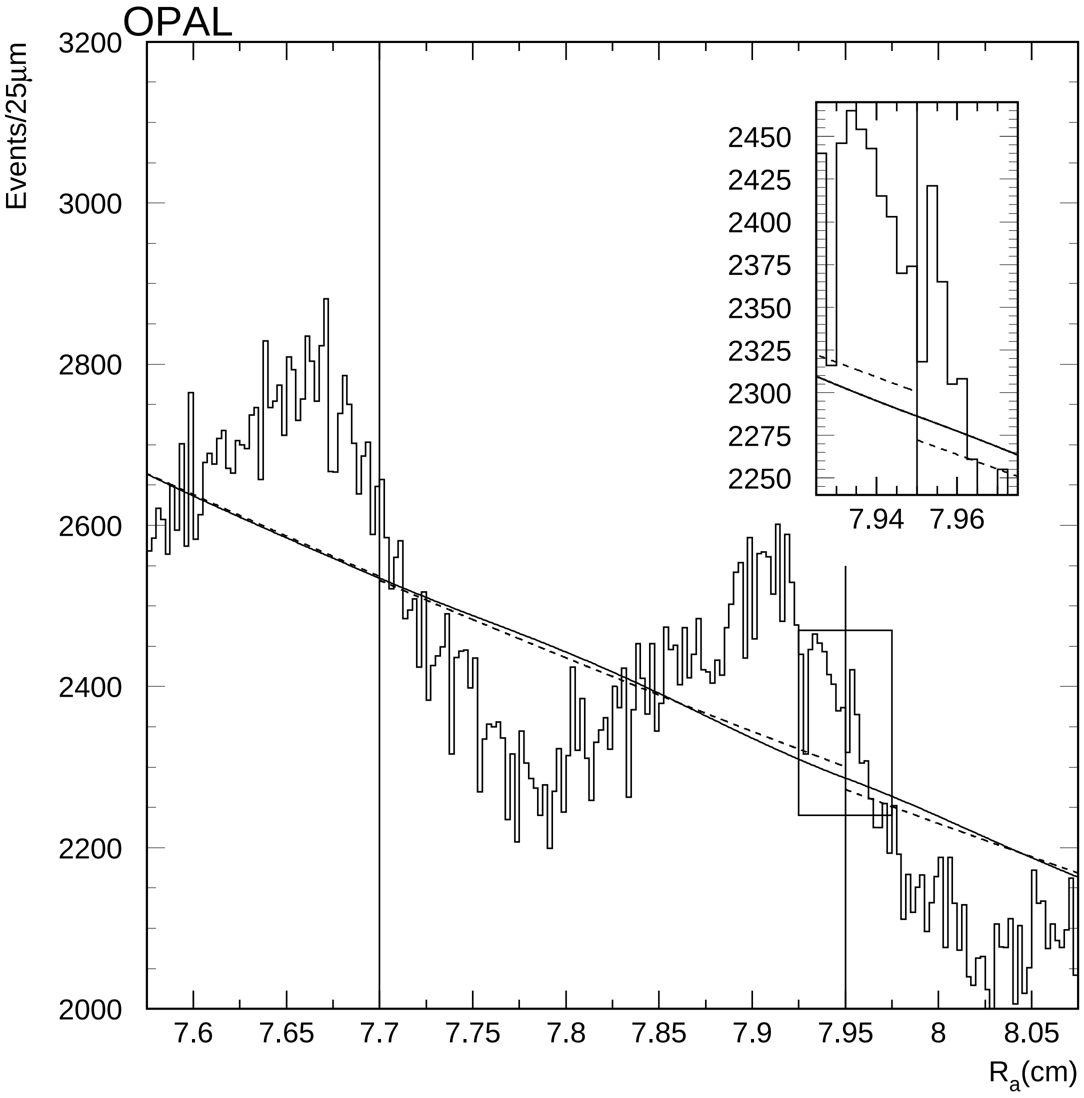

Figure 11: The observed distribution of the raw radial coordinate, R_a, and the target function for dN/dR_{smooth} in the region near the inner acceptance boundary. The vertical lines indicate the position of the pad boundaries in the reference layer of the calorimeter. The departure of the pad by pad R_a distribution from R^{-3} causes the steps between the virtually straight power-law segments (dashed lines) given by the a_i. The final target function is indicated by the solid curve. The inset shows how the final target function passes smoothly through the mid-points of the power-law discontinuities at the pad boundaries.

averaged coordinate, R_A. The mixture of inherent biases is sampled fully as a function of azimuth, and any initial structure will be washed out. In fact most of the residual integral bias will also be washed out in the average over azimuth. We estimate that approximately 5μm bias will remain in R_A at any particular radius in the clean region of acceptance ($R < 8.5$ cm), after integrating over ϕ. [6] The SwitA luminosity counter therefore suffers an inherent additional systematic error of 2×10^{-4} due to this bias uncertainty, and for this reason we use the average of the SwitR and SwitL counters

---

[6] Behind greater amounts of preshowering material, the quality of the measured coordinate is somewhat degraded, having consequences for the systematics of the acollinearity cut (see section 8).

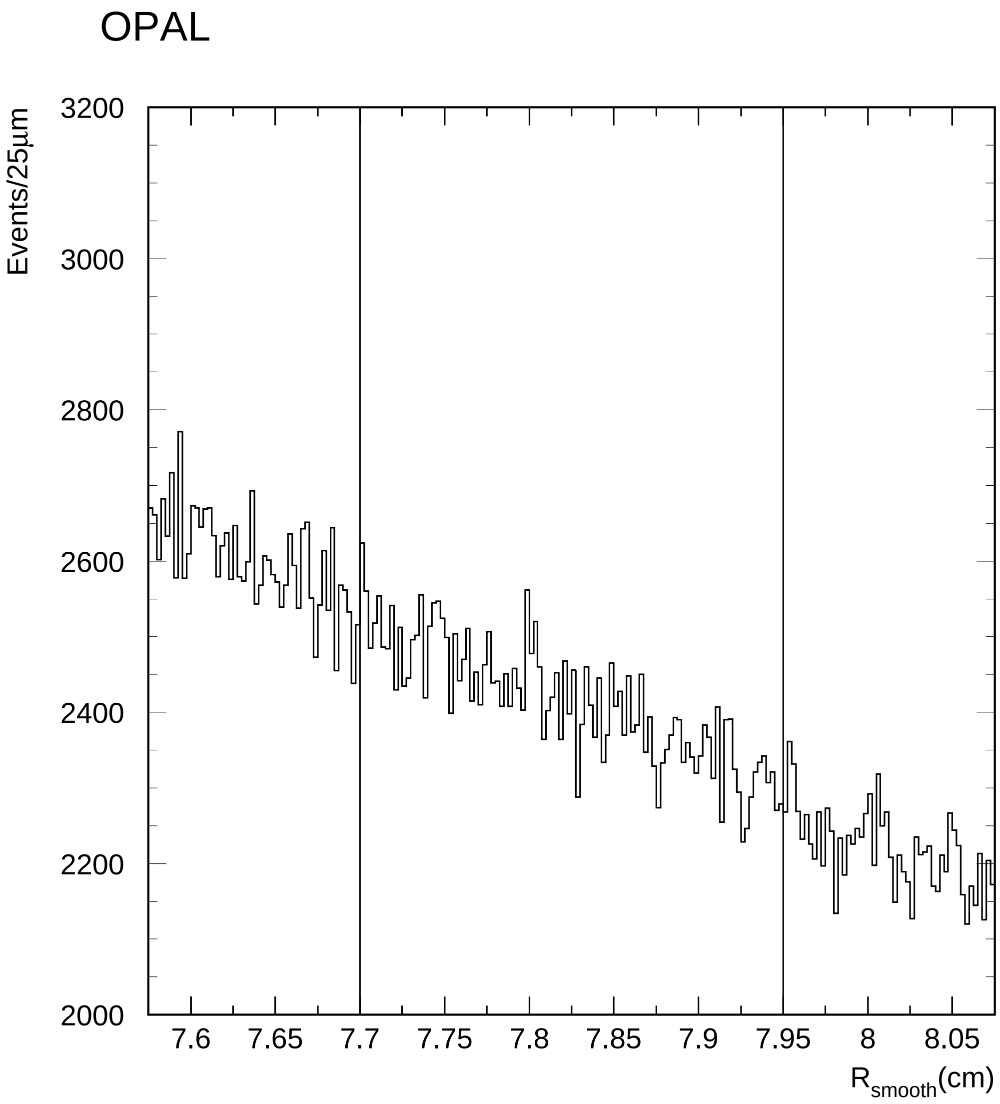

Figure 12: The distribution of the smoothed radial coordinates near the inner cut boundary in the right side calorimeter for the 94b luminosity data sample, with all Bhabha isolation cuts applied, except for any cut at all on the radial coordinate in either calorimeter. The vertical lines indicate the position of the pad boundaries in the reference layer of the calorimeter. No structure is apparent beyond statistical fluctuations, and the measured luminosity is independent of the radius chosen to define the inner edge of the acceptance.

as our primary measure of luminosity. The determination of the residual bias in the left and right coordinates individually forms the topic of the following section.

4.1.4 Anchoring

This section describes the method used to measure any remaining biases in the smoothed radial coordinate of the reconstructed electromagnetic showers. In determining the radial shower coordinate, we have made every effort to explicitly preserve the condition that a shower which deposits equal energies on two adjacent pads in the reference layer at $7X_0$ will be reconstructed, in the mean, to lie exactly at the boundary between the two pads. Due to the $r-\phi$ geometry of the pads, however, the pad area increases by about 3% per pad at the inner edge of the acceptance. In the mean, therefore, the true position of such equal-pad showers will lie at a smaller radius than the physical pad boundary, and this bias should be reflected in our smoothed radial shower coordinates.

This pad boundary bias depends sensitively on the lateral shower profile, which we found was not consistently modeled by existing detailed Monte-Carlo shower simulations. We therefore chose to measure this bias experimentally in a test beam.

The test beam utilized a SiW calorimeter module of 3 azimuthal wedges fully equipped in depth, and a four-plane, double-sided Si micro-strip telescope [?] with a resolution of better than 3μm for individual tracks. The geometry of the calorimeter pads with respect to the telescope was determined using a beam of 100 GeV muons which could be tracked through the individual pads of the calorimeter, since the SiW electronics is sensitive to individual mips. The muon beam was alternated with one of 45 GeV electrons, and measurements made to determine the pad boundary bias.

It might seem most straightforward to measure directly the radial bias of the reconstructed smoothed coordinate in the test beam. However, studies of the reconstructed coordinate (section 4.1.3) show that it is sensitive to the distribution and type of material in front of the calorimeter as well as to the incidence angle of the incoming particles, which at LEP changes continuously over the face of the detector. Because the divergence of the test beam was small, the angle of the incident particles was appropriate to mimic particles emanating from the beamspot at LEP for only a small fraction of the test beam events. This small sample of events was centered slightly above the region of the inner radial cut. Since it was not possible to reproduce exactly the OPAL beam geometry and the material in front of the calorimeters in the test beam studies, a more indirect approach, largely free of material and incidence–angle dependence, is used for determining the bias in the radial coordinate at LEP.

In this approach, called *anchoring*, we take the position of the pad with the maximum amplitude in a given longitudinal layer (the pad–maximum) as our fundamental tool. As the radial position of the incoming particles crosses a radial pad boundary in a single layer, the average pad–maximum moves rapidly from one pad to the next, giving an image of the pad boundary, as shown in figure 13.

The anchoring procedure uses the pad boundary image as the bridge between the OPAL data and the test beam data. In the test beam measurements, the pad boundary bias due to the finite shower size and the curved pad boundaries is measured with respect to the external beam telescope. In the OPAL data, the apparent pad boundaries are then used to measure any additional bias in the smoothed radial coordinate.

We now describe the anchoring procedure in somewhat more detail. The curve fitted to the test beam measurements of the pad boundary images in figure 13 is an error function (a Gaussian convoluted with a step function) whose width, w, we term the *pad boundary transition width.* We define the point at which the error function crosses the 50% level as the *apparent pad boundary.* We then take the difference between the apparent pad boundaries for electrons and muons as the *pad boundary bias.* We have measured the pad boundary bias at a great number of pad boundaries at different layers within the test beam module, with and without additional preshowering material. We find that over a large range of conditions, the results can be usefully described as a function of w, as shown in figure 14. The parameterization of the pad boundary bias as a function of w was determined from a linear fit to the test-beam data with the bare calorimeter. An error of 2.0 μm is assigned to the parameterization which safely covers other possible parameterizations such as the power law form also shown in figure 14. Data taken with additional material in front of the calorimeter is found to be adequately described by the parameterization determined from the bare calorimeter.

In OPAL running, we can not directly measure w since we lack a micro-strip telescope to determine the incident electron trajectories. However, we can measure the apparent width, w_a, of the pad boundary image in terms of the smoothed radial coordinate. Since both w and w_a can be measured in the test beam, the test beam measurements can be used to estimate w from the measured value of w_a as shown in figure 15. The error bars shown on the points for w indicate the uncertainty in the conversion from w_a to w. This uncertainty is estimated from the difference between the test beam data with no additional material and with 0.84 X_0 of material in front of the detector. At the reference

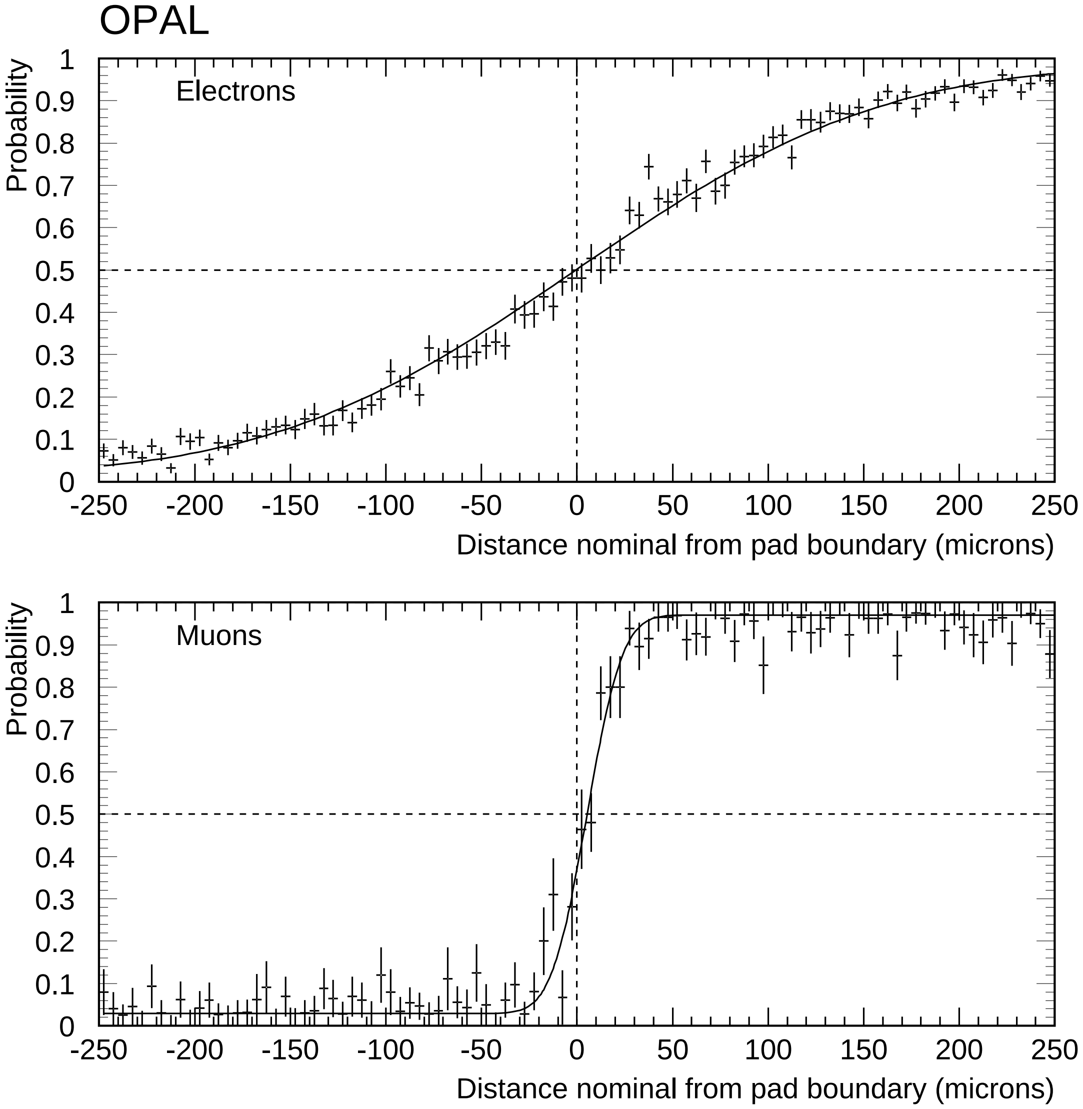

Figure 13: The pad boundary images for test beam electrons and muons at layer 7. Each image is formed by plotting the probability that the pad with maximum signal lies above a given pad boundary as a function of the incident particle trajectory. The measured pad boundary bias is the *difference* between the intersection of the fitted curves for electrons and muons with the 0.5 probability level. The horizontal axis is in micro-strip coordinates only nominally centered on the pad boundary.

layer (7 X_0) the w_a to w conversion contributes about $2\,\mu$m to the uncertainty in the net coordinate bias.

To apply the anchoring method to the LEP data, events are selected by applying all the SwitR and SwitL isolation cuts. This eliminates background from the sample. The coordinates on the right and left sides are then separately anchored. The first step of the anchoring is to scan through the pads in each layer to find the most energetic pad associated with the cluster, $i_{\max}$, which is not more than 2 pad widths (0.5 cm) from the average radial coordinate of the shower. This requirement is designed to eliminate spurious pad–maxima, interference from background, and multi-cluster events.

The image of the pad boundary is then formed by plotting the fraction of events (in a given layer) with a pad–maximum above a given boundary (i.e., $i_{\max} \geq i$) as a function of the radial calorimeter

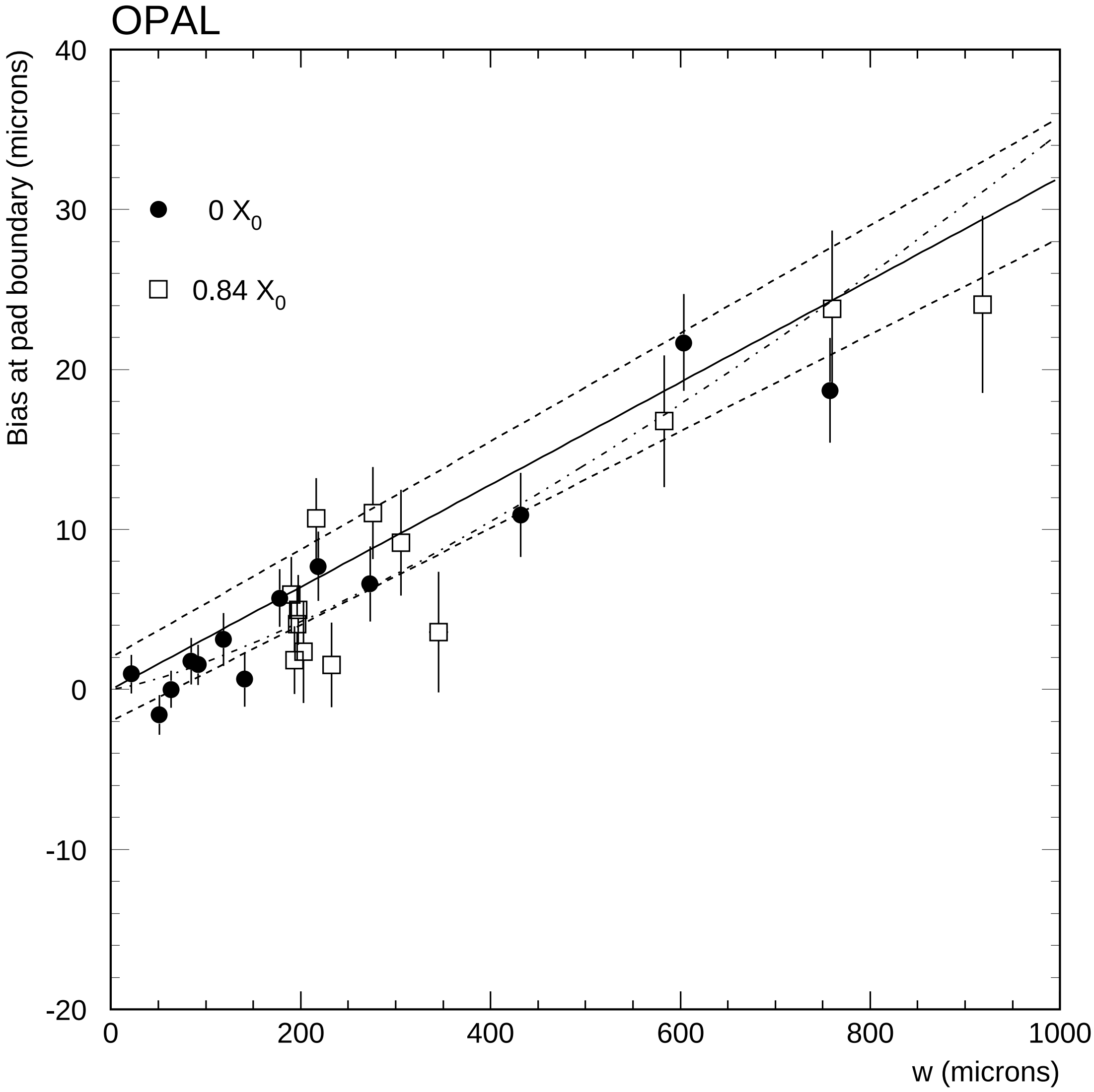

Figure 14: The pad boundary bias as a function of the measured pad boundary transition width (w). The data points correspond to measurements at different depths in the calorimeter. The solid circles show the bias for the bare calorimeter (0 X_0) and the open boxes the calorimeter behind additional dead material (0.84 X_0). The line was fitted to the 0 X_0 data. The dotted lines show the error assigned to the parameterization. The dash-dotted lines shows an alternative two parameter fit of the form ax^b.

coordinate R_{smooth}, as shown in figure 16. As for the test beam measurements, we model the pad boundary image with an error function

$$f(R; w_a, R_{\mathrm{off}}) = \int g(t; R, w_a)\theta(t - R_{\mathrm{off}})dt \tag{34}$$

where R is the distance from the nominal pad boundary, $g(t; R, w_a)$ is a Gaussian of width w_a and mean R, and $\theta(t - R_{\mathrm{off}})$ is a step function with offset, R_{off}, from the nominal pad boundary.

Figure 16 shows that a Gaussian resolution does not perfectly describe the tails of the distribution, even at the center of measurement. To the extent that the pad boundary image maintains an odd

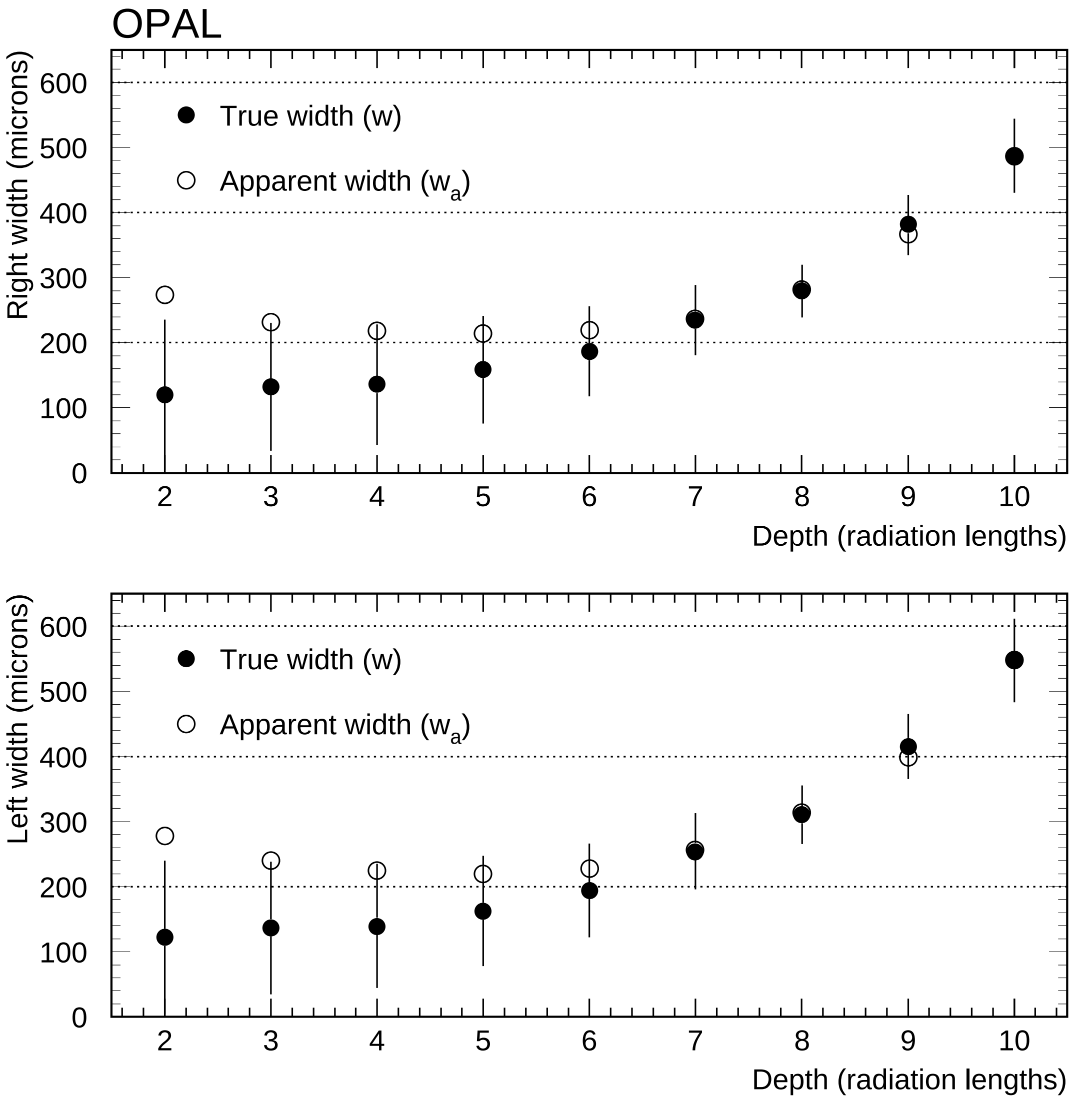

Figure 15: Apparent and estimated true values of the pad-boundary transition width, w, at the boundary between pad rows 6 and 7 (7.7 cm). The upper plot shows the right side, the lower plot the left side. The errors on the estimated true width reflect the uncertainty in the conversion of w_a to w.

symmetry about the apparent pad boundary, its non–Gaussian behavior does not affect the determination of $R_{\rm off}$, as can be seen from the close agreement of the data points and the fitted curve near the pad boundary. The effect of non-Gaussian resolution becomes more important deeper in the calorimeter as the showers broaden and traces of asymmetry appear. We have also considered a model in which the apparent pad boundary is taken as the median of the observed resolution function. Over a reasonable range of depths, the differences observed with respect to the Gaussian method set the scale for the $1.5\,\mu$m error we assign to our method of fitting the pad boundary image.

Using the measured values of w_a, the appropriate pad boundary bias measured in the test beam can be added to $R_{\rm off}$ to find the net bias in the smoothed coordinates for each of the luminosity samples. The results for our *primary anchor* at $R = 7.7$ cm and a depth of $7X_0$ are shown in tables 8 and 9. Note that, as expected, the values of $R_{\rm off}$ are small, and the inherent pad boundary bias dominates the net coordinate bias, so that the effect of the finite shower size is to cause the

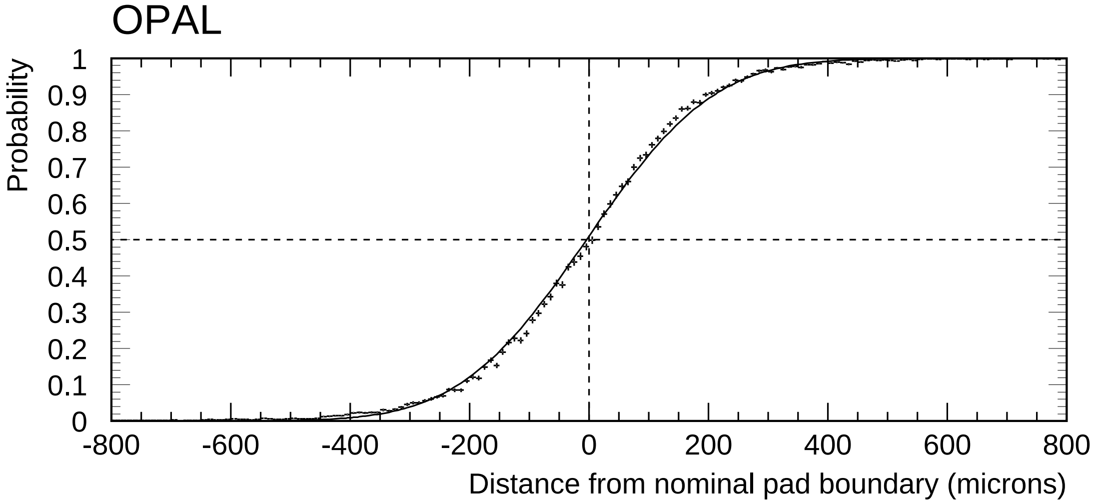

Figure 16: The pad boundary image at LEP. The fraction of events with maximum in pad row 6 or beyond, as a function of distance from the pad boundary between rows 5 and 6, for the layer located after 7 X_0. The solid curve shows the fitted function.

coordinates of the pad boundaries to be reconstructed at smaller radii than their true position (the net bias is positive). Additional small corrections to the anchors, due to resolution effects, have been applied using equations 11 and 15. These corrections account for the difference between the resolution flows of the radial coordinate and the apparent pad boundary.

Studies of $R_{\rm off}$ as a function of the 32 azimuthal divisions of the calorimeters, taking into account the detailed radial and longitudinal metrology of the pads as well as beam offsets, find that the residuals are approximately a factor of two larger than would be expected on the basis of statistical errors alone. The size of these extra azimuthal variations ($\sim 7.5\,\mu$m) is only slightly larger than the azimuthal variations in the average radial coordinate which would be generated by the largest pad gain fluctuations still compatible with the $\leq 0.25\%$ uniformity observed in our electronic calibrations ($\sim 5.5\,\mu$m, see section 4.1.2). Such gain fluctuations affect the apparent coordinates much more than the apparent pad boundaries. Since the anchoring procedure aligns the coordinates to the pad boundaries, it would be appropriate to use, as a systematic error in the net coordinate bias, the smaller gain-induced variations we could expect in the pad boundaries, $\Delta R = 2.5\,\mu\mathrm{m}/\sqrt{32} = 0.6\mu$m (see section 4.1.1).

We choose, however, to be more conservative, and ascribe all the unexplained azimuthal variations to the anchors rather than the coordinates, and take the corresponding

$$\Delta R = 7.5\ \mu\mathrm{m}/\sqrt{32} = 1.5\mu\mathrm{m}$$

as the systematic error in the net coordinate bias due to pad gain variations.

As expected, the anchors in alternating azimuthal towers, which correspond to the pattern in which the AMPLEX channel ordering is reversed in the anchoring layer, do not show any structure beyond the limit of statistical sensitivity of about 2μm.

The errors in tables 8 and 9 are dominated by systematic effects which we take to be common to all of the data analysis periods. The sources of these errors are summarized in table 12.

As expected, the net coordinate bias does not vary significantly as a function of data set, except for the 1995 data on the right side, where the amount of material in front of the detector changed considerably due to the installation of additional cables for the micro-vertex detector. We therefore average the 93-94 and 95 data separately, as shown in tables 8 and 9. We then use these average net coordinate biases, as measured at the inner fiducial boundary in layer 7, to calculate the acceptance correction shown in tables 8 and 9. We apply the average of the right and left inner anchor corrections to the (SwitR + SwitL)/2 acceptance, as shown in section 9, table 23. In propagating the inner anchor error to table 24, we also assume that all the errors are correlated between the left and right anchors, except for the measurement error in $R_{\rm off}$ and the error allowed for azimuthal variations.

The reconstructed radial coordinate can be studied by simultaneously varying the value of the radial cut in the data and in the Monte Carlo. The Monte Carlo assumes that the radial coordinate is reconstructed without bias. Thus any difference in the acceptance of the data and Monte Carlo as the inner cut is varied, beyond that expected from the finite statistics, can be attributed to residual structure in the radial coordinate. The relative acceptance, as a function of the value of the inner radial definition cut for both the SwitR and SwitL selections, is shown in figure 17 for the combined 1993–1994 data sample. The width of the shaded bands represent the binomial errors with respect to the standard selection, with its cut at 7.70 cm. The relative acceptance is remarkably flat, indicating the smoothing procedure has been properly applied to the data. Note that the smoothing procedure does not allow events to move across the pad boundaries at layer 7 X_0, i.e. at 7.45 cm, 7.70 cm and 7.95 cm, so that the data–Monte Carlo comparison at these points cannot be affected by the smoothing.

The unique pad boundary at 7.70 cm in layer 7 was chosen as the optimum point to anchor the coordinates (the primary anchor). A large number of other pad boundaries could have been chosen, and should give consistent results, assuming our methods are valid. The solid points in figure 17 show the anchoring results for the 5-6, 6-7, and 7-8 pad row boundaries and for layers between 2 X_0 and 10 X_0. The primary anchor at 7.70 cm has been required to lie at zero, while the other points demonstrate the consistency of other potential choices. Even at the level of the small residual structure in the smoothed coordinate, the alternative anchors track the expected acceptance variations for each of the pad rows and most of the depth range studied.

Looking at the anchor measurements as a function of depth, good agreement is seen for the layers near the center of measurement. For the deepest layers the difference between the anchors and the measured relative acceptance changes exceeds two standard deviations. The character of these differences might be expected, since the anchor measurements in the deeper layers are much more sensitive to gain variations and details of shower development than those at the center of measurement. The largest differences occur at the 7-8 radial pad boundary in the left calorimeter, where the amount of material between the detector and the interaction point is starting to become large and the test beam measurement of the expected bias may no longer be applicable. Furthermore, the non-Gaussian behaviour of the pad boundary image at layer 10 X_0 causes the anchor in this layer to be sensitive to the fitting method used. Presumably a more sophisticated treatment of the deeper layers would give better results, but the anchors in layers 2–9 X_0 are more than sufficient for a complete understanding of the radial coordinate.

We have also applied the anchoring method to determine the bias in the radial coordinate at the outer edge of the acceptance. The acceptance of the luminosity selections is approximately a factor of four less sensitive to the outer edge than it is to the inner edge, making the result less sensitive to biases in the smoothed coordinate in the outer region. Since we have no test beam measurements of the pad boundary bias for a radius of pad curvature corresponding to the outer edge of the acceptance, our analysis of the outer anchor is also necessarily less precise. We assume that the pad boundary bias scales according to our expectations (as $1/R$) but assign an additional systematic error equal to 50% of the expected bias to account for possible deviations from this behavior. We also treat the inner and outer anchor errors as being uncorrelated, the most conservative assumption.

The outer anchor acceptance correction is then calculated according to equation 12. Tables 10 and 11 give the anchoring results for the right and left sides of the detector, respectively. The average of the right and left outer anchor acceptance corrections and their uncertainties are entered in tables 23 and 24 in section 9. The outer anchor errors are taken as mostly correlated between the two sides, as

Sample	R_{off} (μm)	Estimated w (μm)	Net coordinate bias (μm)	Acceptance Correction ($\times 10^{-4}$)
93 −2	-1.6 ± 1.8	$232. \pm 62.$	6.7 ± 3.7	
93 pk	-4.7 ± 1.8	$232. \pm 58.$	3.6 ± 3.8	
93 +2	-4.8 ± 1.8	$229. \pm 62.$	3.3 ± 3.7	
94 a	-4.1 ± 1.8	$228. \pm 57.$	4.0 ± 3.7	
94 b	-5.0 ± 0.8	$237. \pm 64.$	3.5 ± 3.5	
94 c	-4.4 ± 3.1	$222. \pm 60.$	3.5 ± 4.4	
93–94	-4.6 ± 0.6	$237. \pm 64.$	4.0 ± 3.4	1.6 ± 1.4
95 −2	3.0 ± 2.0	$263. \pm 80.$	12.7 ± 4.1	
95 pk	1.7 ± 2.5	$255. \pm 77.$	11.0 ± 4.3	
95 +2	3.7 ± 1.9	$257. \pm 76.$	13.1 ± 4.0	
95	3.5 ± 1.2	$265. \pm 82.$	13.2 ± 3.8	5.3 ± 1.5

Table 8: Values of the right inner anchors at 7.70 cm in layer 7 for the nine data samples. The errors on R_{off} are statistical only. The errors on the net coordinate bias include the systematic error from the test beam measurement and are largely correlated between the data samples. The acceptance corrections due to the net coordinate bias are calculated for the 93-94 and 95 samples separately.

Sample	R_{off} (μm)	Estimated w (μm)	Net coordinate bias (μm)	Acceptance Correction ($\times 10^{-4}$)
93 −2	-0.4 ± 1.9	$257. \pm 57.$	9.0 ± 4.0	
93 pk	-0.3 ± 1.9	$250. \pm 55.$	8.8 ± 3.9	
93 +2	-1.7 ± 1.9	$243. \pm 54.$	7.1 ± 3.9	
94 a	-8.3 ± 1.8	$249. \pm 55.$	0.7 ± 3.9	
94 b	-2.1 ± 0.9	$258. \pm 57.$	7.3 ± 3.7	
94 c	-3.4 ± 3.0	$215. \pm 47.$	4.2 ± 4.4	
93–94	-2.4 ± 0.6	$257. \pm 56.$	6.9 ± 3.6	2.8 ± 1.4
95 −2	1.5 ± 1.9	$262. \pm 58.$	11.1 ± 4.1	
95 pk	-1.9 ± 2.5	$248. \pm 55.$	7.1 ± 4.3	
95 +2	0.9 ± 1.8	$244. \pm 54.$	9.8 ± 3.9	
95	0.6 ± 1.2	$258. \pm 57.$	10.0 ± 3.7	4.0 ± 1.5

Table 9: Values of the left inner anchors at 7.70 cm in layer 7 for the nine data samples. The errors on R_{off} are statistical only. The errors on the net coordinate bias include the systematic error from the test beam measurement and are largely correlated between the data samples. The acceptance corrections due to the net coordinate bias are calculated for the 93-94 and 95 samples separately.

they were for the inner anchor.

4.2 Azimuthal reconstruction

The determination of the azimuthal coordinate is based on a technique similar to the one used for the determination of the radial layer coordinates. Because of the relatively coarse azimuthal segmentation of the detector[7] the azimuthal coordinate relies primarily on the deeper layers of the calorimeter. Another important difference between the azimuthal coordinate and the radial coordinate is that the azimuthal towers are projective. Thus, the first step in the determination of the ϕ coordinate is to sum the pads associated with a given cluster longitudinally and radially. Typically the shower extends

---

[7] Recall that each layer of the detector is divided into 32 azimuthal segments, giving a pitch of 11.25° which corresponds to a width of 1.2 to 2.7 cm.

Sample	R_{off} (μm)	Estimated w (μm)	Net coordinate bias (μm)	Acceptance Correction ($\times 10^{-4}$)
93 −2	7.3 ± 4.1	$279. \pm 62.$	12.9 ± 6.0	
93 pk	24.3 ± 4.1	$262. \pm 58.$	29.4 ± 5.9	
93 +2	18.0 ± 4.3	$279. \pm 62.$	23.7 ± 6.1	
94 a	16.2 ± 4.0	$259. \pm 57.$	21.3 ± 5.8	
94 b	12.7 ± 2.0	$289. \pm 64.$	18.7 ± 4.9	
94 c	10.2 ± 7.4	$266. \pm 60.$	15.5 ± 8.5	
93–94	13.8 ± 1.4	$290. \pm 64.$	19.7 ± 4.8	-1.8 ± 0.4
95 −2	9.2 ± 5.0	$360. \pm 80.$	17.1 ± 7.5	
95 pk	15.5 ± 6.4	$345. \pm 77.$	23.0 ± 8.4	
95 +2	5.8 ± 4.7	$345. \pm 76.$	13.2 ± 7.1	
95	10.6 ± 3.1	$374. \pm 82.$	18.8 ± 6.6	-1.7 ± 0.6

Table 10: Values of the right outer anchors at 12.70 cm in layer 7 for the nine data samples. The errors on R_{off} are statistical only. The errors on the net coordinate bias include the systematic error from the test beam measurement and are largely correlated between the data samples. The acceptance corrections due to the net coordinate bias are calculated for the 93-94 and 95 samples separately.

Sample	R_{off} (μm)	Estimated w (μm)	Net coordinate bias (μm)	Acceptance Correction ($\times 10^{-4}$)
93 −2	8.5 ± 4.8	$376. \pm 83.$	16.8 ± 7.7	
93 pk	18.0 ± 4.8	$357. \pm 79.$	25.7 ± 7.4	
93 +2	16.0 ± 4.7	$339. \pm 75.$	23.3 ± 7.1	
94 a	6.4 ± 4.7	$362. \pm 80.$	14.3 ± 7.4	
94 b	10.8 ± 2.3	$402. \pm 89.$	19.9 ± 6.8	
94 c	17.2 ± 7.0	$257. \pm 58.$	22.3 ± 8.1	
93–94	11.2 ± 1.7	$399. \pm 88.$	20.2 ± 6.6	-1.8 ± 0.6
95 −2	-5.5 ± 5.0	$367. \pm 81.$	2.5 ± 7.6	
95 pk	3.8 ± 6.4	$352. \pm 78.$	11.5 ± 8.5	
95 +2	-0.3 ± 4.8	$353. \pm 78.$	7.4 ± 7.3	
95	-0.2 ± 3.1	$386. \pm 85.$	8.4 ± 6.9	-0.8 ± 0.6

Table 11: Values of the left outer anchors at 12.70 cm in layer 7 for the nine data samples. The errors on R_{off} are statistical only. The errors on the net coordinate bias include the systematic error from the test beam measurement and are largely correlated between the data samples. The acceptance corrections due to the net coordinate bias are calculated for the 93-94 and 95 samples separately.

Effect	Inner (μm)	Outer (μm)
Measurement of R_{off}	0.6	1.6
Test beam measurement of pad boundary bias	2.0	4.0
w_{a} to w conversion	1.9	1.6
Fit method	1.5	1.5
Azimuthal variations	1.5	2.9
Total	3.5	5.6

Table 12: Typical values of the errors for the inner and outer anchors near the longitudinal center of measurement. The error on the pad boundary bias and the effect of azimuthal variations track the shower size, which grows with the greater amount of preshowering material at the outer radius. We treat the inner and outer errors as being completely uncorrelated, the most conservative asumption.

over three or four of the 32 ϕ segments. In the summation, the deeper layers are given a larger weight.

The three most energetic contiguous ϕ segments are then used to calculate the quantity D given by equation 19. The distribution of the D values is then fit to the sum of two Lorentzian distributions, one with a narrow width and the other with a wider width. By integrating the differential distributions, the linearization function can be extracted. Because of the changing pad size, the parameters of the linearization were determined separately in bins of radial coordinate.

After applying the linearization, a reasonably flat ϕ distribution is obtained. Near the inner edge of the acceptance the resolution is approximately 10 mrad corresponding to 1/50 of a pad width. The resolution of the ϕ coordinate depends on radius and increases by approximately 20% at the outer edge of the detector.

The uncertainties in the parameterization of the azimuthal coordinate result in a negligible systematic error on the acceptance of the SwitR and SwitL selections. The complete azimuthal coverage of the detector allows the ϕ–coordinates to be ignored except in determining the acoplanarity. The azimuthal alignment of the right and left calorimeters is verified by measuring a mean acoplanarity for Bhabhas of 6.2 mrad, in excellent agreement with the value of 6.34 mrad expected from the magnetic deflection of the Bhabha electrons in the OPAL magnetic field. The azimuthal symmetry of both the detector and the Bhabha distribution ensures that there can be no integral scale error in the acoplanarity measurement. Any local scale distortions will cancel in the integral over ϕ, appearing only as a broadening of the effective resolution. The azimuthal resolution is determined from the width of the beam–centered acoplanarity distribution of full–energy Bhabhas. It is found to vary from 10–12 mrad as a function of radius, with some evidence for non–Gaussian features.

Since the acoplanarity cut is made on the steeply falling tails of the distribution (see section 10, figure 34) the resolution flow is

$$\frac{\Delta A}{A} \approx -\left(\frac{\sigma_{\Delta\phi}}{66\ \mathrm{mrad}}\right)^2 \times 10^{-3}. \tag{35}$$

For the measured $11 \times \sqrt{2}$ mrad resolution in $\Delta\phi$, the resolution flow in acoplanarity is -0.5×10^{-4}. Since the parametrized detector simulation does not account for the non–Gaussian features of the true detector resolution, 10% of this calculated resolution flow is taken as a systematic error in the acceptance.

4.3 Energy reconstruction

The reconstructed energy used in the luminosity analysis depends on both the energy response of the SiW calorimeters to individual showers and on the selection of the clusters which are used in the final energy sum. In this section we first discuss the energy characteristics of Bhabha events

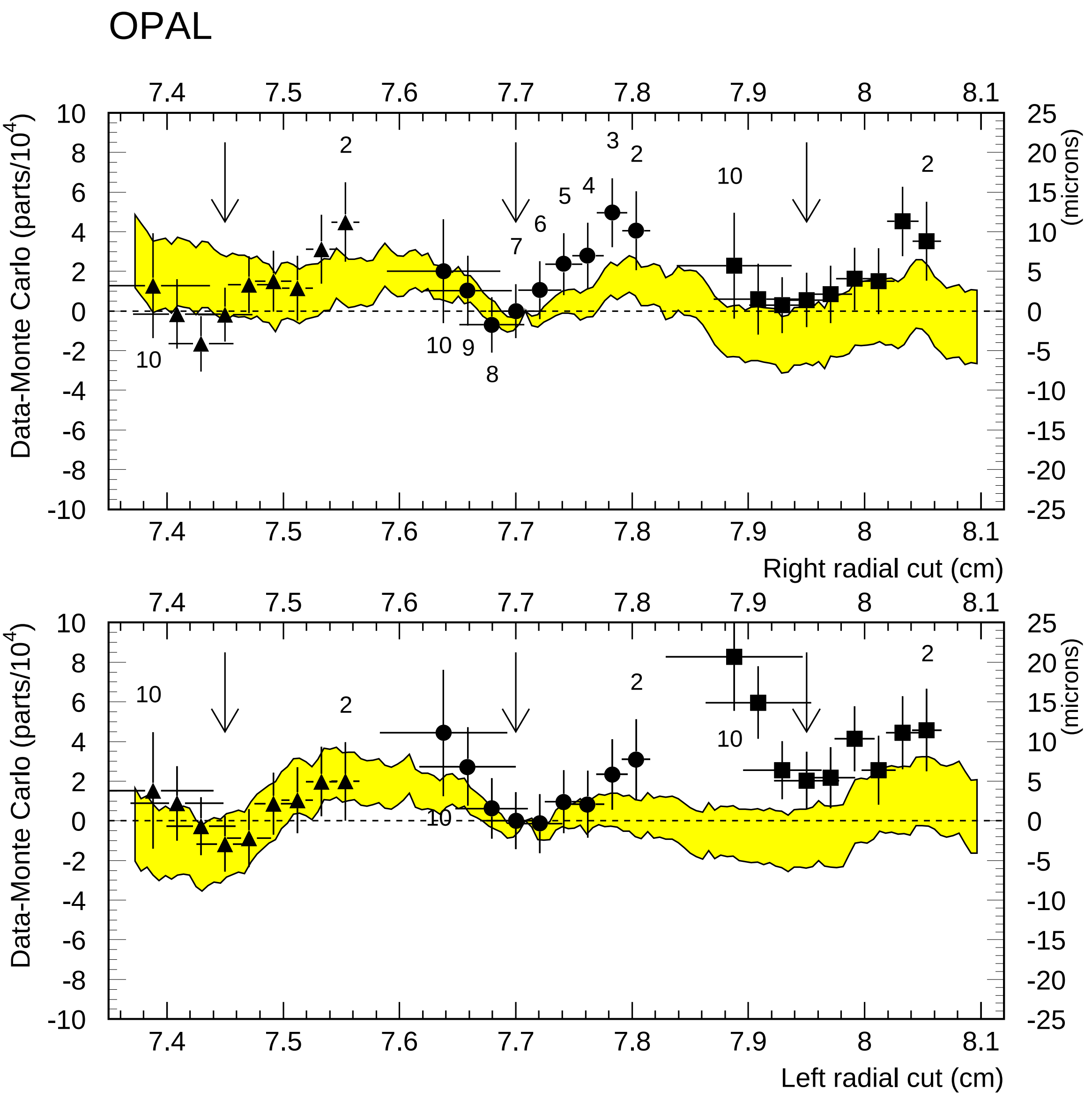

Figure 17: The shaded band shows the relative change in acceptance between data and Monte Carlo as a function of the definition cut on the inner radius for the SwitR and SwitL selections for the combined 1993–1994 data sample. Departures from zero beyond the highly correlated one-sigma statistical errors which correspond to the width of the band are due to the small residual structure in the reconstructed radial coordinate. The solid points show the coordinate bias measured by the anchoring procedure. The primary anchor at 7.7 cm is fixed to lie at zero. The deviations of the other anchors from the data/Monte Carlo band show the acceptance shifts which would result if any of the alternative pad boundaries had been chosen as the reference. Triangles, circles and squares indicate the 5–6, 6–7 and 7–8 pad row boundaries respectively. The numbers indicate the layer depth in radiation lengths. The arrows show the location of the radial pad boundaries at the center of measurement (7 X_0).

and describe how the energy cuts were chosen. We then describe the procedure used to correct the energy of individual clusters for the energy loss in dead material and describe how the detector energy response is extracted from the data and parameterized. Using a detector simulation based on this parameterization we are able to propagate the uncertainties in the measured energy response of the detector to the systematic error in the luminosity measurement. Uncertainties in the energy resolution tails and detector nonlinearity are found to be the dominant systematic effects. The effects of cluster selection on the energy measurement are also discussed and a summary of the energy-related systematic errors is given.

The distribution of the summed energy in the left and right calorimeters (after all other cuts) is shown in figure 18. The large accidental coincidence background, visible at small $E_{\rm R}$, $E_{\rm L}$ requires that relatively tight cuts be applied. Also apparent in the figure are the radiative tails of the distribution from events which have lost energy due to a single initial state photon emitted along the beam axis. For these events transverse momentum conservation implies

$$\frac{E_{\rm R}}{E_{\rm L}} = \frac{R_{\rm L}}{R_{\rm R}}, \tag{36}$$

so that an acollinearity cut effectively limits the energy lost to initial state radiation. The approximately 10 mrad acollinearity cut raises the minimum kinematically possible cluster energy for events radiating a single hard photon along the beam axis from $0.49E_{\rm beam}$, given by the ratio of the inner to the outer acceptance angles, to $0.75E_{\rm beam}$, safely above the explicit energy cuts, thus reducing the intensity of events near the cut boundary by about a factor of four (see figure 18).

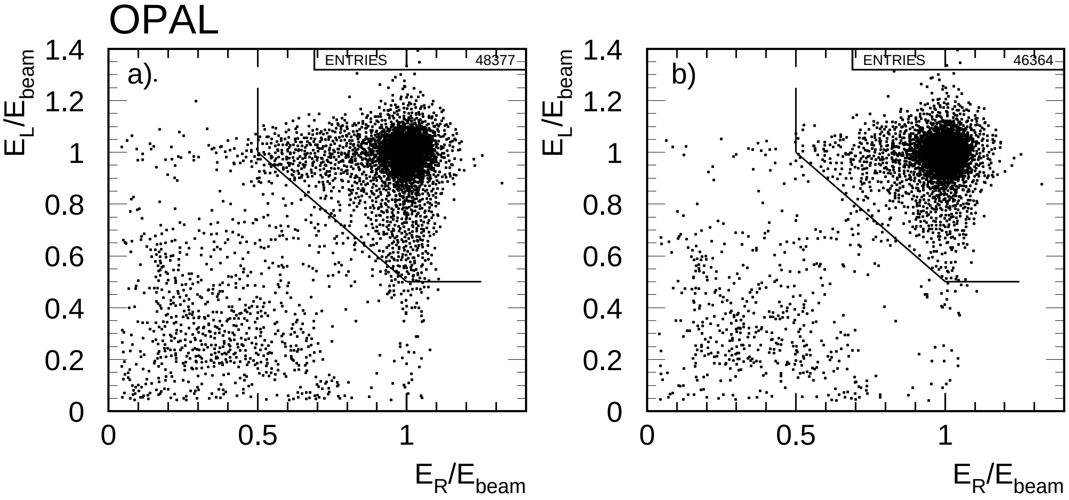

Figure 18: The distribution of $E_{\rm L}$ vs $E_{\rm R}$, after all the SwitA selection cuts have been applied, except for the energy cuts and the acollinearity cut (a). The effect of the acollinearity cut on the radiative events and background is clearly visible in (b). The lines in the $E_{\rm L}$ vs $E_{\rm R}$ plane indicate the cuts applied to the energies. The data shown here are from a typical run with approximately 40,000 SwitA events.

After the acollinearity cut, a change in the effective average energy response of the calorimeters results in a change in the fiducial acceptance of

$$\frac{\Delta A}{A} \approx \left(\frac{0.013\Delta E}{E}\right)$$

for a range of a few percent in $\Delta E/E$. As the average energy response of the detector relative to the beam energy can easily be adjusted to be the same in data and detector simulation, no signficant systematic error results from our knowledge of the overall energy scale. A sample of collinear events has been used to check the stability of the energy measurement. The average energy is stable at better than the percent level, leading to variations in the acceptance at the level of $\sim 10^{-4}$. Because of the small size of the variations, and because the method used to determine the energy response of the calorimeter automatically compensates for the variations in time, these variations in energy scale do not cause any additional systematic error to the SwitR, SwitL and SwitA acceptances.

The most important source of systematic error results from uncertainties associated with the treatment of fluctuations in shower development due to energy loss in upstream material and from longitudinal and lateral leakage. The upstream material (mostly from cables and support structures) has been kept to a minimum in the regions close to the inner and outer edges of the acceptance. However, in the middle of the acceptance the amount of material traversed by the incident electrons exceeds 2 radiation lengths (see figure 3). The energy lost due to leakage and preshowering has been parameterized as a function of both the radial coordinate of the shower and the ratio

$$F_{\rm pre} = \frac{E_{\rm pre}}{E_{\rm main}} \tag{37}$$

where $E_{\rm pre}$ is the energy deposited in the first four layers of the calorimeter (0 to 3 $\rm X_0$) and $E_{\rm main}$ is the energy deposited in the remaining layers, for a given shower. A sample of beam energy electrons can be obtained by imposing a very tight collinearity cut ($|R_{\rm R} - R_{\rm L}| < 1$ mm) and by requiring that the measured energy on the opposite side be close to the beam energy.[8] Note that except for a negligible fraction of double radiative events, the tight acollinearity requirement also selects events with a single cluster. Using this sample, the correction for dead material, in each of 60 radial bins, is found from a fit of the $F_{\rm pre}$ versus $E_{\rm raw}$ distribution as illustrated in figure 19. Near the inner and outer edges of the detector, where the upstream material is small, the energy response is dominated by lateral leakage and a simple scaling, independent of $F_{\rm pre}$ is applied to correct the raw energy. The raw and corrected energy for the left calorimeter as a function of radius are illustrated in figure 20.

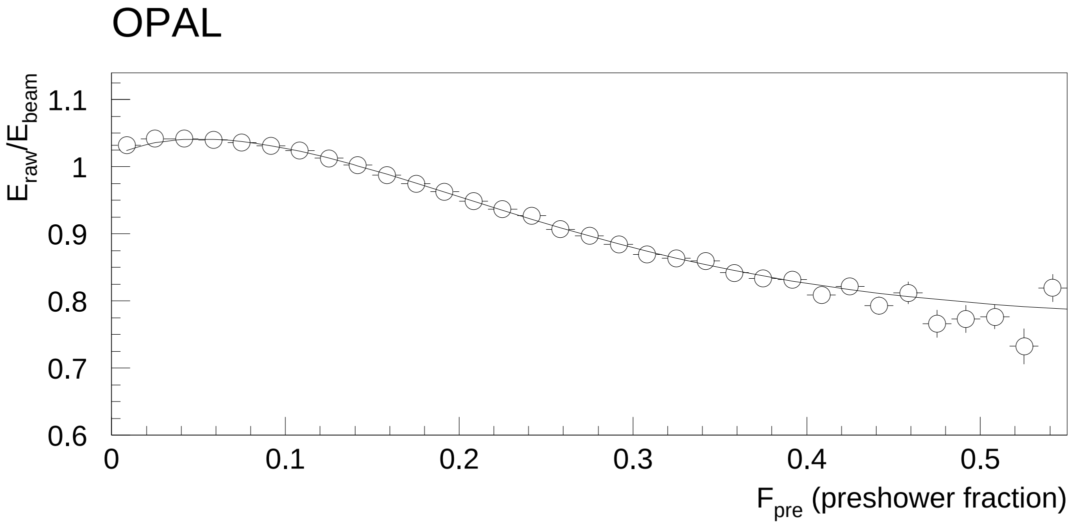

Figure 19: Mean raw energy, $E_{\rm raw}$, measured in the calorimeter as a function of the preshower fraction $F_{\rm pre}$, for showers near the center of the acceptance in the left calorimeter. The solid line shows the functional form used for the energy correction.

Figure 21 shows the distribution of corrected energies for collinear events in the central region of the SiW acceptance. On the right side, the energy resolution is approximately $\Delta E/E = 25\%/\sqrt{E}$

---

[8] For the studies of the calorimeter energy response discussed here, the coordinates of the scattered electron and positron were transformed to a system centered with respect to the LEP beam spot, so that the true collinearity angle is used as the reference.

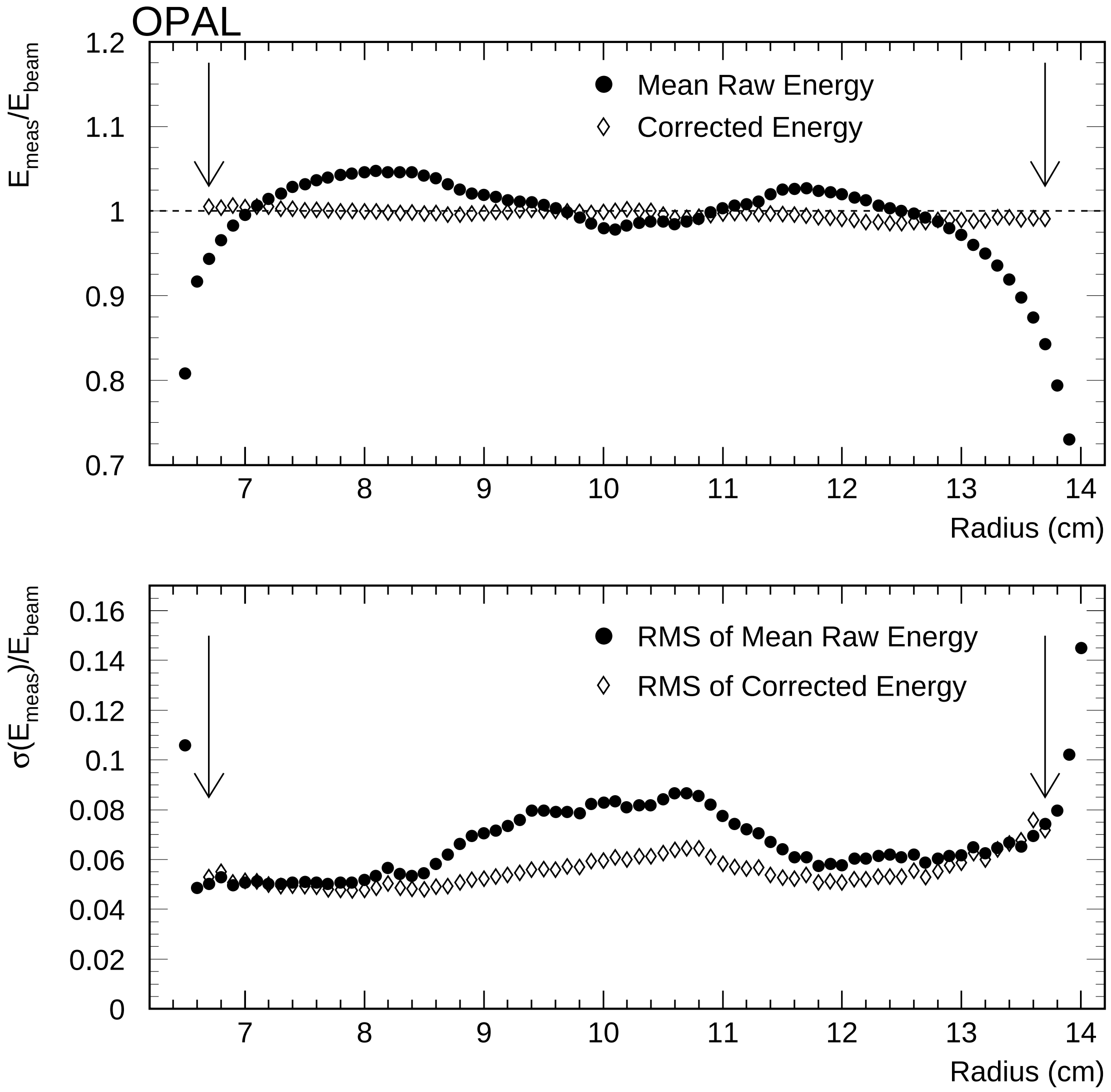

Figure 20: Mean raw measured energy and its RMS for a sample of collinear Bhabha electrons (solid dots), as well as the mean corrected energy and its RMS for the same sample (open diamonds). All quantities are shown as a function of radius for the left calorimeter. The correction algorithm ensures that the energy response of the calorimeter is not a function of radius, and recovers almost all of the resolution lost to preshowering in the region between 9 and 11 cm, where the amount of upstream material exceeds $2\mathrm{X}_0$. The vertical arrows indicate the position of the loose radial cuts. No clusters beyond these limits are used in the luminosity measurement.

in resonable agreement with the expectation of $\Delta E/E \sim 20\%\sqrt{\chi_s}/\sqrt{E}$, where χ_s is the sampling in radiation lengths and E is given in GeV. On the left side the energy resolution is degraded by the presence of cables from the silicon microvertex detector. In the region with the most material (near the middle of the radial acceptance) the energy resolution is approximately $\Delta E/E = 30\%/\sqrt{E}$.

In order to describe the detector energy response, the data have been divided into 60 radial bins and parameterized in each bin using two Gaussians of different widths and two Gaussians folded with exponentials with different exponents. The low exponential tail is due to events which shower very late in the detector, events which are not fully contained, and events with electrons or positrons that scatter off upstream material.

To optimise the energy response parameters, the simulated response function was applied to four–vectors generated by the BHLUMI 4.04 Monte Carlo simulation of small-angle Bhabha scattering [**?**]. The data and Monte Carlo energy distributions for events satisfying a tight acollinearity cut were compared as shown in figure 21, and the energy response parameters were adjusted to give the best agreement. In selecting samples of essentially beam-energy scattered electrons, the tight acollinearity cut prevented the manner in which photon radiation is implemented in the Monte Carlo from influencing the parametrization of the energy response function. The energy spectrum of the bare Monte Carlo four-vectors, also shown in figure 21, falls two orders of magnitude below the simulated detector response, showing that its shape cannot significantly influence the detector response tuning. If the response parameters had been optimised using an input delta function rather than the BHLUMI four–vectors, the result would have been functionally equivalent.

The most crucial feature of the energy response function is its integral below the single-side energy cut at $E/E_{\rm beam} = 0.5$. This controls the fraction of full-energy Bhabhas lost due to energy resolution effects. In figure 21 it can be seen that the response function describes this aspect of the data very well on both sides. For the left calorimeter the simulated response function describes the data everywhere extremely well, but for the right calorimeter, near $E/E_{\rm beam} = 0.8$, the data are somewhat below the model. This region of the response curve primarily affects the calculated acceptance for single radiative events with a low energy, well measured electron on the right, but a poorly measured full energy electron on the left. Such events are not numerous, and we have calculated that the visible descrepancy accounts for a systematic acceptance shift $< 4 \times 10^{-5}$, which we take as an energy response parametrization error in table 13.

The energy response of the detector at energies below the beam energy can be determined by using acollinear events which have energy in one calorimeter consistent with the beam energy. Using the ratio of radii of the showers in the right and left calorimeter (see equation 36) it is possible to predict the energy ratio of the two sides with a resolution of approximately 1%, resulting from the finite size and the divergence of the incoming beams.

In principle, some nonlinearity is introduced by the dead material in front of the calorimeter. Studies of the energy correction in the acollinear events show that, in the energy range of interest ($E_{\rm beam} > E > E_{\rm beam}/2$), the preshowering correction increases as the raw energy of the cluster decreases, compensating for the increasing fraction of energy lost in the dead material. Other possible effects are nonlinearities in the front-end electronics gain, imperfectly determined online electronics pedestals, imperfectly applied cross talk corrections, the ~ 4 MeV/channel threshold applied to the energy sum associated with a cluster, and leakage of energy near the edges of the detector acceptance.[9]

Using the sample of acollinear events, the residual nonlinearity has been measured on the right and left sides separately. The largest deviation seen between the expected and observed energy is approximately 0.4 GeV. Figure 22 shows the difference between the observed and expected energy as a function of the expected energy for both uncorrected and corrected data. The expected energy is calculated from the beam energy and the ratio of the radii of the two showers as described above. Also shown in figure 22 is the expected value of this difference from the detector simulation (see section 8). The apparent nonlinearity visible in the figure in both the data and the Monte Carlo arises from effects of the finite size of the LEP beams and their divergence convoluted with the rapidly falling spectrum of initial state radiation. Studies of data taken well above the $\rm Z^0$ resonance show that a cancellation occurs between the slightly positive contribution from the imperfect cross-talk correction and the negative contribution from the pad threshold, giving a quite linear response for energies below 50 GeV.

No evidence was found of any dependence of the nonlinearity on radius, indicating that nonlinearity due to shower leakage is not important for the event samples used to measure the luminosity.

---

[9] In test beam studies with a bare calorimeter, the energy reponse of contained showers was found to be linear within the sensitivity of the measurement (approximately 1%). However, these studies can not be directly applied to the OPAL running because differences in the hold timing and the trigger rate required special cross talk and pedestal corrections be applied to the test beam data.

The nonlinearity was separately measured for the 1993–1994 data and the 1995 data because of the additional microvertex cables installed on the right side in the 1995 run. The small sample of data taken in 1995 at center-of-mass energies near 133 GeV was also used to constrain the 1995 nonlinearity correction. No differences, within the 0.45 GeV/E_{beam} error, between the expected and observed energies were seen.

The parameters describing the energy response in the detector simulation have been varied within bounds consistent with the precision with which they have been derived, allowing the systematic error due to the cuts on energy to be assessed. These variations included changing the contribution from the exponential tails by 50%, scaling the widths of the Gaussians by ±10%, and changing the method used to extrapolate the energy resolution to lower energies. The allowed values of the nonlinearity were conservatively assigned on the basis of a statistics-limited check with the 1995 high energy data (at 133 GeV). Any possible nonlinearity was shown to distort the energy scale by less than $\pm 0.01 E_{\text{beam}}$ at $E = E_{\text{beam}}/2$. The effect of these parameter variations on the predicted energy distribution is also shown in figure 21. The band of variation is obtained by adding the variations for each of the four effects in quadrature.

	Systematic error ($\times 10^{-4}$)	
Effect	With acoll. Cut	Without acoll. cut
Change tail ±50%	1.2	2.1
Nonlinearity ($\pm 0.01 E_{\text{beam}}$ at $E = E_{\text{beam}}/2$)	1.2	3.2
Scale Gaussian ±10%	0.4	1.6
Low energy resolution	0.4	2.4
Right side parametrization error	0.4	0.4
Total	1.8	4.8

Table 13: Summary of the systematic error in the luminosity due to uncertainties in the detector energy response. These errors were estimated by varying the detector energy response parameters within the precision with which they could be determined from the data.

Table 13 summarizes the systematic errors assigned to the uncertainty in each aspect of the calorimeter energy response discussed above. The total systematic uncertainty on the luminosity due to uncertainty in the energy response is 1.8×10^{-4}.

Table 13 also demonstrates that the acollinearity cut reduces the acceptance uncertainty due to the energy cut by more than a factor of two. We have explicitly compared the results of the luminosity determination with and without the acollinearity cut. The data and Monte Carlo simulation track each other to within 1×10^{-4}, even though the density of events near the energy cuts increases by a factor of approximately four.

Another potential systematic error in the energy measurement can arise from the method used to select clusters to include in the energy sum. If only the most energetic cluster in each calorimeter were used in the energy sum, our analysis would be sensitive to the implementation of final state radiation in the physics Monte Carlo and to the modeling of two-cluster separation in the detector simulation. By summing the energy over the fiducial acceptance of the detector, our analysis is insensitive to the detailed implementation of final state radiation and to the modeling of two-cluster separation. The kinematic cluster selection algorithm discussed in section 3.2 efficiently includes the clusters which belong to the Bhabha scattering event while rejecting the background clusters generated by the off–momentum electrons discussed in section 5.

We have also varied both of the energy cuts used in the analysis and compared data and Monte Carlo. The minimum (E_{min}) and average (E_{ave}) energy cuts were simultaneously varied so that the minimum energy requirement for a single radiative event remained coincident with the average energy cut, i.e. $E_{\text{ave}} = (1 + E_{\text{min}})/2$, as in the standard set of cuts shown in figure 18. The comparison for the 1993 and 1994 data is shown in figure 23. For this comparison a detailed background subtraction based on our delayed coincidence trigger sample has been performed in each energy bin (see section 5). It can be seen that, with the acollinearity cut applied, the measured luminosity changes by less than 10^{-4} as the average energy cut is varied in the range from 0.7 to 0.8 of the beam energy. (Also shown in figure 23 is the variation without the acollinearity cut.) Similar results were obtained for the 1995 data samples.

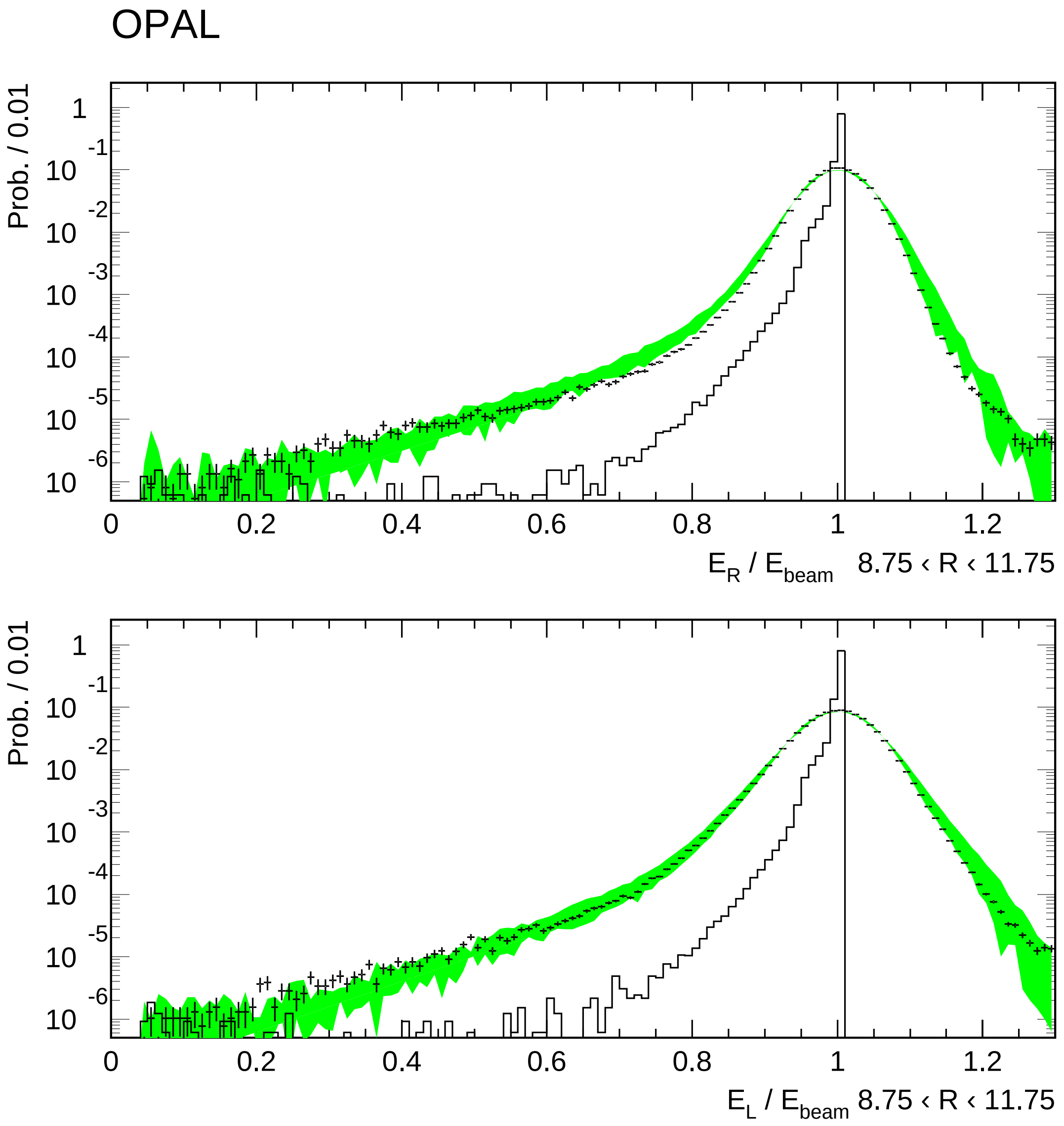

Figure 21: The observed detector energy response to very collinear events, with $|R_\mathrm{R} - R_\mathrm{L}| < 1$ mm, (points) which is used to parameterize the detector simulation (shaded band) for showers in the radial region between 8.75 and 11.75 cm. The width of the shaded band shows the variation in the parametrization used in setting the systematic error. Because of the tight acollinearity cut applied to the samples, single radiative and double radiative events are highly suppressed, and the observed distribution is dominated by resolution effects, as illustrated by the narrow histogram of the bare BHLUMI four–vectors, whose tail falls two orders of magnitude below the simulated detector response.

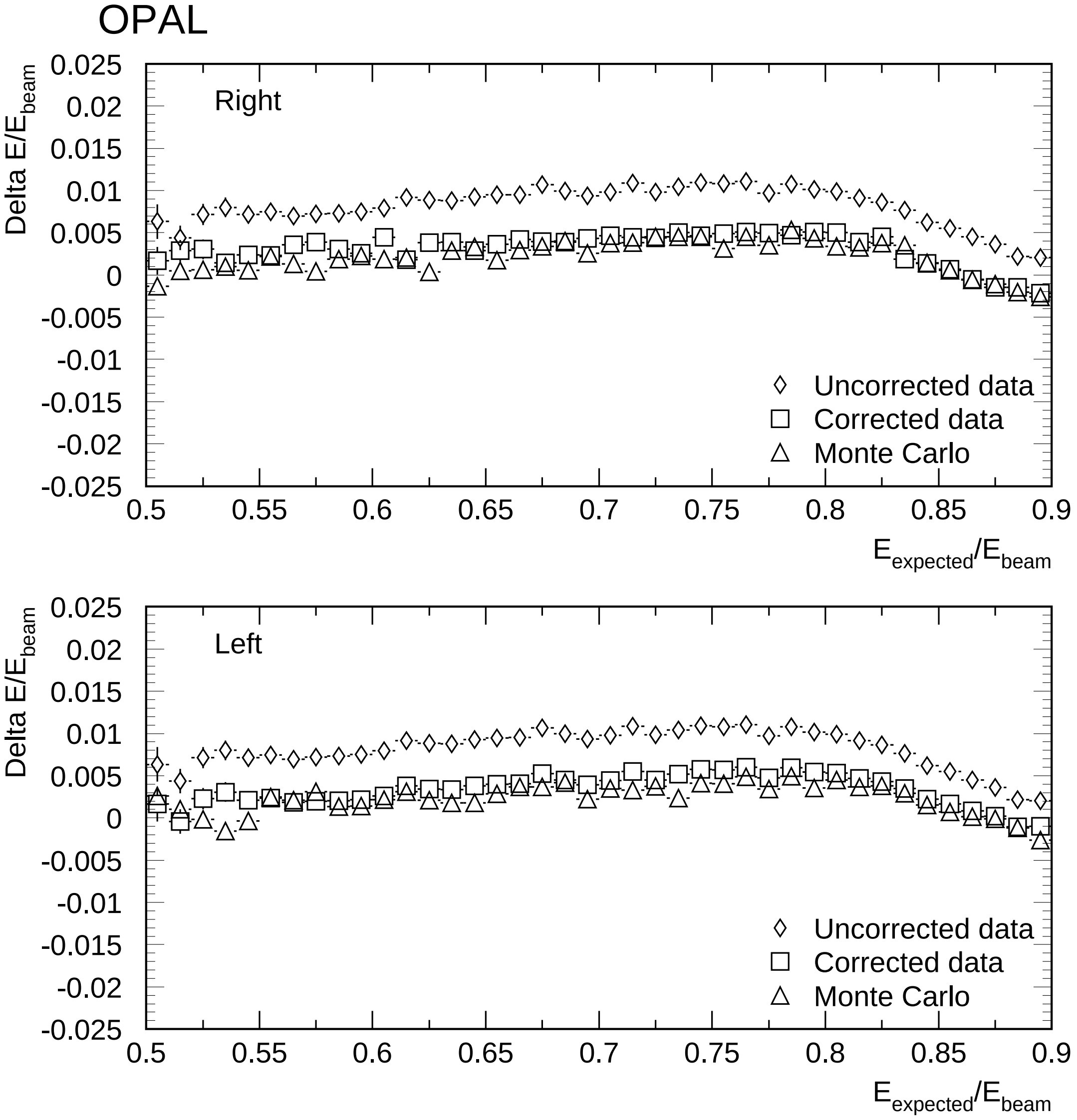

Figure 22: Fractional difference between the expected energy (calculated from the radii of the scattered electron and positron) and both the corrected and uncorrected measured energy for the sample of acollinear events. Also shown is the difference expected from the detector simulation. The apparent nonlinearity visible in both the data and the Monte Carlo above a fractional energy of 0.8 arises from effects of the finite size of the LEP beams and their divergence convoluted with the rapidly falling spectrum of initial state radiation.

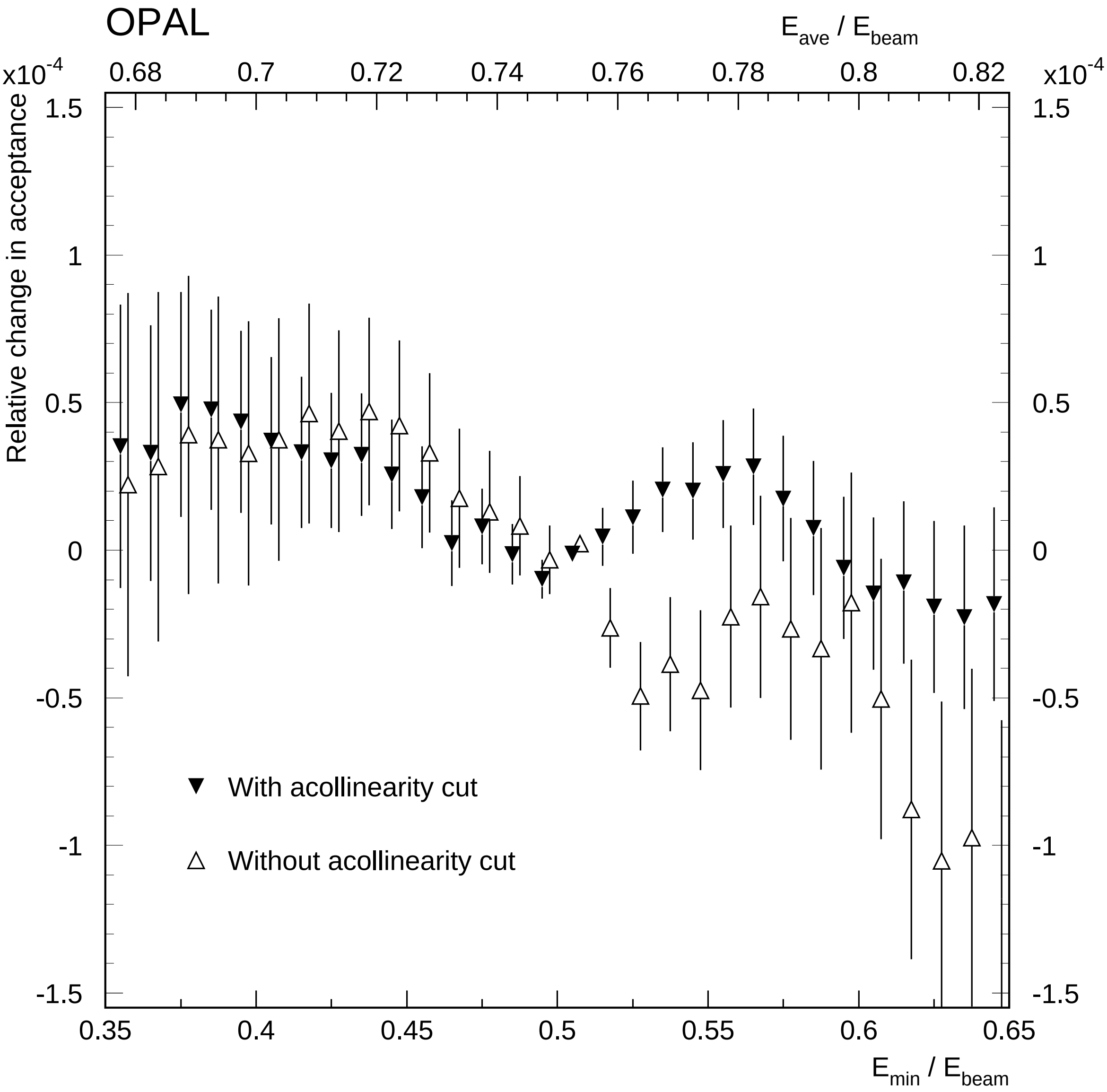

Figure 23: The relative change in acceptance between the Monte Carlo and the 1993–1994 data as a function of scaling the energy cut. The observed deviations are well within the systematic error assigned to detector energy response. The error bars show the binomial uncertainties with respect to the standard cut values.

5 Background and accidentals

The primary source of background to the luminosity measurement is from off-momentum electrons and positrons generated by beam-gas scattering in the straight RF sections on either side of the experiment which are deflected by the mini-beta quadrupoles into the luminosity monitor. The size of this background varies with time, and depends on the quality of the vacuum in the straight sections on either side of the OPAL interaction region and on the settings of the LEP collimators. The occupancies of the left and right calorimeters for clusters with $E > 1.0$ GeV, averaged over the 1993, 1994 and 1995 runs, are given in table 14. The 1993 and 1994 values are from the occupancy of random triggers. In the 1995 bunch train running, random triggers can only be used to measure the occupancy of the last bunchlet. Therefore, in 1995 the occupancy was estimated from the rate of extraneous clusters in non-radiative Bhabha events.

calorimeter	1993	1994	1995
right	8.0×10^{-3}	5.1×10^{-3}	8.4×10^{-3}
left	5.1×10^{-3}	3.7×10^{-3}	6.2×10^{-3}

Table 14: Probability for a cluster of $E > 1.0$ GeV to be found in the right or left calorimeters for the 1993, 1994 and 1995 runs.

The background from off-momentum particles affects the luminosity measurement in two ways. Accidental coincidences between background clusters in the right and left calorimeters can produce events which will potentially pass the SwitR and SwitL selection. The accidental overlap of a background cluster with a Bhabha event can also change the values of reconstructed quantities, modifying the acceptance.

The rate of random coincidences between background in the left and right calorimeters is approximately given by the product of the rates and is of order 5×10^{-5} per beam crossing. This rate is comparable to the rate expected for true Bhabha events. Fortunately the background events are primarily at low energy and can be isolated from Bhahba events as was shown in section 4.3, figure 18.

In the 1993 and 1994 data, this background can be studied using delayed coincidence triggers. Because the trigger signals from every beam crossing are digitized and recorded, it is possible to form a trigger which requires a coincidence when one side is delayed by one full revolution of LEP with respect to the other. In these events, full detector readout is only available from the current beam crossing. For the delayed beam crossing, only trigger information is available. The calorimeter which exceeds the trigger threshold in the current beam crossing is called the in-time side. The opposite calorimeter is referred to as the out-of-time side. The available information allows the energy and the azimuthal coordinate of the out-of-time side to be reconstructed, but not the radius. In order to apply our standard selection procedure to the delayed-coincidence events, the radial coordinate of the out-of-time side is randomly generated as a function of azimuth and energy from the three-dimensional distribution of R,E, and ϕ seen in that calorimeter when it was the in-time side in the sample of the delayed-coincidence triggers. This procedure assumes that the correlations among energy, radius and azimuth are relatively constant for a given year.

Figure 24 shows the lower portion of the 1994 total energy spectrum with all cuts applied, except that on the total energy. The background, as calculated using the method described above, agrees with the observed event rate at low energies to better than 10%. The out-of-time background events above the cut on the total energy of $(E_{\rm R}+E_{\rm L})/(2E_{\rm beam}) > 0.75$ are used to determine the background in the selected luminosity sample. The background fractions for 1993 and 1994 were between 0.1 and 0.6×10^{-4}. The small number of accidental triggers which passed all cuts gave a statistical error of about 30% on the background which is much larger than the 10% systematic uncertainty.

The determination of the coincidence background in 1995 is somewhat more involved. For almost all of the 1995 running, the SiW “wagon tagger” was configured to require a coincidence between the energy deposition in the left and right calorimeters, before issuing a hold signal to the front end

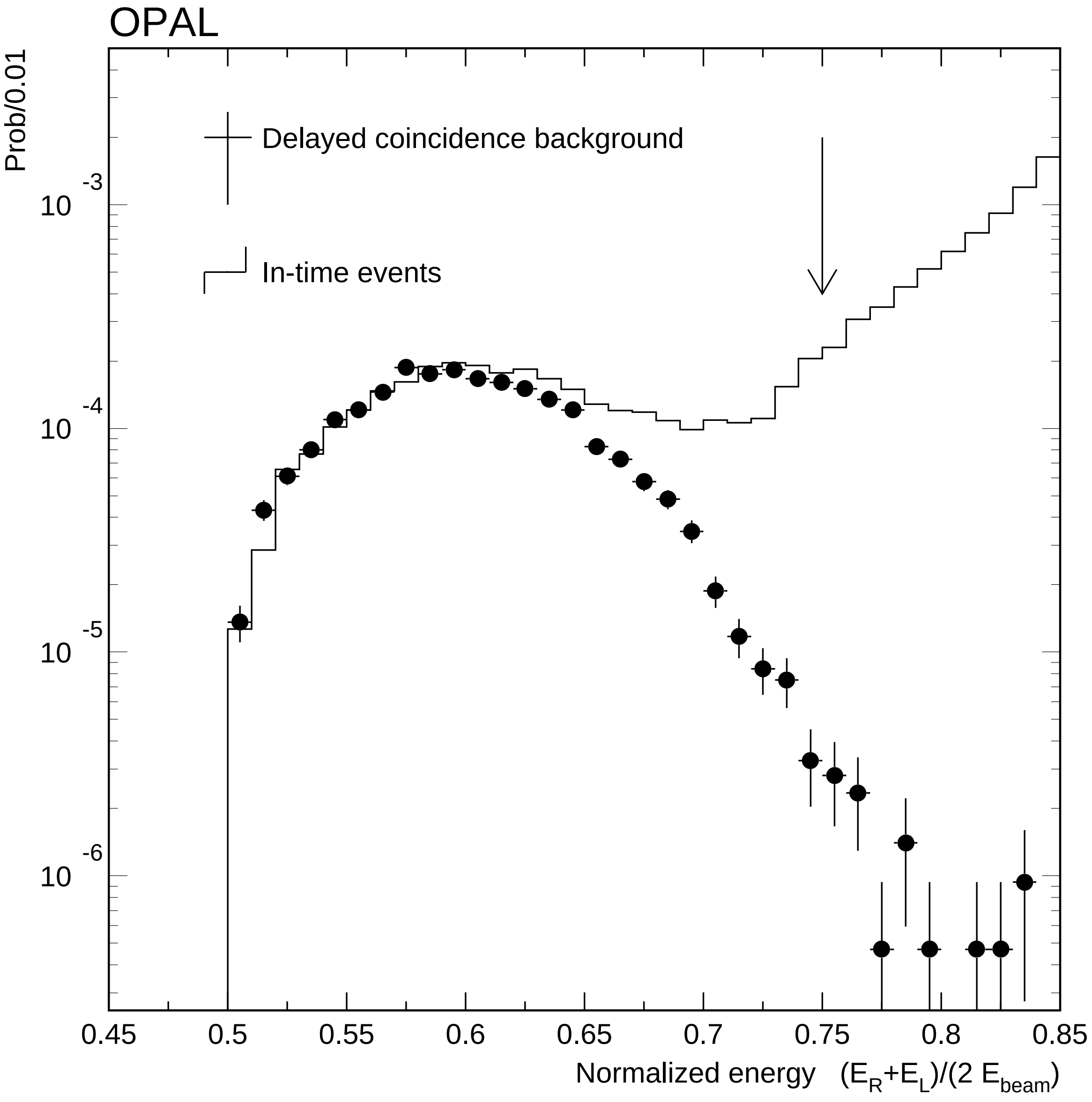

Figure 24: The low energy tail of the total energy spectrum normalized to the number of accepted luminosity events for the 1994 data (histogram). The points with errors show the background spectrum derived from the delayed-coincidence triggers. The arrow indicates the position of the selection cut made on the average energy.

electronics. If no coincidence was found, the hold signal was asserted on the last bunchlet. This means that the delayed-coincidence trigger only operated properly for the last bunchlet of each train. For earlier bunchlets, the measured energy was less than the true energy. For example, a hold issued on the last bunchlet measured only 15% of energy deposited on the first bunchlet and 50% of the energy deposited on the second bunchlet.

A second consequence of the “AND mode” of operation was that only coincidences between the same positron and electron bunchlets can produce background which is energetic enough to pollute the signal region. If the off-momentum background for the three bunchlets were equal, the delayed coincidence trigger would simply measure one third of the background. The characteristics of the background in the three bunchlets was studied by using the background ("extra") clusters in full-energy back-to-back Bhabha events. The overall energy spectrum of the background in each of the bunches was found to be similar, but the rate depended on the bunchlet. Using the shape of the background as measured in the last bunchlet and normalizing the energy spectra of the predicted background to the low energy tail of the in–time data, the background was determined separately for each of the three energy points as illustrated in figure 25. Note that the cuts on the right and left calorimeter energies ($E_{\mathrm{R}} > 0.5 \cdot E_{\mathrm{beam}}$ and $E_{\mathrm{L}} > 0.5 \cdot E_{\mathrm{beam}}$) have already been applied, leaving only the high energy tail of the background. The resulting corrections for the 1995 accidental coincidence background are between 0.1 and 0.15×10^{-4}, as shown in table 23.

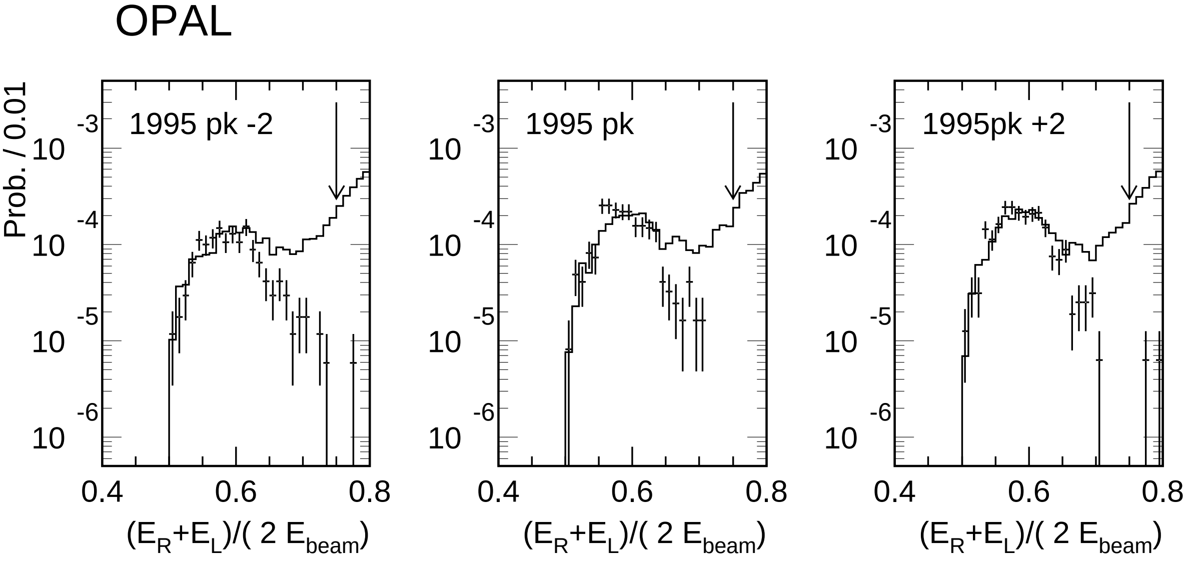

Figure 25: The low energy tail of the total energy spectrum normalized to the number of accepted luminosity events for the three 1995 energy points. The data points show the accidental background as derived from the delayed coincidence accidental triggers and rescaled to account for the background distribution among bunchlets. The arrows indicate the position of the selection cut made on the average energy.

Off-momentum electrons can also strike the detector in coincidence with a true Bhabha event. Such *overlap background* can cause Bhabha events which would have otherwise failed the selection cuts to pass them. It can also cause Bhabha events which would have otherwise passed the selection cuts to fail them. These effects have been evaluated by incorporating the measured background into the detector simulation as described in section 8, and produce an increase in the acceptance of less than 10^{-4}. This effect has also been evaluated by convoluting the measured background with data events. In this case, slightly larger values for these effects were found. We assign a systematic error of 1.0×10^{-4}, divided equally into components correlated and uncorrelated among the different data analysis samples, which covers the difference between the two methods and allows for the uncertainty associated with the implementation of two-cluster separation in the detector simulation. This uncertainty dominates the total uncertainty assigned to background effects, as shown in table 24.

A particularly striking form of overlap "background" occurs when two Bhabha scatterings are recorded in the same bunch crossing. At typical LEP luminosities of 3×10^{30} sec^{-1}cm^{-2}, a few $\times 10^{-6}$ of all SiW Bhabha events can be expected to be overlaid with a second Bhabha, consistent with observations. We count such double-Bhabhas as one, and make no correction for such overlaps.

6 Trigger efficiency

SiW luminosity events are triggered by two signals based on hardware sums of the energy deposited in the calorimeters: SWSEG, which requires deposition of energy in back-to-back segments in the two calorimeters, and SWHILO, which requires a large total energy deposition in one of the calorimeters and a smaller total energy deposition in the other.

Since the nominal hardware thresholds lie well below the minimun energies required to accept fiducial Bhabha events, demonstrating that the trigger system provides adequate efficiency primarily requires studying the mechanisms which can generate low energy tails in the trigger response. One such mechanism involves electronic effects which cause small, but coherent, shifts in the pedestals of the large number of individual channels which need to be summed. Such shifts occur when the steady rhythm of track/hold signals is disturbed, either by the readout of a triggered event, or by a rejected pretrigger. These shifts after a rejected pretrigger can be as large as 10 GeV for the total energy sum used in SWHILO, but less than 2 GeV for the segment sums used in SWSEG.

Another mechanism involves the energy absorbed in material upstream of the calorimeters. The corrections applied to the measured cluster energies on the basis of the longitudinal shower profile allow such absorption to be largely compensated in the luminosity selection (see section 4.3), but the hardware trigger signals are sensitive only to the energy actually deposited in the detector.

The digitized values of the raw trigger signals stored with each read out event allow the relations between the fully corrected cluster energies and the energies seen by the trigger to be studied in detail. We use the large sample of full-energy Bhabhas to measure the extreme tails of the distribution of differences between the corrected cluster energy and the trigger energy all the way down to trigger threshold. We then transport the difference spectrum away from the peak to estimate the number of radiative Bhabhas which might have been lost due to unfavorable trigger energy fluctuations. These studies carefully preserve the temporal and spatial pattern of correlations in the trigger signal fluctuations induced by the two chief known mechanisms mentioned above.

Since the event sample used in these studies requires a SiW Bhabha to have successfully triggered, a truely catastrophic failure mode of the trigger system might remain masked. To uncover such possibilities, we also studied a sample of over 600,000 events independently triggered by the OPAL forward-detector calorimeter with shared energy in SiW. No catastrophic SiW trigger failures were observed, giving a lower limit of 0.37×10^{-5} on the SiW trigger system efficiency at 90% CL.

Figure 26 shows how the calculated trigger efficiency contours are well adapted to the distribution of energies in fiducial SWITA events. Table 15 gives the calculated trigger inefficiency integrated over the Bhabha event distribution for each year of data.

In 1995 the proper functioning of the wagon tagger was also necessary for valid luminosity measurements. The fact that the SiW hold was issued on the last bunchlet of each bunchtrain, even if the tagger did not fire, allowed us to measure the tagger efficiency on last-bunchlet fiducial Bhabhas in a straight-forward manner. In the entire sample of 1,230,114 such events, 18 failures were observed, as shown in figure 27. All the tagger failures are due to showers with extremely late or early development profiles which deposited essentially no energy in the wagon tagger layers. Considering all bunchlets, we estimate the fraction of fiducial Bhabhas lost due to wagon tagger inefficiency is 1×10^{-5}, with an uncertainty of 2×10^{-6}.

7 LEP beam parameters

In this section we consider the effects of the LEP beam geometry on the luminosity measurement. Although the Bhabha selection procedure is chosen to minimize these effects, the luminometer acceptance is affected in second order due to the fact that the LEP beams depart from the ideal geometry of beams free of angular divergence passing on-axis through the center of the bores of the two calorimeters.

We utilize the considerable power of the SiW luminometer itself, as well as measurements using the OPAL tracking detectors and constraints from operational parameters of the accelerator to determine

1993 estimated SiW trigger inefficiencies			
Beam energy (GeV)	SWSEG $\times 10^{-5}$	SWHILO $\times 10^{-5}$	Total $\times 10^{-5}$
43.57	3.5 ± 1.3 ± 0.9	692 ± 7 ± 14	0.14 ± 0.38 ± 0.18
44.57	2.7 ± 1.2 ± 0.7	538 ± 7 ± 12	0.12 ± 0.38 ± 0.17
45.57	2.1 ± 1.2 ± 0.6	380 ± 6 ± 9	0.09 ± 0.37 ± 0.16
46.57	1.6 ± 1.2 ± 0.5	240 ± 4 ± 7	0.07 ± 0.37 ± 0.14
47.57	1.2 ± 1.2 ± 0.4	137 ± 3 ± 4	0.06 ± 0.37 ± 0.14

1994 estimated SiW trigger inefficiencies			
Beam energy (GeV)	SWSEG $\times 10^{-5}$	SWHILO $\times 10^{-5}$	Total $\times 10^{-5}$
45.57	0.02 ± 1.2 ± 0.01	21 ± 1.1 ± 0.8	0.001 ± 0.37 ± 0.001

1995 estimated SiW trigger inefficiencies			
Beam energy (GeV)	SWSEG $\times 10^{-5}$	SWHILO $\times 10^{-5}$	Total $\times 10^{-5}$
43.57	0.10 ± 1.18 ± 0.01	36 ± 2.0 ± 1.3	0.014 ± 0.37 ± 0.005
44.57	0.07 ± 1.18 ± 0.01	19 ± 1.4 ± 0.8	0.010 ± 0.37 ± 0.004
45.57	0.05 ± 1.18 ± 0.01	10 ± 1.1 ± 0.6	0.007 ± 0.37 ± 0.003
46.57	0.04 ± 1.18 ± 0.01	5 ± 0.9 ± 0.4	0.005 ± 0.37 ± 0.002
47.57	0.03 ± 1.18 ± 0.01	3 ± 0.8 ± 0.3	0.004 ± 0.37 ± 0.002

Table 15: Table of estimated trigger inefficiencies for SwitA events for an energy range twice as broad as the scan, in 1993 and 1995, and at the peak energy in 1994. The first error gives the uncertainty due to the limited statistics of the OPAL forward detector sample used to check for catastrophic SiW trigger system failures. The second error covers the uncertainty in convoluting the tails of the trigger response distribution over the energy spectrum of fiducial Bhabhas.

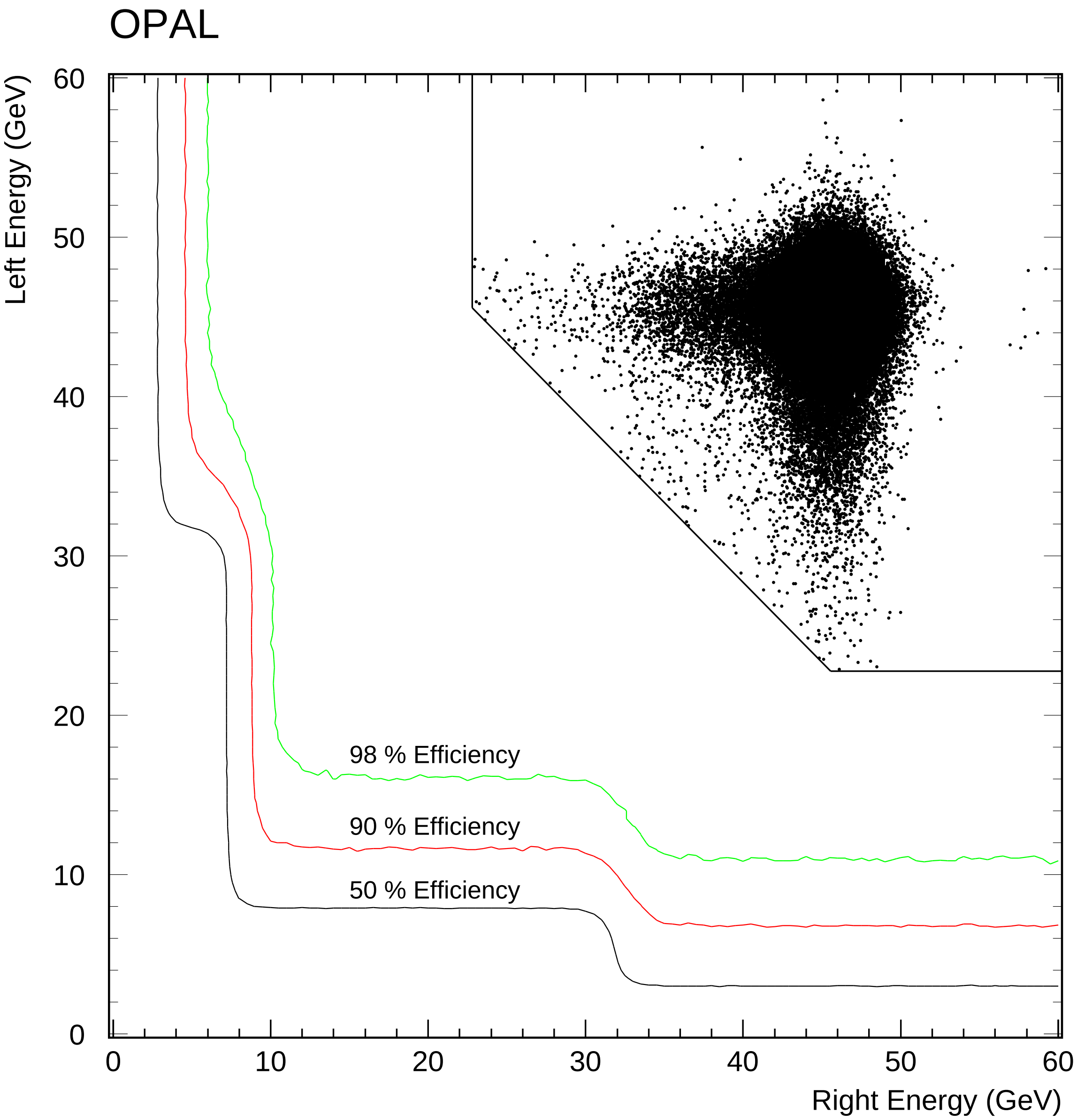

Figure 26: Left versus right summed energy for 10^5 SwitA selected events in 1994 with calculated 50, 90, and 98 % efficiency contours for the combined SWSEG, SWHILO trigger signals for the threshold settings. The straight lines indicate the energy cuts imposed in selecting the SwitA sample.

the offset and tilt of the beams with respect to the calorimeter bores, as well as the angular divergence of the beams and the physical size of the intersection region. Measurements of the above beam parameters, many of them determined fill-by-fill, enter the Monte-Carlo simulation of the detector described in section 8, and result in acceptance corrections of typically 3×10^{-4}, which we know with a precision of about 1×10^{-4}. The two most significant acceptance corrections come from the transverse beam offsets and the angular beam divergence.

The principle systematic errors in these corrections are due to discrepancy between the beam divergence measured from the acollinearity of SiW Bhabhas and that expected from accelerator parameters, as well as a conservative allowance for rapid variations in the tilt of the beam axis, which can only be roughly constrained by our measurements.

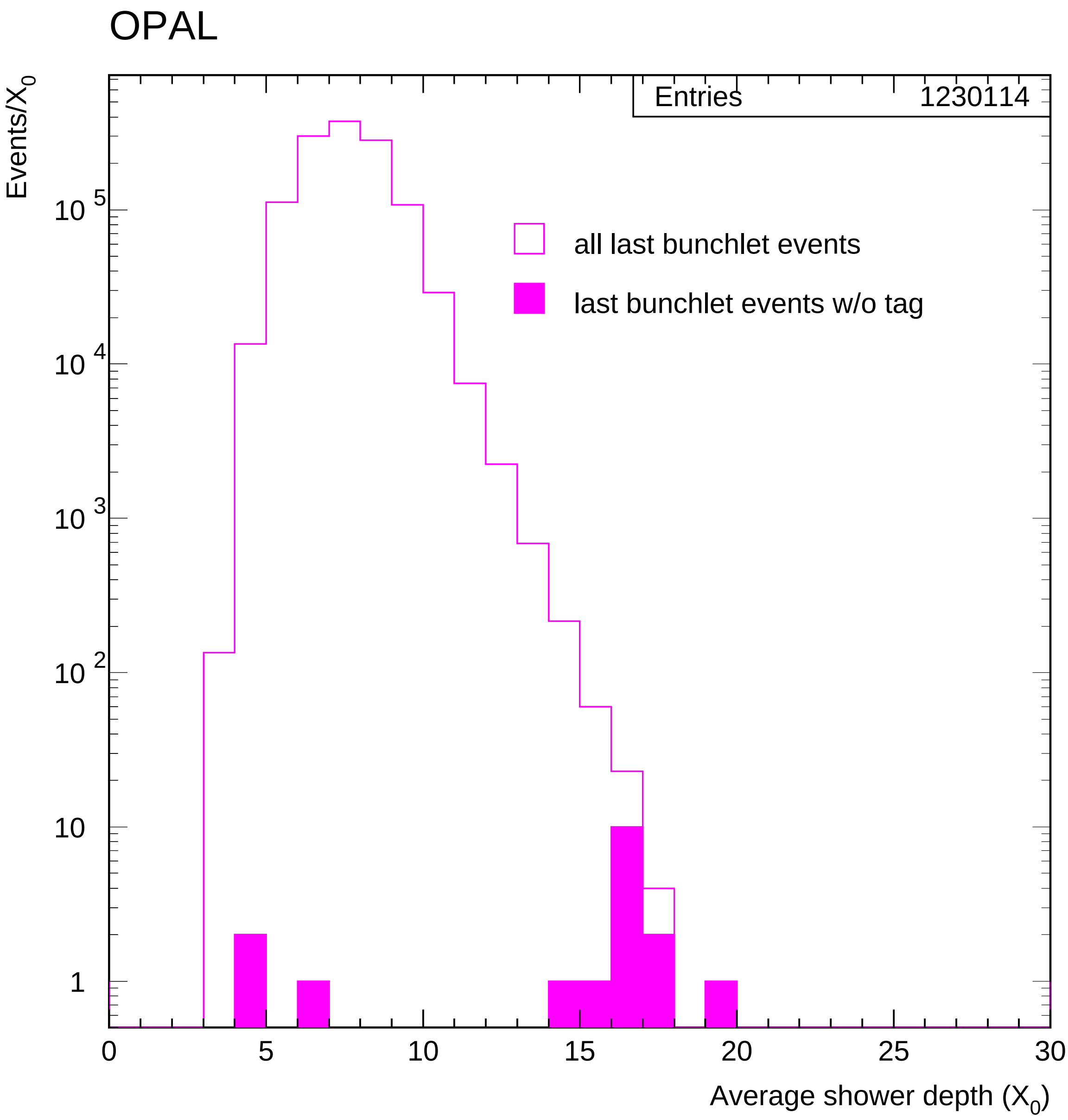

Figure 27: The efficiency of the SiW wagon tagger as measured on the last bunchlet, where hold is always issued, independent of any tag. For the sample of accepted Bhabha events held on the last bunchlet, the average shower depth parameter is plotted for all showers (open) and showers lacking a tag (shaded). Showers with anomalous development profiles, either deeper or shallower than the wagon tagger layers, are seen to be the dominant cause of tagger inefficiency.

The offset and tilts of the LEP beams, as well as the beam divergence, all modulate or smear the $1/\theta^3$ Bhabha spectrum leading to a net increase in acceptance. It is convenient to sort the effects of the beam parameters into the two categories of (i) beam offsets and tilts and (ii) beam size and divergence, as they affect the acceptance in slightly different ways. In practice the separation can not be made absolutely and some effects of rapid variations in beam offsets and tilts are included in the beam size and divergence category. We first consider the effects of transverse beam offsets (section 7.1) and then longitudinal offsets (section 7.2). Finally, we consider the effects of beam size and divergence (section 7.3).

7.1 Transverse beam offsets and tilts

Beam offsets transverse to the beam axis produce a first order modulation in the SwitR and SwitL acceptances as a function of the azimuthal angle. After integrating over all azimuth, a second-order correction remains. The importance of this correction can be seen by considering the effect of a beam offset or tilt on the acceptance of a single side of the calorimeter due to the *definition* cuts. An analytical calculation assuming a $1/\theta^3$ differential distribution gives an azimuthal modulation of the luminosity of

$$\frac{\mathrm{d}L_{\mathrm{RL}}}{\mathrm{d}\phi} \propto 1 + \frac{8}{3}\frac{\epsilon}{r_1}\frac{1-\left(\frac{r_1}{r_2}\right)^3}{1-\left(\frac{r_1}{r_2}\right)^2}\cos\left(\phi-\phi_\epsilon\right) + \left(\frac{\epsilon}{r_1}\right)^2\frac{1-\left(\frac{r_1}{r_2}\right)^4}{1-\left(\frac{r_1}{r_2}\right)^2}\left(6\cos^2\left(\phi-\phi_\epsilon\right)-1\right) \tag{38}$$

where r_1 and r_2 are the inner and outer radii of the acceptance and ϵ is the magnitude of the eccentricity which corresponds to the offset of the outgoing beam at the reference plane of the calorimeter. The x and y components of the eccentricity are given by

$$\begin{aligned} \epsilon_x &= \epsilon\cos\phi_\epsilon \\ \epsilon_y &= \epsilon\sin\phi_\epsilon\ . \end{aligned}$$

The amplitude of a typical first-order azimuthal Bhabha intensity modulation is $\sim 5\%$, but only the much smaller second-order term contributes to the average over azimuthal angle. We are therefore in the favorable situation of being able to use a sizeable first-order effect to determine a small second-order correction. The increase in acceptance of the SwitR or SwitL selection due to the eccentricity can be obtained from equation 38 and is given by

$$\frac{\Delta A_{\mathrm{RL}}}{A_{\mathrm{RL}}} \approx +\left(\frac{\epsilon}{1.5\ \mathrm{mm}}\right)^2 \times 10^{-3}, \tag{39}$$

where ϵ is the magnitude of the eccentricity of the beam on the relevant side. Typical values of the eccentricity of the LEP beam in the OPAL interaction region are 1 to 2 mm, making this a significant effect. However, the effect of the eccentricities on the SwitR and SwitL selections is reduced by more than 50% when the *isolation* cuts are considered. The reduction is due to the loss of radiative events whose detector centered value of acollinearity or acoplanarity is increased by the eccentricities.

One of the concepts motivating the SwitA luminosity selection is the reduction of acceptance dependence on the position of the beam spot. If the true Cartesian half-difference between the shower impact points in the two calorimeters is used in determining the acceptance for back-to-back Bhabhas, then the acceptance is effectively defined in the beam-centered frame, and is therefore independent of any beam offset. In determining SwitA, however, we actually approximate the Cartesian coordinate half-difference by forming the average radius in polar coordinates, calculating

$$R_A = \frac{1}{2}(R_R + R_L) \tag{40}$$

which differs from the exact Cartesian expression

$$R_A = \sqrt{\left(\frac{x_R - x_L}{2}\right)^2 + \left(\frac{y_R - y_L}{2}\right)^2} \tag{41}$$

by a small second-order term in the beam offset. An analytic calculation of the resulting azimuthal modulation of the SwitA luminosity, similar to the calculation made for SwitR and SwitL in equation 38, considering only the effect of the definition cuts, gives

$$\frac{\mathrm{d}L_{\mathrm{A}}}{\mathrm{d}\phi} \propto 1 + \left(\frac{\epsilon}{r_1}\right)^2\frac{1-\left(\frac{r_1}{r_2}\right)^4}{1-\left(\frac{r_1}{r_2}\right)^2}\sin^2\left(\phi-\phi_\epsilon\right) \tag{42}$$

where ϵ is here the average eccentricity of the beams in the two calorimeters, equal to the transverse offset of the beamspot. Considering the definition cuts alone, there is no first-order azimuthal modulation of the acceptance, and the second-order increase in total acceptance is $\frac{5}{16}$ as large as the corresponding increase for SwitR and SwitL. The effect of the isolation cuts, however, is similar, and therefore SwitA suffers a net *decrease* in acceptance about half the size of the net increase suffered by SwitR and SwitL.

Beam tilts with respect to the calorimeters result in different right and left eccentricities. Thus, it is necessary to determine the x and y components of the eccentricities associated with the SwitR selection $(\epsilon_{\mathrm{x}R}, \epsilon_{\mathrm{y}R})$ and the SwitL selection $(\epsilon_{\mathrm{x}L}, \epsilon_{\mathrm{y}L})$ separately. The acceptance of the SwitR and SwitL definition cuts will be independent of the eccentricity on the opposite side, while the acceptance of the isolation cuts depends on the values of the eccentricities on both sides of the detector. The SwitA acceptance shares a similar dependence on the isolation cuts due to beam tilts, and also picks up a second-order increase in acceptance through the definition cut.

In order to calculate the effect of the mean beam offset and tilt, these quantities are first determined from the resulting azimuthal modulation of the Bhabha rate for each OPAL run.[10] The average of the eccentricities gives the beam offset, i.e,

$$x_{\mathrm{off}} = \tfrac{1}{2}(\epsilon_{\mathrm{x}R} + \epsilon_{\mathrm{x}L}) \quad y_{\mathrm{off}} = \tfrac{1}{2}(\epsilon_{\mathrm{y}R} + \epsilon_{\mathrm{y}L})$$

The beam tilt is defined as the difference of the left and right eccentricities, i.e,

$$x_{\mathrm{tilt}} = \tfrac{1}{2}(\epsilon_{\mathrm{xR}} - \epsilon_{\mathrm{xL}}) \quad y_{\mathrm{tilt}} = \tfrac{1}{2}(\epsilon_{\mathrm{yR}} - \epsilon_{\mathrm{yL}})$$

As with any second-order correction a lack of precision in determing the offsets will result in a net bias in the calculated corrections. Due to the limited statistical precision of the offsets determined from the eccentricities ($\sim 250\,\mu$m/run), a second method is used to monitor the beam offset at the interaction point. This method uses the radial and azimuthal coordinates of Bhabha events with beam energy electrons in both calorimeters. These events will have little or no initial state radiation and the line joining each such pair of back-to-back showers therefore passes through the beam spot. For each OPAL run we determine the average beam spot position by fitting for the point which minimizes the distances of closest approach over the ensemble of such lines.

The resolution of this method is illustrated by the apparent acollinearity or acoplanarity observed in such non-radiative events in the *detector frame.* A single event measures two of the three spatial coordinates of the interaction region with a resolution limited only by the inherent position resolution of the detectors, the angular divergence of the beams, and, of course, the size of the luminous region itself. A plot of $\Delta R = (R_{\mathrm{R}} - R_{\mathrm{L}})$ versus ϕ_{R} for an entire run, as shown in figure 28, allows the beam spot to be determined in three dimensions, and with greatly enhanced statistical precision. The cos and sin amplitudes of the azimuthal modulation give the $x-$ and $y-$components, while the constant offset gives the the $z-$component. Similarly, a plot of $R\Delta\phi$ versus ϕ_{R}, also shown in figure 28, reveals the $x-$ and $y-$components of the mean beam spot, with a 90° phase shift, while the constant offset of about 0.6 mm yields no additional beam spot position information, but agrees with the offset expected from the curvature of the Bhabha tracks in the OPAL magnetic field. The RMS width of the scatter about the mean sinusoids in these plots is about 0.9 mm, dominated by two essentially equal components, one from the inherent resolution of the detector and the other from the angular divergence of the beams. The apparent structure in the $R\Delta\phi$ versus ϕ_{R} plot is due to the strong variation of the ϕ resolution across each pad. The statistical precision of this method is high; the beam spots are determined with an accuracy of better than 10 μm for all but a few runs.

In order to calculate the acceptance corrections due to beam offsets and tilts, the measured run-by-run distributions of offsets and tilts for a given period are used as input to the detector simulation, as described in section 8. Because the offsets are determined from the fitting procedure described

---

[10] An OPAL run typically corresponds to one LEP fill. In the data considered here, the average number of accepted Bhabha events in an OPAL run was approximately 25,000.

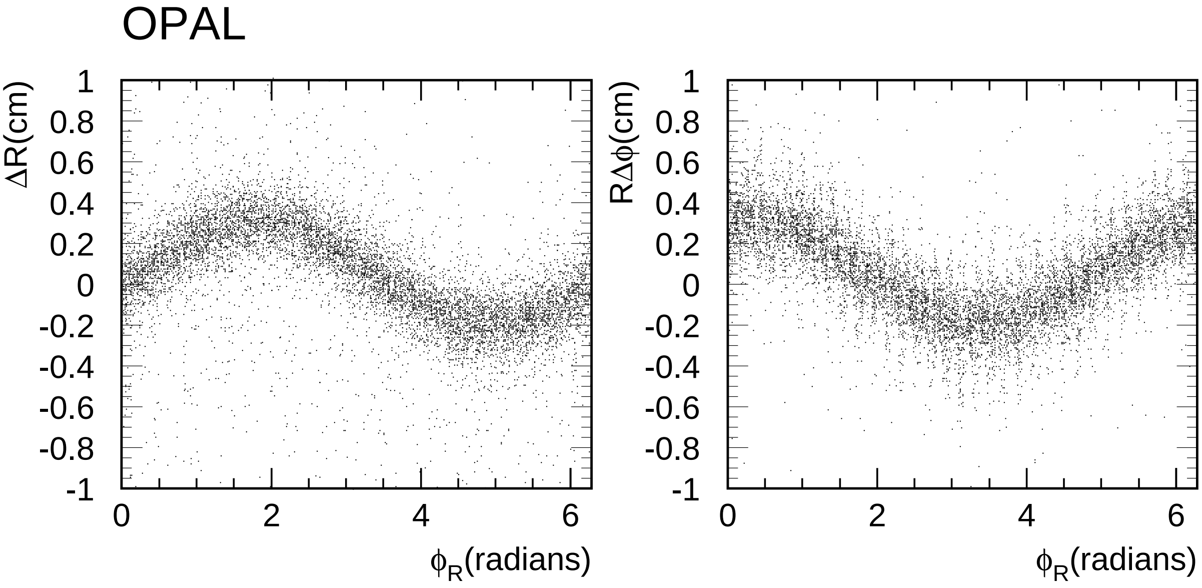

Figure 28: The beam spot position can be determined with great precision from the measured coordinates of back-to-back Bhabha clusters. The plot on the left shows the acollinearity of non-radiative Bhabhas in the detector frame as a function of $\phi_{\rm R}$. The plot on the right shows R times acoplanarity for the same sample.

above, they do not suffer any bias from the isolation cuts or any significant error from finite statistical errors.

The beam spot determined through shower coordiates agrees well with the spot determined through Bhabha intensity modulation, taken as the average of the right and left eccentricites. The coordinate method, however, yields no information on the tilt of the beam, which we continue to extract from the difference of the right and left eccentricites. The statistical precision of $\sim 250\mu$m on the measured tilt in a typical run is adequate to limit the non-linear bias in the acceptance correction to a manageable 3×10^{-5}, but it is not possible to usefully probe the tilts on time scales shorter than an individual run of approximately 10 hours. Rapid variations of the tilts could produce a correction to the acceptance which is not monitored through the azimuthal intensity modulation.[11] Because the typical beam offsets of 1–2 mm are appreciably larger than than the typical tilts of $\sim 300\,\mu$m for the data analyzed here, the main effect of these variations would be to increase either the SwitR or SwitL selection at the expense of the other, resulting in no change to the measured luminosity. However, a small additional correction of order

$$\frac{\Delta A_{\rm RL}}{A_{\rm RL}} \approx + \left(\frac{\Delta\epsilon_{\rm rms}}{1.5\ {\rm mm}}\right)^2 \times 10^{-3} \tag{43}$$

will remain due to the quadratic dependence of the acceptance on the eccentricity (see equation 39). Studies of the data from the LEP beam orbit monitors show no evidence for rapid motion of the beams, and such movements can be safely assumed to be smaller than the average tilts given by equation 38. The acceptance correction for a typical tilt of $\epsilon = 300\mu$m would be 0.4×10^{-4}. It is possible that the isolation cuts introduce a correction of opposite sign. To evaluate this effect, the change in the $L_{\rm RL}$ average was measured in the Monte Carlo with and without simulated tilts. For the 1994b sample,

---

[11] Note that random variations in the angles of the electron and positron beams will appear as additional contributions to the beam divergence which is evaluated at the end of this section. In order for the tilts to have an effect on the acceptance which is not included in the divergence correction, the trajectories of the incoming positron and electron beams must change in a correlated manner.

which has a typical tilt and offset, turning on the tilt gave an acceptance change of $+0.4\pm0.3\times10^{-4}$, in agreement with the estimate from equation 43. We take 100% of this effect as the possible systematic error from variations of the tilt within a run.

7.2 Longitudinal offsets

Since the luminosity is calculated from the average of SwitR and SwitL, offsets in the position of the interaction region along the beam direction almost cancel in the average. Possible second order effects are taken into account by including the measured longitudinal beam offset in the detector simulation. In order to check the expected effects of the longitudinal beam position on the acceptance of the SwitR and SwitL selections, we plot

$$D_{\mathrm{LR}} = \frac{(N_{\mathrm{SwitL}} - N_{\mathrm{SwitR}})}{\frac{1}{2}(N_{\mathrm{SwitL}} + N_{\mathrm{SwitR}})}$$

for the nine data samples and compare it with analytical and Monte Carlo expectations. In figure 29 it can be seen that D_{LR} depends linearly on the z-offset with the expected slope. The scatter of the data with respect to a straight line is due to beam tilts, which also effect D_{LR}. These tilts have been included in the detector simulation and there is reasonable agreement between the data and Monte Carlo prediction for D_{LR}, with a χ^2/d.o.f of 15/9 (C.L. = 0.09). However, perfect agreement between the detector simulation and the data is not expected, because the detector simulation does not include correlations between the longitudinal beam position and changes in the tilts. These correlations will affect the D_{LR} ratio, but will not change the measured luminosity.

7.3 Beam size and divergence

Random movements of the colliding beams on a short time scale, as well as the finite beam sizes and divergences at the OPAL interaction region, cannot be monitored using the measured eccentricities. The largest of these effects is the beam divergence which affects the acceptance in the same way as the radial resolution, i.e.,

$$\frac{\Delta A}{A} \approx + \left(\frac{\sigma_\theta}{450\ \mu\mathrm{rad}}\right)^2 \times 10^{-3} \tag{44}$$

giving a correction to the luminosity of approximately 1×10^{-4} for the typical LEP beam divergence of 150μrad. The effects of finite beam size have a slightly different effect on the luminosity, and give rise to a slightly smaller correction. The most visible effect of the beam size and divergence is to broaden the acollinearity distribution. In the following, we compare the beam divergences extracted from the acollinearity distribution with those predicted from the LEP machine optics and measured beam size. The difference between these estimates is then used to evaluate the systematic error on the divergence.

By using measurements of the longitudinal and transverse size of the luminous region from the OPAL central detector and micro-vertex detector, it is possible to derive a number of constraints on the beam size and divergence. Tracks from the process $\mathrm{Z}^0 \to \mu^+\mu^-$ were used to determine the horizontal size of the luminous region, σ_x. The beam divergence in the horizontal plane is related to the horizontal size of the luminous region by

$$\sigma'_x = \sqrt{2}\frac{\sigma_x}{\beta^*_x}$$

where β^*_x is the β function at the interaction region and the factor $\sqrt{2}$ accounts for the difference between the beam size and the size of the luminous region. The horizontal beam divergence determined from this method is given in table 16. (Note that for period 1994c the microvertex detector was not installed and an adequately precise value of the horizontal beam size is not available.)

The horizontal beam divergence may also be estimated by comparing the acollinarity distribution of Bhabha events in the luminometer, corrected for the beam offset, with that of simulated events. The

Sample	σ'_x (a) (from acollinearity)	σ'_x (b) (from beam spot)
93 -2	$110 \pm 15\,\mu$rad	$90 \pm 10\,\mu$rad
93 pk	$110 \pm 15\,\mu$rad	$90 \pm 10\,\mu$rad
93 $+2$	$100 \pm 15\,\mu$rad	$90 \pm 10\,\mu$rad
94 a	$120 \pm 15\,\mu$rad	$85 \pm 10\,\mu$rad
94 b	$110 \pm 15\,\mu$rad	$85 \pm 10\,\mu$rad
95 -2	$145 \pm 15\,\mu$rad	$80 \pm 10\,\mu$rad
95 pk	$135 \pm 15\,\mu$rad	$80 \pm 10\,\mu$rad
95 $+2$	$155 \pm 15\,\mu$rad	$80 \pm 10\,\mu$rad

Table 16: Values of the horizontal beam divergence, σ'_x, as determined from (a) the acollinearity distribution and (b) the horizontal beam size as measured by the OPAL central detector. The discrepancy between the two values is used as the basis for the systematic error due to the uncertainty in the beam divergence. If this discrepancy is due to random changes in the directions of the incoming beams during runs, then using beam divergence as determined from the acollinearity will give the correct acceptance.

simulated events incorporated the radial detector resolution, as measured in the test beam, and the measured longitudinal size of the luminous region, as measured by muon pairs. To reduce the tails in the acollinearity distribution from radiative events, the events were required to satisfy $\mathrm{E} > 0.9 \cdot \mathrm{E}_{\mathrm{beam}}$ on both sides of the detector. Comparing the width of the acollinearity distribution of Bhabha events in the horizontal plane with simulated events we obtain the values given in table 16. The values of the beam divergence estimated from the Bhabha acollinearity distribution are systematically larger than those inferred from the size of the luminous region and the expected value for β. This effect is especially pronounced for the 1995 data. These differences may be due to an incorrect estimate of the value of β^*_x. However, a more likely explanation is that they are due to random changes in the angles of the incoming beams over time. These changes would be expected to be larger for the 1995 bunch train running. In the following, we use the value of divergence estimated from the acollinearity distribution and take 100% of the difference, in quadrature, between the two methods as a systematic error. This gives a $\sim 100\ \mu$rad uncertainty for 1993 and 1994 and 110 to 125 μrad for 1995. These results are summarized in table 16.

In the vertical plane, the beam size is much smaller, ($\sim 5\ \mu$m) and is not easily measured with tracks from the central detector and microvertex detector. For the effective beam size in the vertical direction we take 25 μm which includes typical motions of the beam in the vertical plane over the course of a run.

The beam divergence in the vertical plane can not be directly determined from measurements of the central detector alone. For the nominal LEP optics the vertical and horizontal divergences are equal, but in practice the vertical divergence is expected to be somewhat larger than the horizontal divergence. Values of σ'_y between 125 μrad and 185 μrad are obtained for the nine data samples by using Bhahba events in the vertical plane and comparing their acollinearity with that of simulated events. These values, which are used in calculating the acceptance for each period, are given in table 17.

The effects of the finite beam size and beam divergence have been incorporated into the simulation used to extract the final acceptance. To estimate the systematic error due to uncertainties in these beam parameters equation 44 is used. The largest single effect is from the beam divergence. The uncertainty in the divergences is parameterized by a term of $\pm 100\mu$rad which adds in quadrature to the divergence. The resulting systematic error on the luminosity is 0.4×10^{-4}. Since this uncertainty could be fully correlated, or fully uncorrelated between the samples, we conservatively assume both a correlated and uncorrelated error of 0.4×10^{-4}. The uncorrelated error allows for different systematic effects at the three energy points of each scan. We also allow for a systematic difference between the 1993-1994 and 1995 running which reflects the increase in the difference between the measured and calculated divergence for the 1995 run. The systematic error from uncertainties on the values of the transverse beam size and radial resolution is negligible. These effects are summarized in table 18.

The effect of the finite longitudinal beam size on the luminosity measurement differs slightly from that of the transverse size. Assuming a $1/\theta^3$ distribution, it can be parameterized as

$$\frac{\Delta A}{A} \approx + \left(\frac{\sigma_z}{8.0 \text{ cm}}\right)^2 \times 10^{-3}. \tag{45}$$

The longitudinal beam size, σ_z , averaged over the 1993, 1994 and 1995 running, is known to better than 0.02 cm, giving negligible systematic error.[12]

Sample	σ_x	σ_y	σ_z	σ'_x	σ'_y
93 -2	156 μm	25 μm	0.70 cm	110 μrad	140 μrad
93 pk	156 μm	25 μm	0.70 cm	110 μrad	140 μrad
93 $+2$	140 μm	25 μm	0.70 cm	100 μrad	125 μrad
94 a	120 μm	25 μm	0.70 cm	120 μrad	155 μrad
94 b	120 μm	25 μm	0.70 cm	110 μrad	150 μrad
94 c	150 μm	25 μm	0.70 cm	135 μrad	185 μrad
95 -2	140 μm	25 μm	0.70 cm	145 μrad	170 μrad
95 pk	140 μm	25 μm	0.70 cm	135 μrad	165 μrad
95 $+2$	140 μm	25 μm	0.70 cm	155 μrad	180 μrad

Table 17: Values of the beam parameters used in the detector simulation. The dimensions of the luminous region, σ_x, σ_y and σ_z, include the estimated rms motion of the beam offsets over the course of a typical run.

Effect	Systematic error (correlated) $\times 10^{-4}$	Systematic error (uncorrelated) $\times 10^{-4}$	Additional error (1995 only) $\times 10^{-4}$
beam divergence	0.40	0.40	0.50
transverse beam offsets	0.01	0.01	< 0.01
average beam tilts	0.01	0.01	< 0.01
variation in beam tilts	0.40	0.40	< 0.01
longitudinal beam size	0.02	0.02	< 0.01
transverse beam size	< 0.01	< 0.01	0.20
Total	0.57	0.57	0.50

Table 18: Systematic errors from incomplete knowledge of the LEP beam parameters.

7.4 Beam energy error and spread

The errors in the luminometer acceptance due to the uncertainty of the LEP energy at each energy point [?] are not included in the OPAL luminosity analysis. These highly correlated uncertainties of

---

[12] Large, $\sim 30\%$, variation in the longitudinal beam size within a run can occur due to the use of wigglers to limit the beam-beam interactions. However, the average behavior in each of the nine samples was nearly the same.

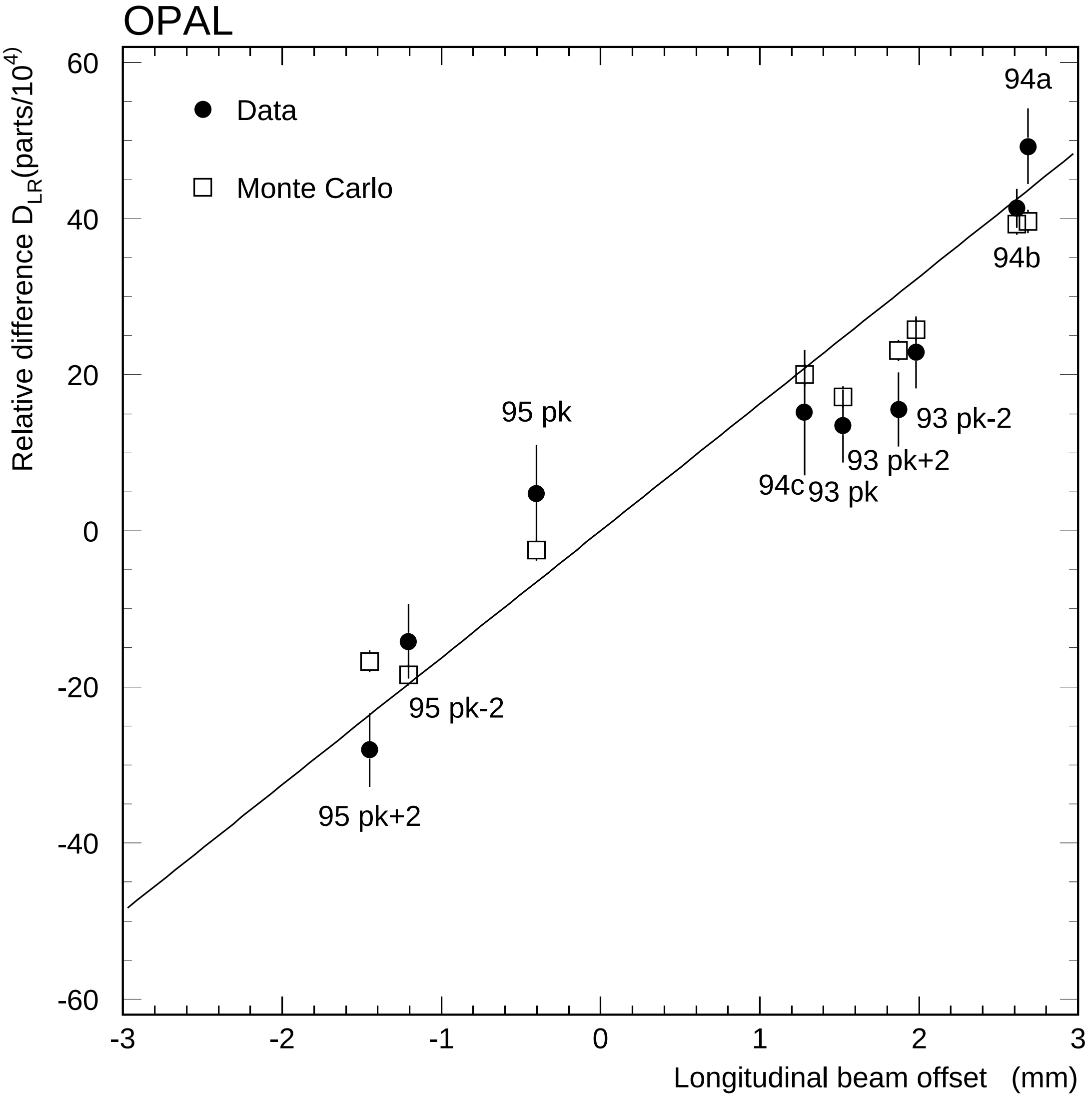

Figure 29: D_{LR}, the difference between SwitL and SwitR selections, divided by their average, as a function of the mean measured longitudinal offset of the beam spot. The points show the value for each of the nine data taking periods for both the data, and the detector simulation. The detector simulation uses the reconstructed longitudinal beam position and the transverse offsets and tilts as inputs. The solid line shows the expected ratio if there were no effects from energy resolution and from differences in the eccentricities of beam in the left and right calorimeter.

order 10^{-4} are, however, taken into account when fitting for the Z^0 resonance parameters. In propagating the LEP energy uncertainties to the measured cross sections, the derivative of the luminosity with respect to energy plays a small role compared to the derivatives of the cross sections themselves, and ultimately has a negligible effect on the final Z^0 parameters and errors.

The rms spread of the LEP central energy of about 55 MeV generates a correction of $\sim 10^{-3}$ to the OPAL peak cross sections due to the curvature of the Z^0 lineshape. The off–peak corrections are substantially less. The corresponding correction to the luminosity is everywhere 2×10^{-6}, and is neglected.

8 Detector simulation

The OPAL SiW detector simulation does not rely on a detailed physical simulation of electromagnetic showers in the detector. Instead, we utilize the experimentally determined response of the detector in energy, radius and azimuth to generate the measured quantities corresponding to the clusters of section 3 directly from the four-vectors of the physics Monte Carlo. This approach gives a much more reliable description of the tails of the detector response functions, which are primarily due to extreme fluctuations in shower development, than we could obtain using any existing code which attempts to simulate the basic interactions of photons and electrons in matter. We also choose to simulate an *ideal* detector, which differs from the actual detector in having nominal dimensions, a perfectly efficient trigger and wagon tagger, as well as being free of accidental coincidence (although not overlap) backgrounds. We treat the differences between this ideal detector and the actual detector by applying what we term *external* corrections (see section 9).

The simulation consists of five steps. First, the four-vectors are used to generate particle trajectories according to the beam parameters. Second, the energy of each of the four-vectors is smeared by an energy resolution algorithm, producing "showers". Third, background (as measured from random beam crossings) is added. Fourth, showers are grouped together, to produce the equivalent of the clusters (see section 3). Fifth, radial and azimuthal resolutions are simulated. In the following, these steps are described in somewhat more detail.

The beam spot offset for each event is chosen randomly from the distribution of measured x, y and z run-averaged beam spot positions. This run-averaged beam spot is further smeared by the measured beam sizes averaged over a given data sample (see section 7). Each event is then randomly boosted and rotated so as to simulate the effects of finite beam divergence while keeping the center-of-mass energy of each event fixed at its generated value.

Each of the rotated and boosted four-vectors is then extrapolated to the detector. The energy of each four-vector is smeared using the parameterization described in section 4.3.

Accidental overlap background is taken from a library based on random beam crossings. Separate libraries are available for 1993, 1994 and 1995 runs to reflect different background conditions. Systematic errors from these effects were evaluated in section 5.

At the next step, showers are merged into at most three clusters per side which closely approximate those found in the data. The clusters are sorted according to energy and any clusters outside of the detector (that is, clusters with radii outside 6.20 and 14.20 cm) are discarded. (The relatively tight isolation cuts of the selections ensure that the calculated acceptance is insensitive to the treatment of showers close to the edge of the detector.) The most energetic remaining shower is chosen as the shower core. If any other remaining shower is within the measured two-cluster separation of the main shower core in azimuth and radius, it is merged with the shower core. The probability to merge two showers has been parameterized by using the data: the actual pad signals from showers due to photons in events with final state radiation were overlaid at variable positions on the signals from the electron showers, and the resulting cluster merging probabilities were measured (see section 3) as a function of shower separation. The merging probability reaches 50% at a separation of 1.0 cm, or 4 pad widths. When two showers are merged, their energies are summed, and the radial position of the most energetic cluster is used unless the radial position of the two four-vectors fall within a window, in which case the position is taken as the energy weighted mean of both clusters. The scale of this window is set by the three pads used in the radial position algorithm and varies as a function of energy from two pad widths (0.5 cm) at beam energy to four pad widths (1.0 cm) at low energies. Studies were made varying the size of the window used for forming clusters, resulting in changes in acceptance below the assigned systematic error of 1×10^{-4}.

In the case of closely spaced, but resolvable clusters, no attempt has been made to simulate possible distortions in the energy assignment made by the cluster finding algorithm. This introduces a negligible correction to the luminosity acceptance because the energy cut is based on the sum of energy in the fiducial region of the detector. It may, however, affect the comparison of final state radiative events in the data and Monte Carlo.

The radial and azimuthal positions of the remaining clusters are further smeared using resolution measurements from the test beam and from the data. The radial and azimuthal response functions are taken as Gaussians whose mean values reproduce the input four-vectors and whose resolutions are assumed to scale as $1/\sqrt{E}$, where E is the cluster energy. The detector simulation allows the evolution of resolution with energy to be changed to assess the systematic errors due to these aspects of the detector response. The test beam measurement is used to set the radial resolution of 130μm at pad boundaries in the clean acceptance near the inner edge of the detector for beam energy electrons and positrons. The effects of the increased material at greater radii are estimated from changes in the acollinearity and acoplanarity distributions as a function of radius which are not accounted for by the known beam sizes and divergences. These studies indicate that the apparent resolution at the outer edge and in the central portion of the detector, behind the bulk of the pre–showering material, is degraded by a factor of 2 to 2.5.

The effect of this degradation in resolution is especially important for the acceptance of the acollinearity cut, since in many of the events having an acollinearity near 2.5 cm, one of the electrons will have an energy significantly less than E_{beam}, and lie in a region of the detector where the effects of the pre–showering material are most severe. Because the apparent degradation in radial resolution could be partially caused by an underestimate in the length of the beamspot, we assign the full calculated effect of this degradation as an uncertainty of 2×10^{-5} in the acceptance due to uncertainties in the radial resolution. Similarly, the radial coordinate of such lower–energy electrons in the region behind the bulk of the pre–showering material may develop a net bias which we estimate could be as large as $15\,\mu$m. According to equation 18 we therefore assign a systematic error of 3.6×10^{-5} due to possible bias in the measured acollinearity.

The azimuthal resolution is taken as $1/\sqrt{2}$ times the width of the beam–centered acoplanarity distribution of full–energy Bhabhas, and varies from 10–12 mrad as a function of radius. An acceptance uncertainty of 4×10^{-6}, equal to 10% of the resolution flow calculated according to equation 35, accounts for the non–Gaussian features of the actual detector resolution, which are not reproduced by the detector simulation.

The final clusters include values of E, R, and ϕ and are passed through the same analysis chain as the data.

9 Calculation of the acceptance

We are now in position to calculate the critical parameters mentioned in section 1.3, the acceptances for the SwitX luminosity selections, A_{RL} and A_{A}. We proceed to make the calculation in four steps:

- We use the best available Monte-Carlo simulation of small–angle Bhabha scattering (BHLUMI) to calculate, at the level of the generated four–vectors, a *theoretical reference acceptance* ($A^{\mathrm{ref}}_{\mathrm{RL}}$) which is very close to the actual experimental acceptance. We make this calculation at a single reference energy of 91.100 GeV, and generate a very large sample of events to reduce the statistical error on this absolute accepted cross section to a level well below any of our other errors.

- We use another Monte-Carlo (BHAGEN), and an analytic calculation (ALIBABA), to calculate the energy evolution of the acceptance through the small relevant range of energies about the Z^0. At this point we also consider the contribution of the processes $\mathrm{e}^+\mathrm{e}^- \to \gamma\gamma$ and $\mathrm{e}^+\mathrm{e}^- \to \mathrm{e}^+\mathrm{e}^- X$. After applying these corrections ($\epsilon_{\mathrm{theory}}$) we arrive at the *ideal theoretical acceptance.*

- We pass a more limited sample of four–vectors from the BHLUMI Monte-Carlo through our parametrized detector response simulation described in section 8 to calculate the small binomial differences (ϵ_{sim}) between the ideal theoretical acceptance and the *ideal experimental acceptance.*

- Finally, we apply the *external* corrections (ϵ_{ext}) to convert the ideal experimental acceptance into the *actual experimental acceptance*, accounting for the small departures of the actual detector from its nominal geometry revealed by the metrology and coordinate anchoring studies. The external corrections also account for any trigger and wagon tagger inefficiencies, as well as accidental coincidences from beam–related backgrounds.

The final actual luminometer acceptance, A_{RL}, is therefore calculated as:

$$A_{\mathrm{RL}} = A_{\mathrm{RL}}^{\mathrm{ref}}(1 + \epsilon_{\mathrm{theory}} + \epsilon_{\mathrm{sim}} + \epsilon_{\mathrm{ext}}). \tag{46}$$

The major advantage of the above organization is that our clear definition of an ideal theoretical acceptance at four–vector level allows our result to be easily adjusted to incorporate a potential improvement in the theoretical understanding of small–angle Bhabha scattering. Only a four–vector level calculation using an improved Bhabha Monte-Carlo needs to be undertaken. Our decision to calculate the energy dependence of the theoretical acceptance separately, rather than to use the full BHLUMI Monte-Carlo everywhere, is motivated solely by the desire to limit the relative acceptance errors, which would otherwise be larger due to the difficulty in running BHLUMI with sufficient statistics at a large number of energies. Tests have demonstrated that the energy dependence of BHAGEN and ALIBABA agrees with that of BHLUMI within the quoted errors, as demonstrated by the direct BHLUMI 4.04 points plotted in figure 30.

9.1 The theoretical reference acceptance

This section describes the calculation of the theoretical reference cross section, which is based only on four-vector quantities produced by the BHLUMI Monte Carlo.

At Born level, Bhabha scattering is described by equation 8 and results in the production of exclusively collinear, beam–energy, scattered electrons. Considering first–order radiative corrections in leading log allows photons collinear with either the in–coming or out–going electrons to be radiated. In sub–leading log, these photons can be acollinear. The consideration of progressively higher–order terms in the perturbative expansion allows correlations in multiple–photon emission to be taken into account. Exponentiation is a useful calculational technique which allows lower–order terms in the perturbative expansion to be used in approximating the effect of higher–order terms which have not been explicitly evaluated, and allows an $O(\alpha)$ generator to simulate final states with multiple photons. Higher–order vertex corrections also make themselves felt in modifying the cancelation of the infra–red divergences inherent in the external photonic corrections. The effect of vacuum polarization modifies the internal photonic propagators and introduces a dependence on hadronic couplings which is most accurately quantified through a dispersion relation to experimental measurements of $\mathrm{e}^+\mathrm{e}^- \rightarrow$ hadrons [?]. All these effects modify the Born–level acceptance of the luminometer by only a few percent.

The BHLUMI Monte Carlo program [?] is accepted as embodying the considerable theoretical work which has been undertaken to calculate small–angle Bhabha scattering in the LEP era. It is a multiphoton exponentiated $O(\alpha)$ generator for small–angle Bhabha scattering only. It includes the majority of the leading logarithmic and part of the next to leading logarithmic terms of $O(\alpha^2)$ for the Bhabha scattering process. The current version, BHLUMI 4.04, has an estimated precision [?, ?, ?] of 6.1×10^{-4} for use with the OPAL acceptance.

The parameters used in generating the theoretical reference cross section are given in table 19. The range of the allowed t-channel transfers correspond to an inner acceptance for non-radiative events of 18.9 mrad and an outer acceptance of 150 mrad. This range is sufficiently broad to cover nearly all radiative events which could trigger our detector. The fraction of small t-channel transfer events not generated by the Monte Carlo, but which would be accepted by the SwitR, SwitL or SwitA selections was determined to be less than 2×10^{-5} by varying the value of the minimum t-channel transfer. With the parameter set used, our BHLUMI calculation includes the effect of all γ exchange processes within the scope of the program, but specifically excludes the effects of $\mathrm{Z} - \gamma$ interference, which we consider separately.

Parameter	Value	BHLUMI variable
Center-of-mass energy ($\sqrt{s}$)	91.100 GeV	
Minimum t-channel transfer	0.741 GeV^2	
Maximum t-channel transfer	46.6 GeV^2	
Soft photon cutoff ($\epsilon = \frac{2E_\gamma}{\sqrt{s}}$)	1.0×10^{-4}	
Vacuum Polarization	Method 3 [?]	(KeyPia =3)
$\mathrm{Z} - \gamma$ interference	Off	(KeyZet =0)

Table 19: Parameters used with BHLUMI 4.04 Monte Carlo to obtain the reference cross section. Note that the $\mathrm{Z} - \gamma$ interference correction is kept separate so that it is not necessary to generate large statistics Monte Carlo samples at each beam energy.

The theoretical reference acceptance is defined in the Monte Carlo calculation by taking the energy in each detector as the sum of all four-vectors with polar angles between 27.227 mrad and 55.629 mrad. The energy in each calorimeter is required to be greater than $0.50E_{\mathrm{beam}}$, while the total energy is required to be greater than $0.75\sqrt{s}$, where E_{beam} is the nominal LEP beam energy and $\sqrt{s} = 2E_{\mathrm{beam}}$. The tight radial cuts of 7.7 cm and 12.7 cm, which are equivalent to polar angles of 31.288 mrad and 51.576 mrad, as well as the acoplanarity cut of 200 mrad, and an acollinearity cut of 10.162 mrad (which closely corresponds to 2.5 cm in radial difference), are imposed on the coordinates of the single most energetic "particle" in each detector.

An important feature of this ideal configuration is that it incorporates the distinction which is made in the experimental analysis between the particles used to calculate energy (the sum of the whole detector) and those used to calculate position. The definition of the most energetic four-vector may depend on the parameters of the Monte Carlo and the order of the calculation. For the results presented here we defined a "particle" by clustering together all four-vectors within $\sim$ 3 mrad of each other. In the BHLUMI 4.04 Monte Carlo this has almost no effect on the acceptance (less than 0.2 $\times 10^{-4}$). In reference [?] the impact of the definition of the "most energetic particle" on comparisons between different Monte Carlo generators was evaluated and no differences were observed for acceptances similar to the one described here.

The accepted theoretical reference cross sections for these L_{RL} and L_{A} selections were calculated to be

$$\begin{aligned} A^{\mathrm{ref}}_{\mathrm{RL}} &= 78.898 \pm 0.005 \text{ nb} \\ A^{\mathrm{ref}}_{\mathrm{A}} &= 79.413 \pm 0.005 \text{ nb} \end{aligned}$$

at $\sqrt{s} = 91.100$ GeV, where the error is statistical only. Note that these cross sections do not include the $\mathrm{Z} - \gamma$ interference, $\mathrm{e^+e^-} \to \gamma\gamma$, or the detector acceptance corrections given in table 23.

The acceptance obtained by simply integrating the Born cross section of equation 8 over the geometrical acceptance of the detector is 81.0298 nb, 2.7% larger than the BHLUMI 4.04 value. Vacuum polarization reduces the Born cross section by 4.1%, while other radiative corrections make a net positive contribution of 1.4%, most of which is due to the $O(\alpha)$ terms.

9.2 Theoretical acceptance corrections

In this section we describe adjustments made to the BHLUMI cross section for $\mathrm{Z} - \gamma$ interference, the running of the vacuum polarization as a function of t across the energies of the scan, and for the processes $\mathrm{e^+e^-} \to \gamma\gamma$ and $\mathrm{e^+e^-} \to \mathrm{e^+e^-}X$.

The energy dependence of the luminometer acceptance was calculated using the ALIBABA [?] and BHAGEN [?] calculations. Excluding the fundamental $1/s$ dependence of the Bhabha cross section leaves the effects of $\mathrm{Z} - \gamma$ interference and the variation in vacuum polarization across the relevant

	93 −2	93 pk	93 +2	94 a	94 b	94 c	95 −2	95	95 +2
93 −2	1.0	0.0	-1.0	0.0	0.0	0.0	1.0	0.0	-1.0
93 pk	0.0	1.0	0.0	1.0	1.0	1.0	0.0	1.0	0.0
93 +2	-1.0	0.0	1.0	0.0	0.0	0.0	-1.0	0.0	1.0
94 a	0.0	1.0	0.0	1.0	1.0	1.0	0.0	1.0	0.0
94 b	0.0	1.0	0.0	1.0	1.0	1.0	0.0	1.0	0.0
94 c	0.0	1.0	0.0	1.0	1.0	1.0	0.0	1.0	0.0
95 −2	1.0	0.0	-1.0	0.0	0.0	0.0	1.0	0.0	-1.0
95 pk	0.0	1.0	0.0	1.0	1.0	1.0	0.0	1.0	0.0
95 +2	-1.0	0.0	1.0	0.0	0.0	0.0	-1.0	0.0	1.0

Table 20: The correlation matrix for $\mathrm{Z}-\gamma$ interference and the change in vacuum polarization.

region of the scan. The correction factor, as shown in figure 30, is calculated as the ratio

$$\frac{\sigma_{\mathrm{bhagen}}(E)}{\sigma^{\mathrm{noZ^0}}_{\mathrm{bhagen}}(91.1\,\mathrm{GeV})}\left(\frac{91.1\,\mathrm{GeV}}{E}\right)^2 \tag{47}$$

where σ_{bhagen} is the full BHAGEN accepted cross section with values of the Z^0 mass and width taken to be 91.187 and 2.489 GeV [?], and $\sigma^{\mathrm{noZ^0}}_{\mathrm{bhagen}}$ is the BHAGEN cross section calculated with the effect of the Z^0 turned off. The precision of the interference correction calculated from the BHAGEN Monte Carlo has been estimated by comparison with the published results of ALIBABA [?] in the same acceptance. Both BHAGEN and ALIBABA include the complete $O(\alpha)$ and $O(\alpha^2)$ LL photonic corrections. The quoted physical precision of the ALIBABA $\mathrm{Z}-\gamma$ interference correction is 1.5×10^{-4}, essentially due to the lack of NLL $O(\alpha^2)$ terms. The absolute difference between the interference corrections of the two programs is below 6×10^{-5} over a wide range of center-of-mass energies. Around the peak the difference is consistent with zero within the statistical error, which is 2×10^{-5}. Taking into account the 1.5×10^{-4} uncertainty due to missing NLL $O(\alpha^2)$ terms in ALIBABA, we assign to BHAGEN a precision of 1.5×10^{-4} in the relative cross sections at the three points of the energy scan. The error matrix associated with this uncertainty is given in table 20.

Potential physics backgrounds from the processes $\mathrm{e^+e^-}\to\gamma\gamma$ and $\mathrm{e^+e^-}\to\mathrm{e^+e^-}X$ have also been considered. The correction for the former process, which our calorimetric measurement does not distinguish from $\mathrm{e^+e^-}\to\mathrm{e^+e^-}$, has been determined by using a radiative $\mathrm{e^+e^-}\to\gamma\gamma(\gamma)$ Monte Carlo generator [?] at four–vector level. The $\gamma\gamma$ cross section within our idealized acceptance is found to be (14.0 ± 0.2) pb at 91.1 GeV, or 1.8×10^{-4} times the Bhabha cross section in the same acceptance, with negligible uncertainty. A simple analytic calculation at Born level agrees within 10%

The contribution of soft pair production in the reaction $\mathrm{e^+e^-}\to\mathrm{e^+e^-}X(X=ee,\mu\mu,...)$, giving rise to final states in configurations which would be accepted by the luminosity Bhabha selection, has been calculated in our idealized acceptance according to reference [?]. Applying the calculated fractional contribution of $(-4.4\pm1.4)\times10^{-4}$ [?] as a correction to the BHLUMI reference cross section (which does not include such pairs) allows the BHLUMI 4.04 theoretical error of 6.1×10^{-4} to be reduced to 5.4×10^{-4} [?].

The corrections to the theoretical reference cross section, including $\mathrm{Z}-\gamma$ interference and physics backgrounds($\epsilon_{\mathrm{theory}}$), are illustrated in table 21. The particular energies chosen in table 21 correspond to the OPAL multihadron cross section sample. In order to determine the cross sections for leptonic and hadronic decays of the Z^0, the luminosity is counted separately for each channel. The center-of-mass energy for each channel is slightly different because of variations in detector status requirements (e.g. the muon chambers do not have to work to count electrons). These variations give the $\mathrm{Z}-\gamma$ and $1/s$ corrections a very small channel dependence.

Sample	Average E_{cm} GeV	$1/s$ correction $\times 10^{-4}$	$\mathrm{Z}-\gamma$ correction $\times 10^{-4}$	$\mathrm{e}^+\mathrm{e}^- \to \gamma\gamma$ background $\times 10^{-4}$	soft pairs $\times 10^{-4}$	cross section (ideal theoretical) nb
93 −2	89.4505	372.2	18.5 ± 1.5	1.8	-4.4 ± 1.4	81.965 ± 0.090
93 pk	91.2063	−23.3	3.6 ± 1.5	1.8	-4.4 ± 1.4	78.722 ± 0.087
93 +2	93.0351	−411.7	-16.3 ± 1.5	1.8	-4.4 ± 1.4	75.507 ± 0.083
94 a	91.2358	−29.7	2.8 ± 1.5	1.8	-4.4 ± 1.4	78.665 ± 0.087
94 b	91.2165	−25.5	3.3 ± 1.5	1.8	-4.4 ± 1.4	78.702 ± 0.087
94 c	91.4287	−71.8	-2.3 ± 1.5	1.8	-4.4 ± 1.4	78.293 ± 0.086
94 c’	91.2195	−26.2	3.3 ± 1.5	1.8	-4.4 ± 1.4	78.697 ± 0.087
95 −2	89.4415	374.3	18.5 ± 1.5	1.8	-4.4 ± 1.4	81.981 ± 0.090
95 pk	91.2829	−40.0	1.5 ± 1.5	1.8	-4.4 ± 1.4	78.573 ± 0.086
95 +2	92.9715	−398.5	-16.5 ± 1.5	1.8	-4.4 ± 1.4	75.609 ± 0.083

Table 21: Summary of corrections to the theoretical reference cross section of 78.898 ± 0.005 nb calculated at $E_{\mathrm{cm}} = 91.100$. The cross section listed in the last column does not include any detector related effects and the error is the theoretical error only. The actual luminometer acceptance is obtained by applying the acceptance corrections of table 23 to the ideal theoretical cross sections given in the last column.

9.3 Experimental acceptance corrections

As mentioned at the begining of this section, we divide the experimental acceptance corrections into two categories: those evaluated using the parameterized detector simulation (ϵ_{sim}), and those excluded from the detector simulation, and applied externally (ϵ_{ext}).

To evaluate ϵ_{sim} a set of four–vectors from the BHLUMI [?] event generator has been used to convolute the effects of the LEP beam parameters and of the detector response, determined directly from the data, with the underlying distributions of Bhabha events. This procedure relates the ideal detector acceptance, data set by data set, to the ideal theoretical acceptance with only small binomial uncertainties. The resulting correction factor (ϵ_{sim}) for a typical data sample is given in table 22, as well as its breakdown into individual effects as estimated with the Monte Carlo.

The largest correction, $\sim (-4.1 \pm 1.8) \times 10^{-4}$, is due to the energy response of the detector (section 4.3). The parameterization of the detector energy response has been studied in detail in the data, making extensive use of our ability to geometrically define the kinematics of Bhabha events. The systematic uncertainty quoted on the acceptance correction is based on varying the parameters describing the energy response over a range which safely covers that allowed by our studies. The corrections due to beam parameters are discussed in section 7, those due to coordinate resolutions and clustering in section 8. The corrections for resolution flow in the radial and azimuthal coordinates agree with the analytic expressions discussed in sections 4.1 and 4.2. The effect of finite energy resolution on the acceptance is nearly cancelled by an increase in acceptance from the beam offsets (section 7), resulting in a very small net difference between the ideal theoretical and ideal experimental acceptances. The $\Delta R - \Delta\Theta$ cut difference correction in table 22 results from a small technical discrepancy between the acollinearity cut defined in terms of a fixed difference in Θ ($\Delta\Theta = 10.162$mrad) used for the theoretical reference acceptance, and the acollinearity cut defined in terms of a fixed difference in R ($\Delta R = 2.5$ cm) used for the experimental acceptance.

The relatively large variations in LEP beam parameters, as well as changes in the energy resolution due to the configuration of upstream material, require that the acceptance be calculated separately for each of the data samples, resulting in variations of about 2×10^{-4}. The total simulation correction (ϵ_{sim}) for each data sample is given in table 23.

The external corrections (ϵ_{ext}) account for differences between the *actual* detector and the *ideal* detector described by the parametrized simulation. These corrections were discussed in sections 2.3

Effect	Typical acceptance correction $(\times 10^{-4})$		
Energy resolution	-4.1	± 1.8	± 0.33
Beam parameters	$+2.7$	± 0.8	± 0.56
Radial resolution	-0.4	± 0.2	± 0.33
Acollinearity bias	$+0.0$	± 0.36	± 0.33
Azimuthal resolution	-0.2	± 0.04	± 0.13
Clustering	-0.3	± 1.0	± 0.08
$\Delta R - \Delta\Theta$ cut difference	-0.7	± 0.0	± 0.03
Total	-3.0	± 2.3	± 0.81

Table 22: Values of the acceptance corrections for data sample 94b due to effects which are evaluated using the Monte Carlo (ϵ_{sim}). The first error is systematic (see table 24), the second is the statistical error of the Monte Carlo.

Effect	93 −2	93 pk	93 +2	94a	94b	94c	95 −2	95	95 +2
Radial Metrology (sec 2.3)	1.55	1.55	1.55	1.55	1.55	1.55	1.55	1.55	1.55
Radial Thermal (sec 2.3.2)	−0.86	−0.85	−0.85	−1.13	−1.22	−1.31	−2.72	−2.69	−2.72
Inner Anchor (sec 4.1.4)	2.18	2.18	2.18	2.18	2.18	2.18	4.64	4.64	4.64
Outer Anchor (sec 4.1.4)	−1.78	−1.78	−1.78	−1.78	−1.78	−1.78	−1.19	−1.19	−1.19
Z Metrology (sec 2.4)	0.50	0.59	0.50	1.16	0.72	0.08	−0.95	−0.95	−0.95
Background (sec 5)	0.65	0.50	0.30	0.16	0.09	0.22	0.15	0.10	0.10
Trigger (sec 6)	0.00	0.00	0.00	0.00	0.00	0.00	0.00	0.00	0.00
Wagon Tagger (sec 6)	0.00	0.00	0.00	0.00	0.00	0.00	−0.10	−0.10	−0.10
Total External (ϵ_{ext})	2.24	2.19	1.90	2.13	1.54	0.94	1.38	1.36	1.33
Total Simulation (ϵ_{sim})	−2.13	−1.81	−1.96	0.36	−2.98	0.26	−2.33	−2.33	−2.18
Grand Total	0.11	0.38	−0.06	2.50	−1.44	1.20	−0.95	−0.97	−0.85

Table 23: This table summarizes the detector acceptance corrections for the L_{RL} luminosity measurement for the nine data samples. All corrections are in units of 10^{-4}. The sum of ϵ_{ext} and ϵ_{sim}, the grand total, has been applied to the ideal theoretical cross sections given in section 9.1, table 21 to obtain the actual luminometer acceptance for each data sample.

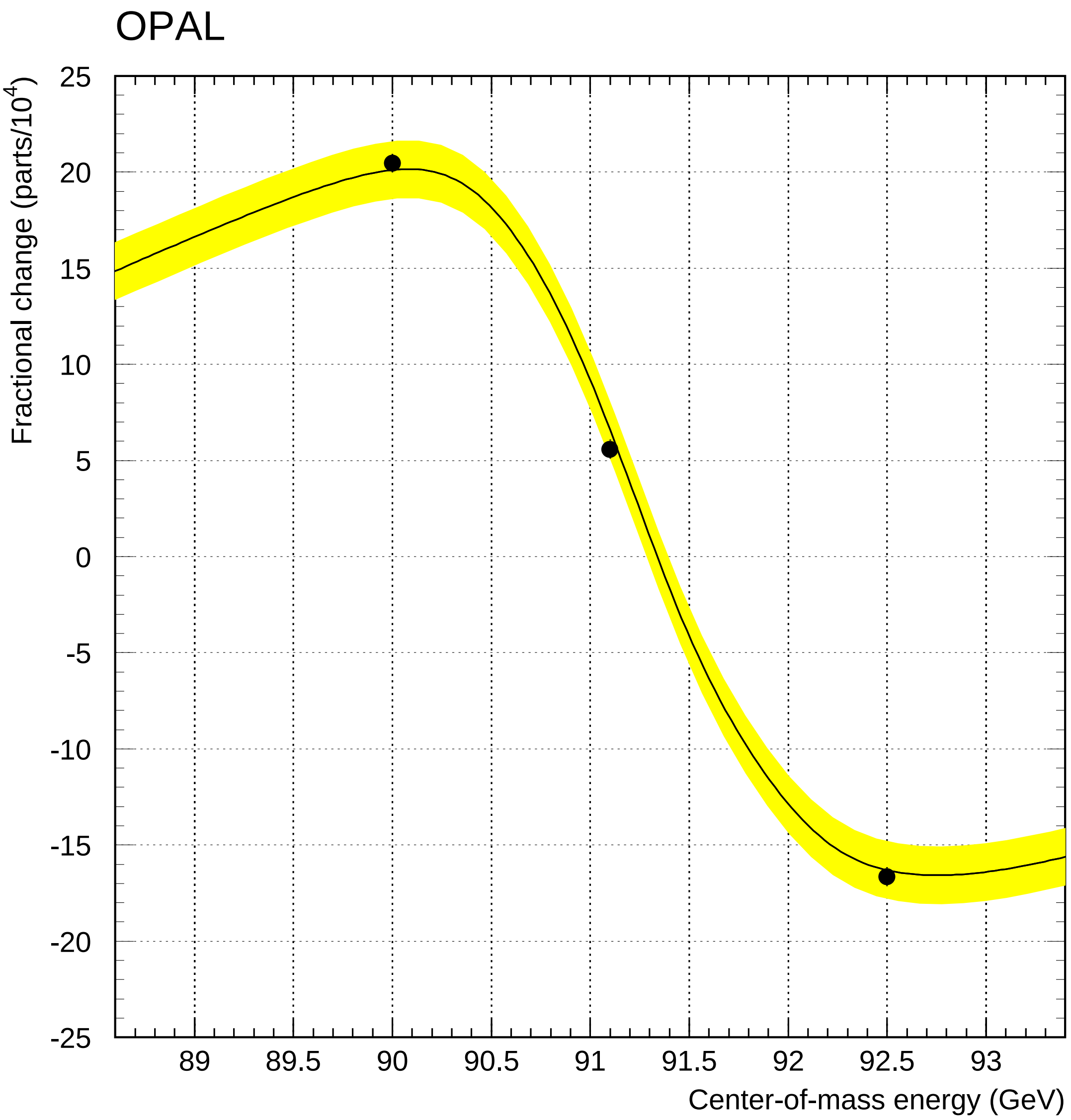

Figure 30: Relative size of the energy dependence of the SiW acceptance as a function of center-of-mass energy near the Z^0 peak, excluding the fundamental $1/s$ dependence of the cross section. The curve includes the effects of $Z-\gamma$ interference and the variation (6×10^{-4}) in vacuum polarization. The band gives the error assigned to this correction. The points with (statistical) error bars display the result of direct calculations at three energy points using BHLUMI 4.04.

and 2.4 (metrology), 4.1.4 (radial anchoring), 5 (background), and 6 (trigger). Accurate metrology of the detector dimensions, and direct measurements of bias in the radial coordinate from test beam data, enable us to control the uncertainty in the radial acceptance-defining cuts at better than the 2×10^{-4} level. Careful monitoring of backgrounds and a well-designed trigger keep corrections and systematic errors from these sources small. In table 23 we list the values of these external corrections ($\epsilon_{\rm ext}$) for each of the nine data samples.

In table 24 we give the systematic uncertainties on each of the $\epsilon_{\rm ext}$ and $\epsilon_{\rm sim}$ correction factors. The grand total quadrature sum of these uncertainties gives the total experimental uncertainty in the absolute luminosity measurement using the average of the SwitR and SwitL selections. Taking into account all sources of experimental error, the quadrature sum of the correlated and uncorrelated systematic errors is 3.3×10^{-4}, degrading slightly to 3.5×10^{-4} in 1995. Due to the statistical manner in which the greater part of these systematic errors have been evaluated, as well as the fact that four independent sources of error make contributions greater than 1×10^{-4}, we would like to point out that these one-sigma errors can be extrapolated to greater levels of significance in a Gaussian fashion. The final experimental luminosity error correlation matrix is given in table 25. The classification of the detailed sources of error into correlated and uncorrelated components given in table 24 does not reveal the complete pattern of correlations embodied in the full correlation matrix. In the table, the detailed errors classified as correlated are fully correlated between all data samples, while those classified as uncorrelated are often correlated within a given year, but uncorrelated between years.

10 Properties of the Bhabha event sample

In the preceeding sections, we have demonstrated that the characteristics of our detector, as well as the background in our event sample, are well understood. In this section we compare distributions of the quantities on which the Bhabha selection is based with the predictions of the BHLUMI Monte Carlo [**?**]. The agreement in every aspect is excellent, even though the tuning of the detector response functions was carried out in a manner almost completely independent of the BHLUMI Monte Carlo. We must also emphasize that we derive no part of our systematic error from these comparisons. All such errors are determined directly from the data and the limitations on our ability to understand the detector response. The data–Monte Carlo comparisons therefore represent, in great measure, a blind test in which discrepancies can only be interpreted as a failure of either our experimental or theoretical understanding. In either case, such a discrepancy would necessarily invalidate the luminosity measurement.

Furthermore, since the higher-order terms which represent the limiting theoretical uncertainties in the Bhabha scattering calculation are expected to leave little trace in the experimentally observable quantities, even perfect agreement between the measured and expected distributions can not be used to argue for a reduction in the theoretical error. The material of this section therefore represents a demanding test of the luminosity measurement, in which it is impossible for the agreement to be better than expected. The agreement is, and must be, essentially perfect.

The most important isolation cut concerns the energy. In figure 31 we compare the rate of “single radiative” events, predominately from initial–state radiation, to the prediction from the Monte Carlo. One of the electrons is required to satisfy $E > 0.85 \cdot E_{\mathrm{beam}}$ and the energy of the other is plotted. The energy response of the detector was determined using a sample of very collinear events and the kinematics of radiative events. This determination was independent of the rate of radiative events, allowing this rate to be used as a test of the Monte Carlo. There is good agreement between the predicted and observed radiative tail. This tail can best be observed when the acollinearity cut is suppressed, indicating that BHLUMI gives a valid description of the radiative energy tail over almost five orders of magnitude.

The acollinearity distribution (difference between R_{R} and R_{L}) is shown in figure 32. This plot also shows agreement between the Monte Carlo and the data over almost five orders of magnitude. The two peak structure of the plot is due to the beam offset. The good agreement near the peak is due to the use of the measured LEP beam parameters in the simulation. The agreement in the tail provides more evidence that initial–state radiation is correctly implemented in the Monte Carlo.

Further features of radiative processes in small–angle Bhabha scattering are revealed by studying accepted Bhabha events with secondary clusters falling within the SiW acceptance. The excellent capability of our detector for resolving even close–lying clusters allows a sensitive comparison to be made between the observed and expected rates of such secondary clusters. Despite the fact that the luminosity acceptance depends only weakly on the fidelity with which secondary clusters are treated experimentally, faith in the accuracy of higher-order terms in the calculation of the Bhabha scattering cross section would be undermined if the observed distribution of secondary clusters did not conform to theoretical expectations.

Figure 33 shows the observed energy spectrum of comfortably resolved secondary clusters which

Uncertainty	section	93 -2	93 pk	93 +2	94a	94b	94c	95 -2	95	95 +2
Radial Metrology	2.3									
uncorrelated		0.00	0.00	0.00	0.00	0.00	0.00	0.00	0.00	0.00
correlated		1.40	1.40	1.40	1.40	1.40	1.40	1.40	1.40	1.40
Radial Thermal	2.3.2									
uncorrelated		0.06	0.00	0.06	0.09	0.11	0.11	0.25	0.25	0.25
correlated		0.18	0.18	0.18	0.18	0.18	0.18	0.18	0.18	0.18
Inner Anchor	4.1.4									
uncorrelated		0.23	0.23	0.23	0.23	0.23	0.23	0.58	0.58	0.58
correlated		1.36	1.36	1.36	1.36	1.36	1.36	1.36	1.36	1.36
Outer Anchor	4.1.4									
uncorrelated		0.13	0.13	0.13	0.13	0.13	0.13	0.28	0.28	0.28
correlated		0.31	0.31	0.31	0.31	0.31	0.31	0.30	0.30	0.30
Z Metrology	2.4									
uncorrelated		0.00	0.00	0.00	0.00	0.00	0.00	0.37	0.37	0.37
correlated		0.41	0.41	0.41	0.41	0.41	0.41	0.41	0.41	0.41
Background	5									
uncorrelated		0.76	0.76	0.76	0.75	0.75	0.75	0.76	0.76	0.76
correlated		0.75	0.75	0.75	0.75	0.75	0.75	0.75	0.75	0.75
Trigger	6									
uncorrelated		0.00	0.00	0.00	0.00	0.00	0.00	0.00	0.00	0.00
correlated		0.04	0.04	0.04	0.04	0.04	0.04	0.04	0.04	0.04
Wagon Tagger	6									
uncorrelated		0.00	0.00	0.00	0.00	0.00	0.00	0.02	0.02	0.02
correlated		0.00	0.00	0.00	0.00	0.00	0.00	0.00	0.00	0.00
Total External ($\Delta\epsilon_{\mathrm{ext}}$)										
uncorrelated		0.81	0.81	0.81	0.80	0.80	0.81	1.10	1.10	1.10
correlated		2.16	2.16	2.16	2.16	2.16	2.16	2.16	2.16	2.16
Energy	4.3									
uncorrelated		0.10	0.10	0.10	0.10	0.10	0.10	0.10	0.10	0.10
correlated		1.80	1.80	1.80	1.80	1.80	1.80	1.80	1.80	1.80
Beam parameters	7									
uncorrelated		0.57	0.57	0.57	0.57	0.57	0.57	0.57	0.57	0.57
correlated		0.57	0.57	0.57	0.57	0.57	0.57	0.76	0.76	0.76
Radial resolution	8									
uncorrelated		0.00	0.00	0.00	0.00	0.00	0.00	0.00	0.00	0.00
correlated		0.20	0.20	0.20	0.20	0.20	0.20	0.20	0.20	0.20
Acollinearity bias	8									
uncorrelated		0.00	0.00	0.00	0.00	0.00	0.00	0.00	0.00	0.00
correlated		0.36	0.36	0.36	0.36	0.36	0.36	0.36	0.36	0.36
Azimuthal resolution	8									
uncorrelated		0.00	0.00	0.00	0.00	0.00	0.00	0.00	0.00	0.00
correlated		0.04	0.04	0.04	0.04	0.04	0.04	0.04	0.04	0.04
Clustering	8									
uncorrelated		0.00	0.00	0.00	0.00	0.00	0.00	0.00	0.00	0.00
correlated		1.00	1.00	1.00	1.00	1.00	1.00	1.00	1.00	1.00
$\Delta R - \Delta\Theta$ cut difference	9.3									
uncorrelated		0.00	0.00	0.00	0.00	0.00	0.00	0.00	0.00	0.00
correlated		0.00	0.00	0.00	0.00	0.00	0.00	0.00	0.00	0.00
M.C. statistics	8									
uncorrelated		0.29	0.27	0.29	0.33	0.13	0.25	0.36	0.34	0.32
correlated		0.80	0.80	0.80	0.80	0.80	0.80	0.80	0.80	0.80
Total Simulation ($\Delta\epsilon_{\mathrm{sim}}$)										
uncorrelated		0.65	0.64	0.65	0.67	0.59	0.63	0.68	0.67	0.66
correlated		2.32	2.32	2.32	2.32	2.32	2.32	2.37	2.37	2.37
Grand Total										
uncorrelated		1.04	1.03	1.04	1.04	1.00	1.03	1.29	1.28	1.28
correlated		3.17	3.17	3.17	3.17	3.17	3.17	3.21	3.21	3.21

Table 24: This table summarizes the experimental systematic uncertainties on the absolute L_{RL} luminosity measurement for the nine data samples. The lines labeled correlated and uncorrelated refer to errors correlated and uncorrelated among the samples. All errors are in units of 10^{-4}.

Sample	93 −2	93 pk	93 +2	94 a	94 b	94 c	95 −2	95	95 +2
93 −2	1.00	0.91	0.91	0.90	0.90	0.90	0.87	0.87	0.87
93 pk	0.91	1.00	0.91	0.90	0.90	0.90	0.87	0.87	0.87
93 +2	0.91	0.91	1.00	0.90	0.90	0.90	0.87	0.87	0.87
94a	0.90	0.90	0.90	1.00	0.90	0.90	0.87	0.87	0.87
94b	0.90	0.90	0.90	0.90	1.00	0.90	0.87	0.87	0.87
94c	0.90	0.90	0.90	0.90	0.90	1.00	0.87	0.87	0.87
95 −2	0.87	0.87	0.87	0.87	0.87	0.87	1.00	0.91	0.91
95 pk	0.87	0.87	0.87	0.87	0.87	0.87	0.91	1.00	0.91
95 +2	0.87	0.87	0.87	0.87	0.87	0.87	0.91	0.91	1.00

Table 25: The experimental luminosity correlation matrix.

are identified by the kinematic cluster selection algorithm as belonging to the Bhabha event. To ensure that the events entering this study are kinematically complete, we further require that one side of the event consists of a single full–energy cluster, and that the total measured energy in the event is within 10% of the LEP center-of-mass energy. The energy spectrum of such clusters predicted by BHLUMI, also shown in figure 33, agrees well with the experimental measurements, except for the two lowest energy bins.

The acoplanarity distribution is displayed in figure 34. Good agreement between the Monte Carlo expectation and the data is seen throughout most of the distribution. At small values of acoplanarity some differences between Monte Carlo and data are observed. These differences are due to the rather crude treatment of the ϕ resolution in the detector simulation, which does not reproduce the non–Gaussian features of the true detector response, and are not an indication of a problem in the physics Monte Carlo. A 10% error in the calculated resolution flow in acoplanarity is assigned to account for these imperfections (see section 4.2).

The distribution of the right radial coordinates for the SwitL sample, and similarly the left radial coordinate for the SwitR sample, are shown in figure 35. These distributions are closely related to the acollinearity distribution, as the tight radial cut on the opposite side provides an effective acollinearity cut on the events near the inner and outer edges of the acceptance.

The radial distributions after all cuts, except the tight radial definition cut, are displayed in figure 36 and the locations of the definition cuts are indicated. Good agreement between the data and Monte Carlo is seen except for a small amount of structure near the center of the acceptance on the right and left sides, behind the bulk of the upstream material (see figure 3). The radial distribution checks the prediction of the Monte Carlo on the scale of the radial granularity of the detector (0.25 cm). The smoothing procedure, described in section 4.1.3, suppresses any structure within each pad at the 7 X_0 reference plane and therefore the radial distributions do not check the prediction of the Monte Carlo on scales smaller than a pad.

Some global checks of the selection procedure have already been mentioned in sections 4.1.4 and 7. Shifting the location of the inner radial cut one pad boundary lower or higher leads to changes in measured luminosity of $0.4 \pm 1.3 \times 10^{-4}$ and $-0.9 \pm 1.3 \times 10^{-4}$ respectively. A stronger check on the selection comes from the comparison of the luminosity measurement based on SwitA with that based on SwitR and SwitL. The SwitA selection has additional systematic errors beyond those of the SwitR and SwitL selections due to differences in the resolution of the individual right and left coordinates and the averaged coordinate. These systematic effects are estimated to be at the level of 1.5×10^{-4}. On the other hand the dependence of the SwitA selection on the beam parameters is substantially different than that of the SwitR and SwitL selection. Comparing the two selections we find that the selection for SwitA and $\frac{1}{2}(\text{SwitR} + \text{SwitL})$ differ by $65.4 \pm 0.9 \times 10^{-4}$ in the data and $65.3 \pm 1.0 \times 10^{-4}$ in the Monte Carlo. The residual difference between data and Monte Carlo is much smaller than the additional systematic error of the SwitA selection.

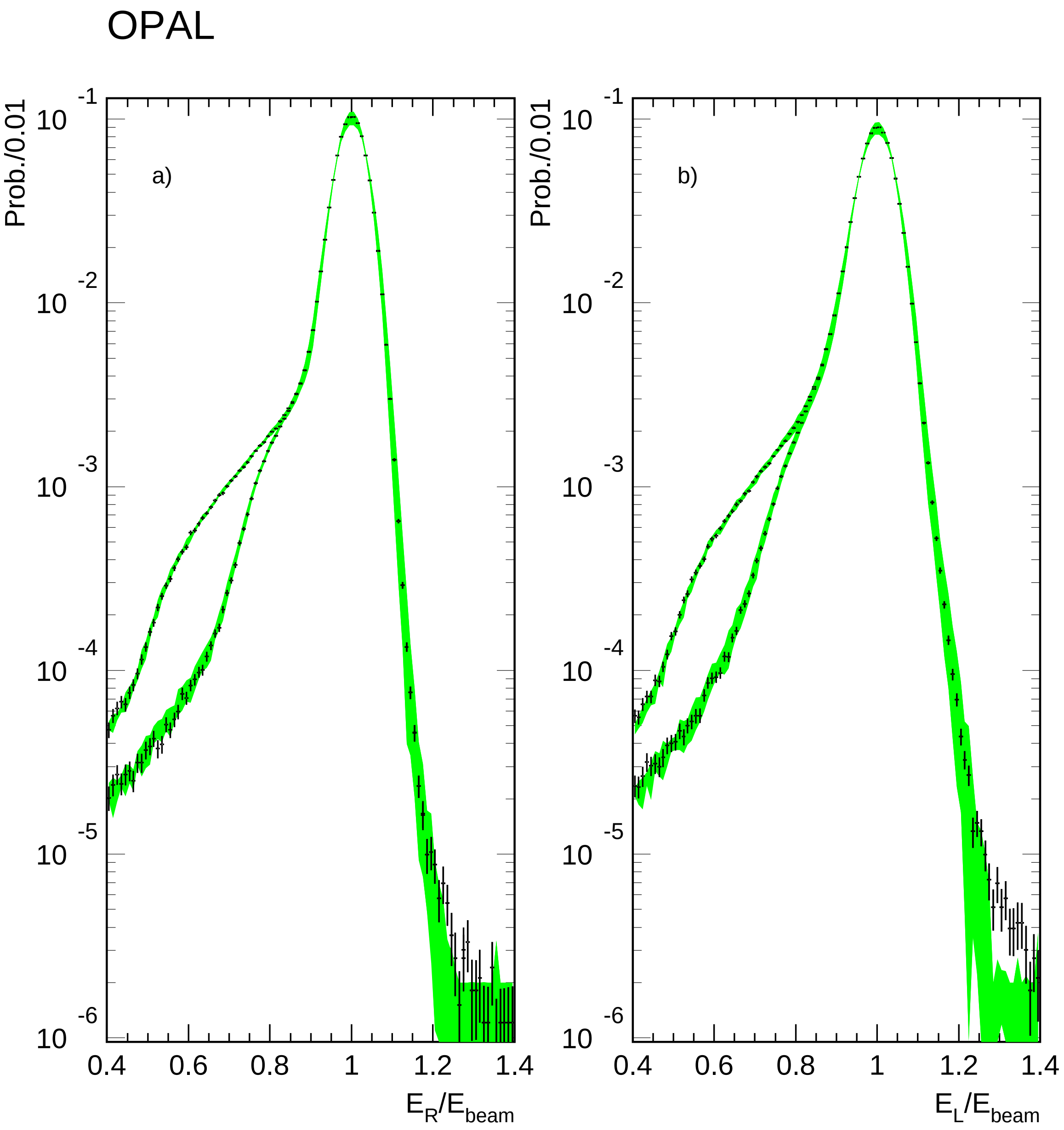

Figure 31: The normalized energy distributions in the right (a) and left (b) calorimeter for events passing all geometric cuts for the SWITA selection and which in addition have more than 0.85 of the beam energy in the opposite calorimeter. The energy spectrum is shown respectively before and after the acollinearity cut has been applied in the upper and lower branches of the curves. The points with errors show the data. The shaded bands show the Monte–Carlo predictions for the range of energy parameterizations used in assessing the systematic error (see section 4.3). Above 0.8 the upper and lower branches of the curves are nearly indistinguishable.

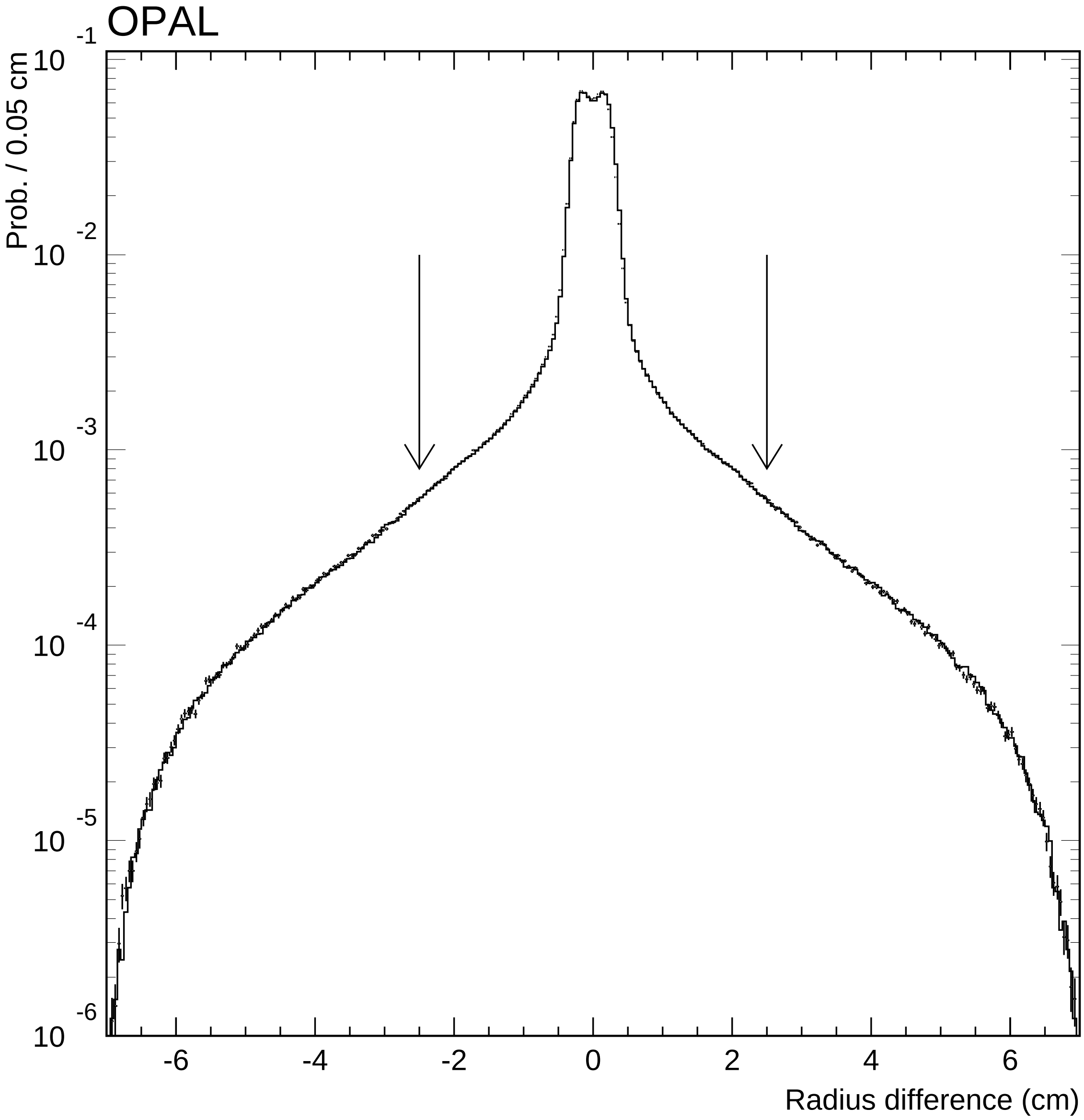

Figure 32: The distribution of $R_{\mathrm{R}} - R_{\mathrm{L}}$ after all the SWITA selection cuts have been applied, except for the acollinearity cut. Data are shown as the points and Monte Carlo as the solid histogram. For this comparison, the background from accidental coincidences of off-momentum beam particles has been subtracted from the data. The acollinearity cut is indicated by the two vertical arrows.

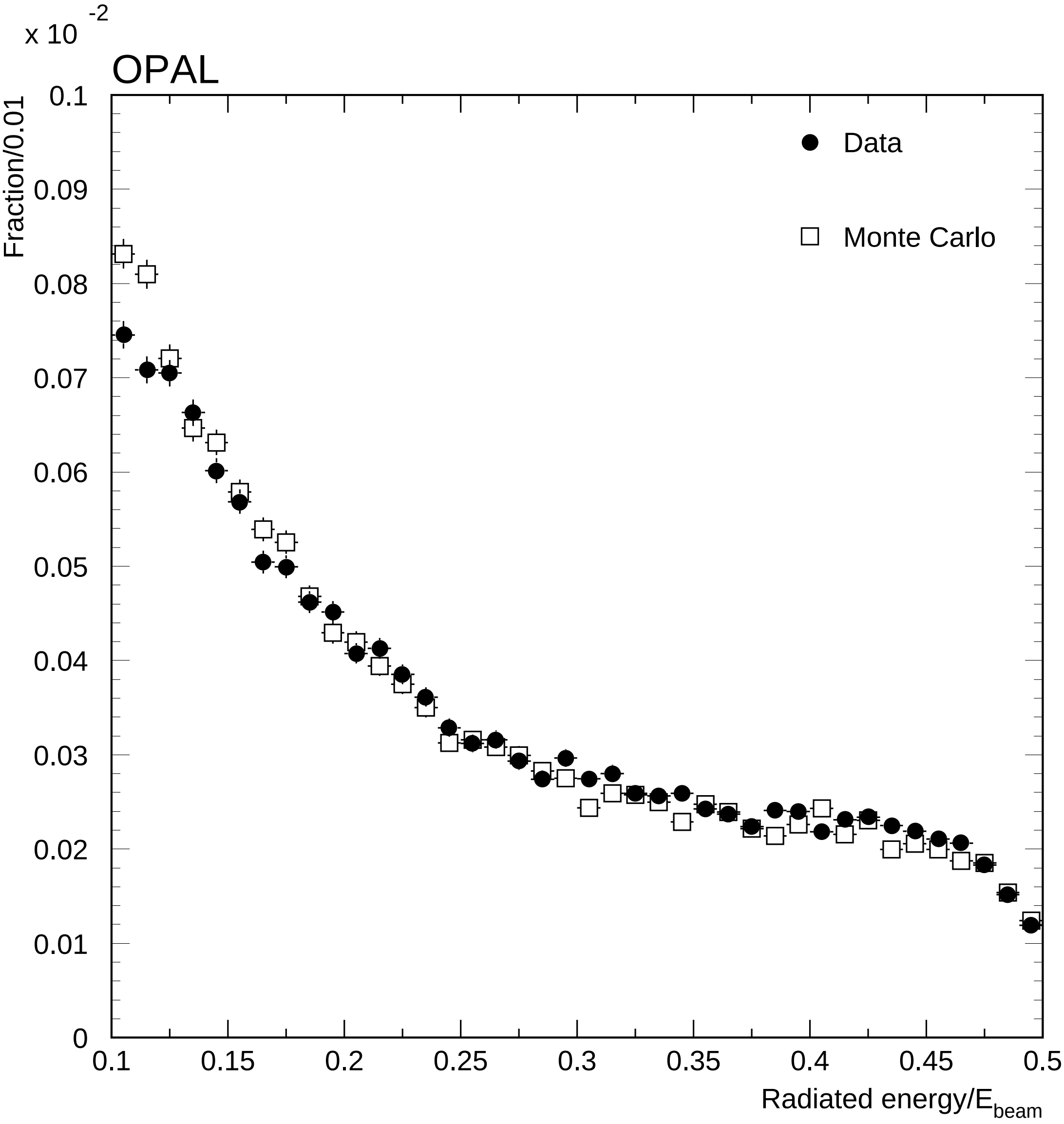

Figure 33: The energy distribution of the least energetic cluster in SwitA events where the kinematic cluster selection algorithm has selected exactly one cluster on one side of the detector, and two on the other. To ensure a sample of kinematically complete events, we furthermore require that the total measured energy in the event is within 10% of the LEP center-of-mass energy. Only those clusters separated by at least 2 cm in radius or 400 mrad in azimuth are shown. Data and Monte Carlo are independently normalized to the total number of Bhabha events with a single full–energy cluster on one side of the detector.

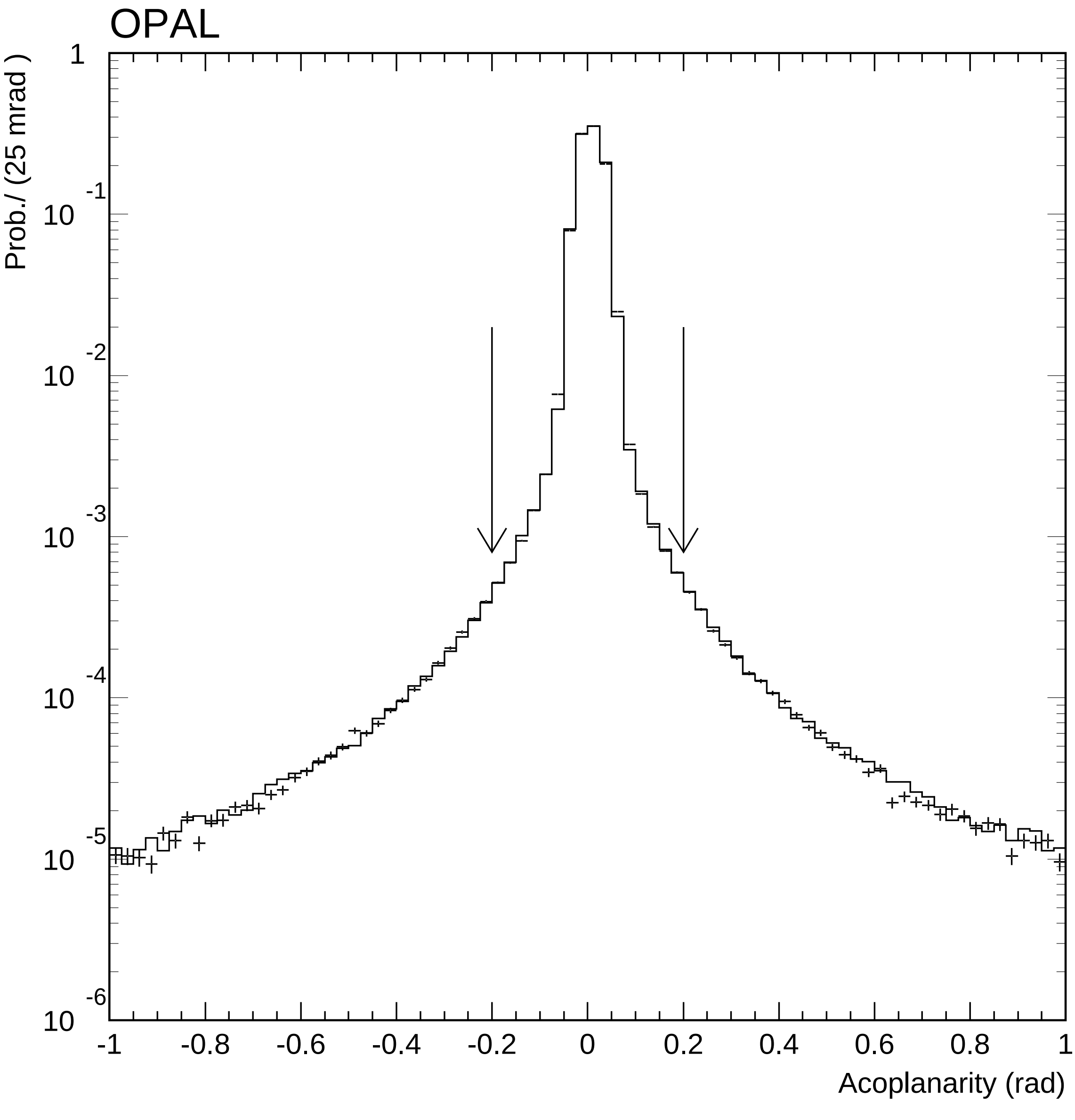

Figure 34: The distribution of the acoplanarity $((\phi_R - \phi_{L)-\pi)})$ after all the SwitA selection cuts have been applied, except for the acoplanarity cut. Data are shown as points and Monte Carlo as the solid histogram. For this comparison, the background from accidental coincidences of off-momentum beam particles has been subtracted from the data. The acoplanarity cut is indicated by the two vertical arrows. The mean acoplanarity is offset from zero by 6.2 mrad averaged over all fills. This can be compared with the expected effect due to the OPAL magnetic field, which is 6.34 mrad.

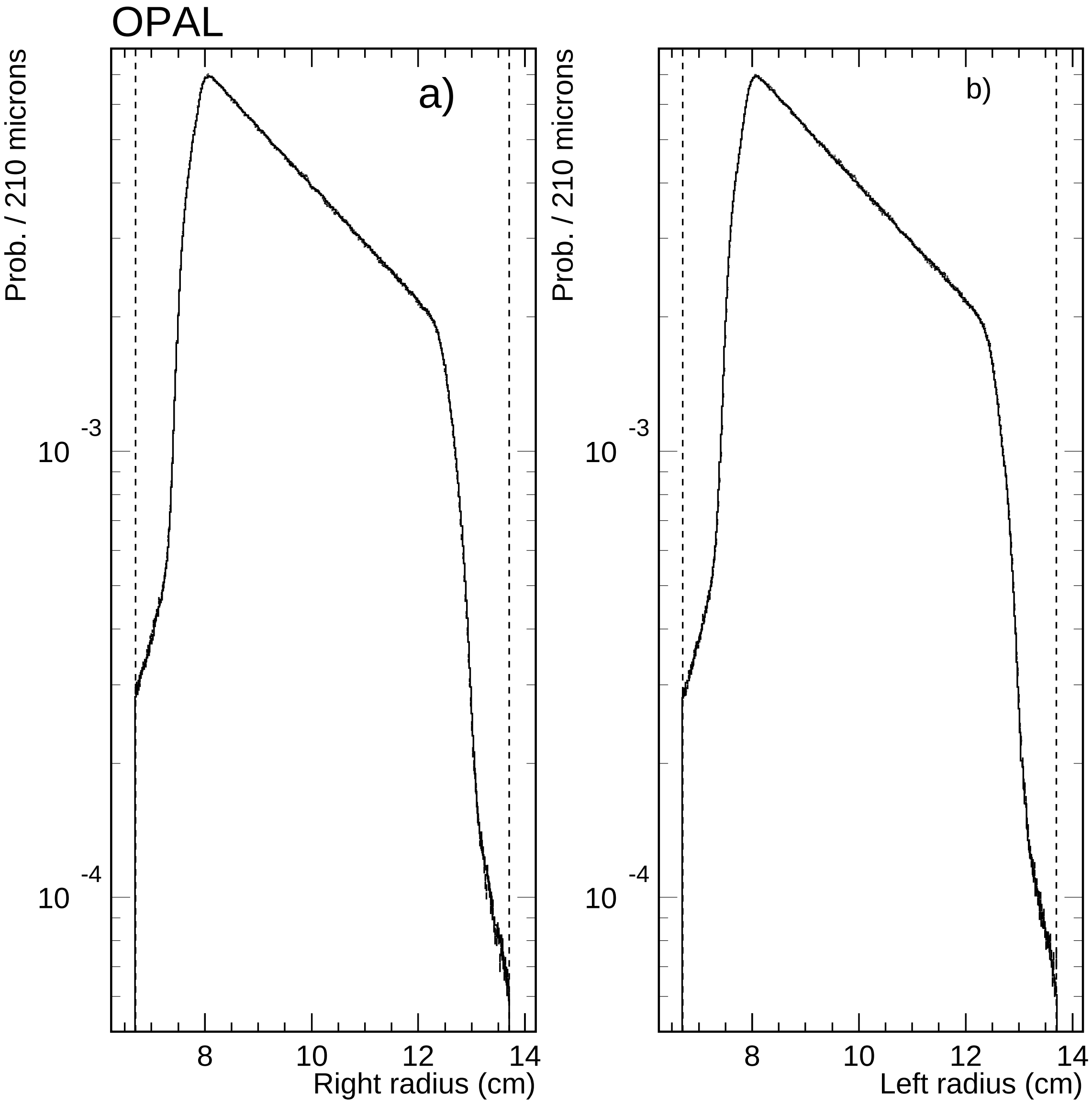

Figure 35: The distributions of R_{R} after all SwitL selection cuts have been applied (a), and of R_{L} after all SwitR selection cuts have been applied, (b). The points and error bars are the data and the histogram the Monte Carlo. The vertical dotted lines indicate the radial isolation cuts.

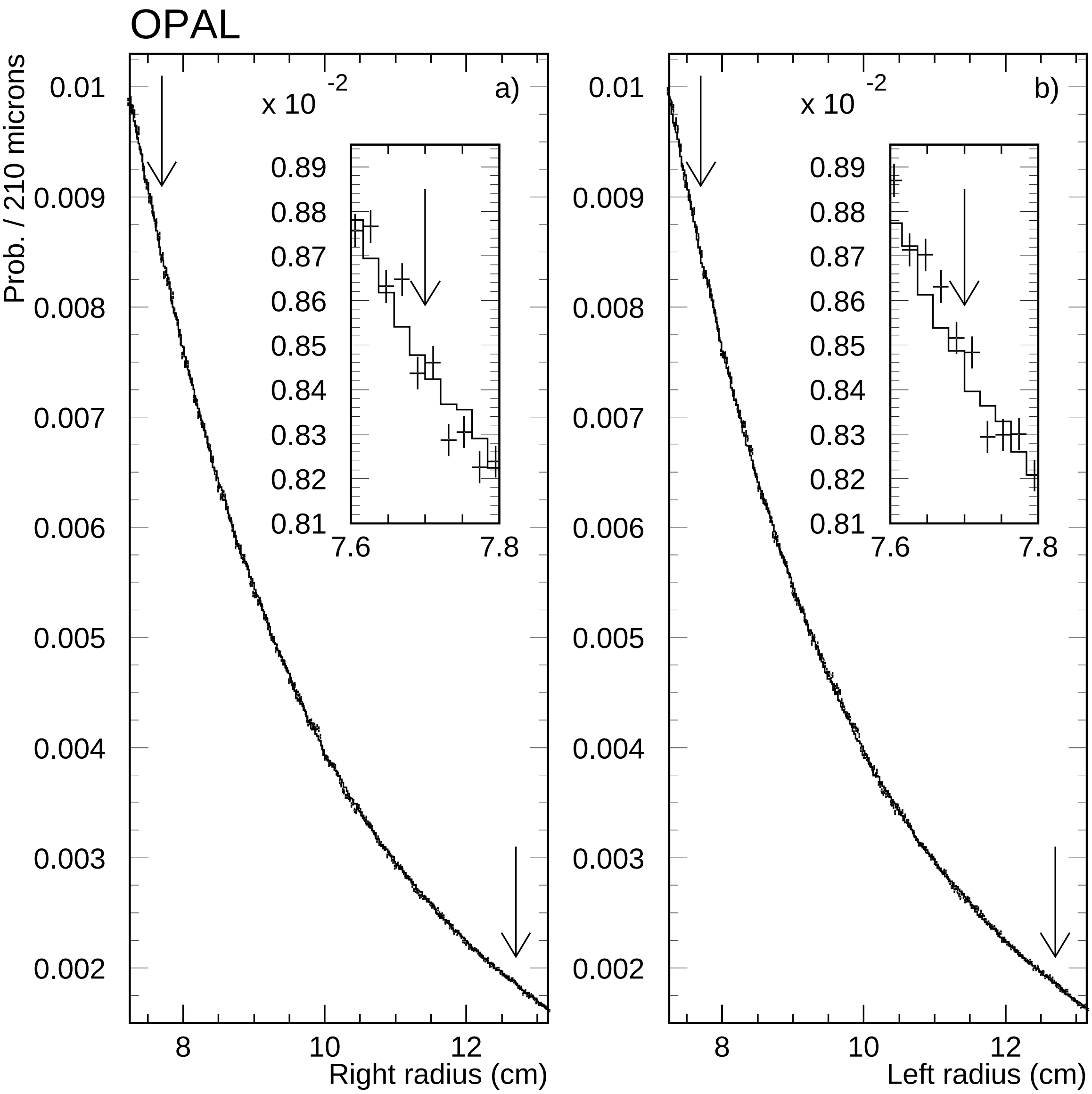

Figure 36: The distributions (after the isolation cuts have been applied) of R_{R} (a), and R_{L} (b). The arrows indicate the location of the definition cuts for the SwitR and SwitL selections. The points and error bars are the data and the histogram the Monte Carlo. The insets show fine details near the inner acceptance boundaries.

11 Conclusion

The OPAL Silicon-Tungsten Luminometer has been used to measure the integrated luminosity at the OPAL intersection region at LEP since its installation in 1993. After stringent requirements on the condition of the detector during data taking, it provides valid measurements for 101 pb^{-1} of OPAL data, which represents $\sim 60\%$ of the entire OPAL LEP I data sample. The detector has achieved a fractional experimental systematic error of 3.4×10^{-4} in defining the acceptance within which the number of small-angle Bhabha scattering events have been counted to determine the luminosity. This precision represents more than an order of magnitude improvement with respect to previous OPAL results using the Forward Detector [**?**].

As a result, the experimental precision of the luminosity measurement no longer represents a significant limitation in the OPAL determination of the absolute coupling strengths of the Z^0. The statistical error inherent in the entire sample of 8×10^6 small angle Bhabha events observed in the ~ 79 nb fiducial acceptance of the luminometer is similar in size to the experimental systematic error in the luminosity, and also contributes negligibly to the total error.

All observable properties of the luminosity event sample agree well with the current theoretical understanding of small–angle Bhabha scattering. The dominant contribution to the uncertainty in the OPAL luminosity is the current theoretical error of 5.4×10^{-4} in the calculated acceptance.

The uncertainty in the OPAL acceptance for hadronic Z^0-decays is 7×10^{-4} [**?**, **?**], comparable to the statistical error in the total sample of 2.4×10^6 hadronic Z^0 decays. The OPAL measurement of $\Gamma_{\mathrm{inv}}/\Gamma_{\ell^+\ell^-}$, a quantity which depends crucially on the determination of absolute cross sections, has a total relative error of 4.4×10^{-3}, of which only 1.7×10^{-3} is attributable to the luminosity measurement. In the end, the SiW luminometer has made a dramatic improvement in our ultimate knowledge of the Z^0 couplings, quantities whose precise measurement has been the fundamental goal of the experimental program at LEP I.

The measured luminosity for the 1993-1995 multihadron sample is given in table 26.

Sample	Energy (GeV)	Multihadrons	SwitR	SwitL	Luminosity (pb^{-1})
93 −2	89.4505	84710	697370	699041	8.515 ± 0.010
93 pk	91.2063	262735	689570	690487	8.761 ± 0.011
93 +2	93.0351	123895	682445	683642	9.042 ± 0.011
94 a	91.2358	267413	698423	701928	8.895 ± 0.011
94 b	91.2165	1238184	3238878	3252718	41.229 ± 0.023
94 c	91.4287	11135	29066	29211	0.372 ± 0.002
94 c'	91.2195	68324	177864	178154	2.261 ± 0.005
95 −2	89.4415	83254	691317	690522	8.425 ± 0.010
95 pk	91.2829	139328	362725	362853	4.616 ± 0.008
95 +2	92.9715	126305	677469	675479	8.944 ± 0.011
Total		2405283	7945127	7964035	101.059 ± 0.036

Table 26: The mean center-of-mass energy, numbers of multihadron and luminosity events recorded in the 1993, 1994 and 1995 data samples as well as the corresponding luminosities, with their statistical error.

Acknowledgements:

We particularly wish to thank the SL Division for the efficient operation of the LEP accelerator at all energies and for their continuing close cooperation with our experimental group. We thank our colleagues from CEA, DAPNIA/SPP, CE-Saclay for their efforts over the years on the time-of-flight and trigger systems which we continue to use. We would also like to extend special thanks to the small community of theorists, without whose painstaking calculation of the radiative corrections to small–angle Bhabha scattering, the experimental precision of our result would have been in vain. In

addition to the support staff at our own institutions we are pleased to acknowledge the
Department of Energy, USA,
National Science Foundation, USA,
Particle Physics and Astronomy Research Council, UK,
Natural Sciences and Engineering Research Council, Canada,
Israel Science Foundation, administered by the Israel Academy of Science and Humanities,
Minerva Gesellschaft,
Benoziyo Center for High Energy Physics,
Japanese Ministry of Education, Science and Culture (the Monbusho) and a grant under the Monbusho International Science Research Program,
Japanese Society for the Promotion of Science (JSPS),
German Israeli Bi-national Science Foundation (GIF),
Bundesministerium für Bildung, Wissenschaft, Forschung und Technologie, Germany,
National Research Council of Canada,
Research Corporation, USA,
Hungarian Foundation for Scientific Research, OTKA T-016660, T023793 and OTKA F-023259.